



## Review article

# Unleashing the potential of tungsten disulfide: Current trends in biosensing and nanomedicine applications

Mohamed Bahri<sup>a,b,\*</sup>, Dongmei Yu<sup>c</sup>, Can Yang Zhang<sup>a,b</sup>, Zhenglin Chen<sup>a,b</sup>, Chengming Yang<sup>d</sup>, Lyes Douadji<sup>e</sup>, Peiwu Qin<sup>a,b,\*\*</sup>

<sup>a</sup> Center of Precision Medicine and Healthcare, Tsinghua-Berkeley Shenzhen Institute, Shenzhen, Guangdong Province, 518055, China

<sup>b</sup> Institute of Biopharmaceutical and Health Engineering, Tsinghua Shenzhen International Graduate School, Tsinghua University, Shenzhen 518055, China

<sup>c</sup> School of Mechanical, Electrical & Information Engineering, Shandong University, Weihai, Shandong 264209, China

<sup>d</sup> University of Science and Technology Hospital, Shenzhen, Guangdong Province, China

<sup>e</sup> Chongqing Institute of Green and Intelligent Technology Chinese Academy of Sciences, Chongqing City, China

## ARTICLE INFO

**Keywords:**

Tungsten disulfide  
Biomedical applications  
Nanomedicine  
Biosensing  
Oncotherapy  
Tissue engineering  
Drug delivery  
Anti-bacterial  
CVD growth

## ABSTRACT

The discovery of graphene ignites a great deal of interest in the research and advancement of two-dimensional (2D) layered materials. Within it, semiconducting transition metal dichalcogenides (TMDCs) are highly regarded due to their exceptional electrical and optoelectronic properties. Tungsten disulfide (WS<sub>2</sub>) is a TMDC with intriguing properties, such as biocompatibility, tunable bandgap, and outstanding photoelectric characteristics. These features make it a potential candidate for chemical sensing, biosensing, and tumor therapy. Despite the numerous reviews on the synthesis and application of TMDCs in the biomedical field, no comprehensive study still summarizes and unifies the research trends of WS<sub>2</sub> from synthesis to biomedical applications. Therefore, this review aims to present a complete and thorough analysis of the current research trends in WS<sub>2</sub> across several biomedical domains, including biosensing and nanomedicine, covering antibacterial applications, tissue engineering, drug delivery, and anticancer treatments. Finally, this review also discusses the potential opportunities and obstacles associated with WS<sub>2</sub> to deliver a new outlook for advancing its progress in biomedical research.

## 1. Introduction

The exploration of 2D materials gained momentum following the identification of graphene, composed of a carbon sheet only one atom thick [1,2]. Concurrently, the discovery and exploration of transition metal dichalcogenides (TMDCs) in the 1990s led to their increasing importance across various fields, including solar energy conversion, batteries, photodetectors, transistors, and surface coatings [3–6]. In recent years, TMDCs have also garnered attention in the biomedical field due to their high X-ray attenuation ability for radiotherapy and tomography, large exciton binding energy, strong photoluminescence, layer-dependent band gap, and good

\* Corresponding author. Center of Precision Medicine and Healthcare, Tsinghua-Berkeley Shenzhen Institute, Shenzhen, Guangdong Province, 518055, China.

\*\* Corresponding author. Center of Precision Medicine and Healthcare, Tsinghua-Berkeley Shenzhen Institute, Shenzhen, Guangdong Province, 518055, China.

E-mail addresses: [mohamedbahri@sz.tsinghua.edu.cn](mailto:mohamedbahri@sz.tsinghua.edu.cn) (M. Bahri), [pwqin@sz.tsinghua.edu.cn](mailto:pwqin@sz.tsinghua.edu.cn) (P. Qin).

<https://doi.org/10.1016/j.heliyon.2024.e24427>

Received 18 September 2023; Received in revised form 18 December 2023; Accepted 9 January 2024

Available online 11 January 2024

2405-8440/© 2024 The Authors. Published by Elsevier Ltd. This is an open access article under the CC BY-NC-ND license (<http://creativecommons.org/licenses/by-nc-nd/4.0/>).

stability in ambient [7–10]. Among semiconducting TMDCs materials, tungsten disulfide ( $WS_2$ ) is composed of stacked layers, where each layer is composed of three atomic planes arranged in a hexagonal pattern, with a W metal plane sandwiched between two S atom planes, resulting in an S–W–S structure [11].  $WS_2$  displays a unique 2D morphology with a tunable crystal structure and is highly versatile in constructing biological sensing, photothermal therapy, drug delivery, bioimaging, and antibacterial platforms with multiple functionalities [12,13]. It also boasts low cytotoxicity, satisfactory biodegradability, and high biocompatibility at a low cost.

For instance, tungsten disulfide shows great promise in biomedicine due to its ability to be modified for increased biocompatibility and tumor targeting by incorporating specific antibodies or biomolecule modification [14,15]. Specifically,  $WS_2$  has the potential to break down the elevated level of hydrogen peroxide present in solid tumors into oxygen. This not only helps alleviate the hypoxic conditions in the tumor but also produces reactive oxygen species (ROS) for tumor therapy within a particular wavelength spectrum [16]. Unlike graphene,  $WS_2$  exhibits lower toxicity and is rapidly excreted and biodegradable [17]. Tungsten disulfide possesses the ability to absorb near-infrared light, specifically within the range of 700–1100 nm, and displays exceptional optical stability and an impressive photothermal conversion efficiency that is on par with that of gold nanoparticles, making it an ideal candidate for imaging-guided anti-tumor photothermal therapy (PTT) [18]. Additionally, the significant specific surface area of  $WS_2$  provides numerous potential binding sites for the attomolar sensitivity of different biomolecules [19–21], while its conductivity and appropriate band gap are critical aspects for  $WS_2$ -based biosensing applications [22–24].

To date, tungsten disulfide has garnered significant attention for numerous researchers, as indicated by the substantial body of publications dedicated to tungsten disulfide-based biomedical applications (Fig. 1). Some potential reviews have been reported. For example, Lan et al. [13] overviewed the numerous synthesis techniques of tungsten disulfide and discussed its electronic and optoelectronic applications. In another work, the properties of TMDCs and their application in biosensing and tumor therapies were reviewed by Wang et al. [9]. Earlier, Gu et al. [25] presented a general bibliometric and data set distribution of tungsten-based nanomaterials and its research hotspots in biomedical fields. Another comprehensive summary of the recent development of 2D TMDCs and their applications was reviewed by Choi et al. [8]. In the aforementioned reviews, unifying the diverse properties of  $WS_2$  by covering the most trending biological sensing and nanomedicine applications within a specific nanoarchitecture with a specific emphasis on its CVD synthesis and its associated challenges toward high-quality growth has not yet been offered. Therefore, the current review presents a comprehensive overview of the recent developments of CVD-mediated synthesis of 2D  $WS_2$  nanoarchitecture, details the fundamental properties of  $WS_2$ , and highlights their potential application in various biosensing and nanomedicine fields, including oncotherapy, drug delivery, antibacterial activity, and tissue engineering as displayed with representative examples in Scheme 1. At the end of this review, the main challenges and outlook associated with the aforementioned applications are also presented with detailed descriptions and discussion.

## 2. Recent advances in the synthesis and preparation of $WS_2$

Significant efforts have been devoted to synthesizing tungsten disulfide with uniform atomic structures and controllable size using various top-down and bottom-up techniques, such as CVD, mechanical exfoliations, molecular beam epitaxy (MBE), and solvothermal synthesis. Thus, for a more in-depth discussion of  $WS_2$  growth methods, we encourage the readers to refer to these additional references [8,13,26–29].

$WS_2$  belongs to TMDCs, the same as  $MoS_2$ , which, due to their weak interlayer van der Waals interaction, the mechanical exfoliation of crystals from bulk to thin layers was extensively adopted using scotch tape [30,31]. Nonetheless, mechanically exfoliated materials lacked size and thickness uniformity across large areas, making the mechanical exfoliation technique inadequate for large-scale production [26,27]. As an alternative exfoliation approach of  $WS_2$ , liquid-based exfoliation, including solvents assistance exfoliation [32], lithium intercalation approaches [33,34], and electrochemical exfoliation [35,36] have been widely relied on due to their simplicity, low cost, and high quality [37]. Following these approaches, larger nanoflakes in solution were performed, yet with difficult

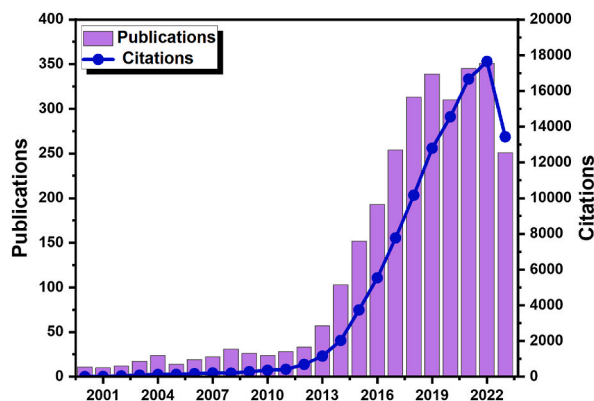
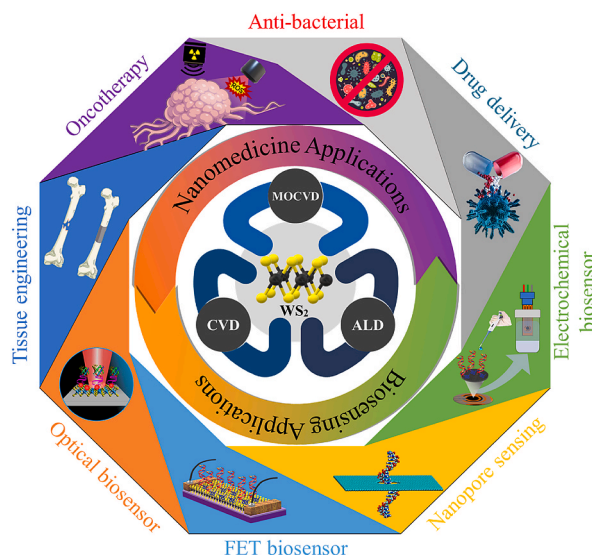


Fig. 1. The annual growth of publication and citation regarding tungsten disulfide ( $WS_2$ ) for biomedical applications. In total, 2939 publications were retrieved, including 2683 articles, 189 proceeding papers, 12 meeting abstracts, and other types of papers. Reproduced from the Web of Science core collection using the advanced search function in November 2023.



**Scheme 1.** The main research hotspots of tungsten disulfide ( $WS_2$ ) in the biosensing and nanomedicine applications.

thickness and lateral size controls [38]. Additionally, following the liquid exfoliation process frequently comes with chemical residue or introduces surface defects through sonication, causing material quality degradation [27].

On the other hand, the CVD process has been adopted for large-area growth of  $WS_2$ , though with lower quality and efficiency than those issued exfoliation methods [21]. Therefore, numerous efforts have been devoted to ameliorating  $WS_2$  quality using metal-organic-CVD (MOCVD), atomic layer deposition (ALD), and direct deposition methods, including pulsed laser deposition (PLD), sputtering, and e-beam. Such 2D material growth processes depend mainly on multiple factors such as the atomic gas flux, substrate lattice parameters, and temperatures [39,40]. Here, we provide a focused discussion on the  $WS_2$  growth by CVD, MOCVD, and ALD approaches, overviewing growth parameters dependent  $WS_2$  quality, and their pros and cons.

### 2.1. Chemical vapor deposition (CVD)

Chemical vapor deposition (CVD) is often considered one of the most straightforward techniques for large-area synthesizing atomically thin 2D TMDCs. The simplest form of CVD-based TMDCs growth involves the co-evaporation of chalcogen and metal oxide precursors, which further react in the vapor phase to form a stable layer on a suitable substrate (Fig. 2a). However, the precise growth mechanism differs considerably, depending on various factors such as the substrate properties, the temperature profile distribution, and the atomic gas flux (Fig. 2b).

The substrate properties significantly impact the atomic layer properties of the grown 2D TMDCs. Factors such as surface morphology, terminating atomic planes of the substrate, and its lattice mismatching can drastically influence the atomic layer of  $WS_2$  crystal [41]. Previous reports suggest that the substrate's surface energy plays a crucial role in the 2D TMDCs nucleation and growth [42,43]. In addition, the direct nucleation of  $WS_2$  layered film on a smooth surface presents an additional barrier due to the weak surface interaction with the in-plane passivated film. Therefore, two main growth mechanisms were generally followed. The first mechanism is based on the direct nucleation on imperfect sites [43], whereas the second is based on the formation of nanoparticles such as  $WO_3$ NPs and AuNPs [44,45].

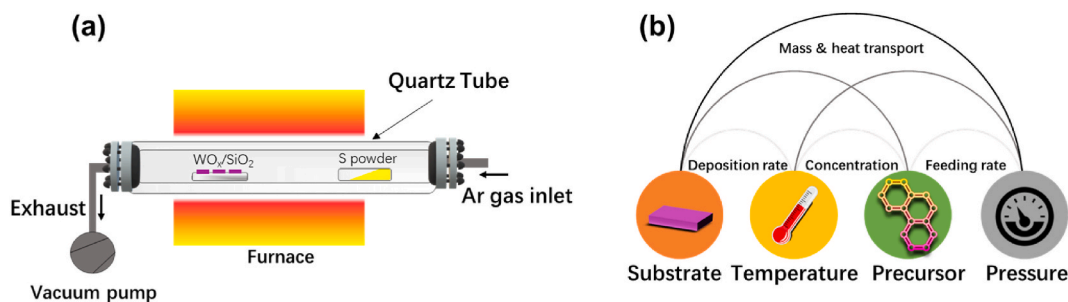


**Fig. 2.** Chemical Vapor deposition setup and parameters affecting growth. a) Schematic illustration of conventional CVD experimental setup for  $WS_2$  film growth under sulfur/argon environment. b) Schematic diagram displaying the growth parameters-dependent CVD kinetics.

Temperature is another crucial parameter of the growth reaction process. Generally, if the growth temperature is too high, surface diffusion occurs rapidly, enabling a randomly deposited adatom to move to the most favorable position, leading to the growth of 3D island. In contrast, at a low substrate temperature, adatoms lack sufficient kinetic energy to diffuse and locate the site with the lowest potential energy, forming an amorphous or polycrystalline film instead [46]. In addition, the growth reaction process is also limited to the atomic gas flux. Thus, sufficient high vapor pressure is necessary to provide an effective mix of the atomic gases inside the reactor chamber and ensure the atomic species carriage toward the growth substrate. Additionally, it is crucial to maintain a continuous feeding of vaporized atoms to prevent any undesirable reactions during the carriage into the reaction chamber [8]. The flow rate of the vaporized atoms using carrier gas is governed by Clausius–Clapeyron equation as written in the following equation (Eq. (1)):

$$\frac{d(\ln P)}{dT} = \frac{\Delta H}{KT} \quad (1)$$

where  $T$  is the temperature,  $P$  is the evaporated atoms' partial pressure,  $K$  is the Boltzmann constant, and  $\Delta H$  is the evaporation enthalpy [47].

Park et al. [48] used the  $H_2S$  and  $WCl_6$  as the S and W source for  $WS_2$  film growth at  $700^\circ C$ . The CVD growth of  $WS_2$  was carried out obeying the layer-by-layer mode, in which a controllable number of layers can be performed by varying the deposition time (Fig. 3a–f). In explicit, the growth of the second film begins once the first film is nearly complete. Following this gas precursor approach, a large

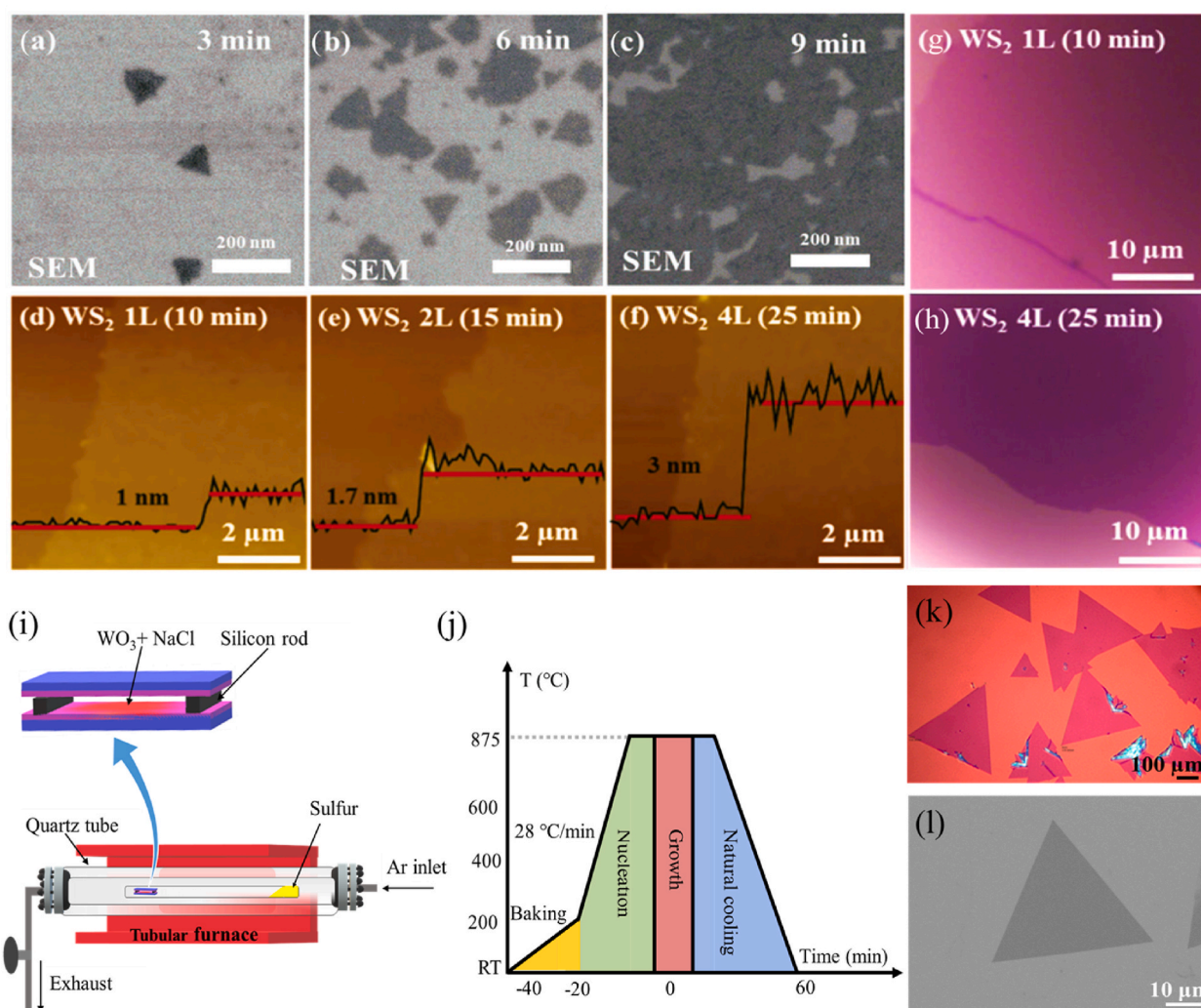


**Fig. 3.** CVD synthesis of  $WS_2$ . a–c) SEM images of the synthesized  $WS_2$  using growth period of 3, 6, and 9 min, d–f) AFM images of the CVD-grown  $WS_2$  film, depicting the growth time-dependent thickness of  $WS_2$ . Optical image of g) monolayer and h) quadlayer  $WS_2$  following the growth period of 10 min and 25 min, respectively. Reproduced with permission from Ref. [48]. Copyright 2015, Royal Society of Chemistry. i) Schematic illustration of NaCl-assisted  $WS_2$  growth setup. j) Temperature profile followed using NaCl-assisted CVD growth of  $WS_2$ . k) Optical image, and l) SEM image of the synthesized  $WS_2$  crystal. Reproduced with permission from Ref. [21]. Copyright 2022, American Chemical Society.

area synthesis was achieved (Fig. 3g and h); however, the grain size remains relatively small at only  $\approx 100$  nm. In addition, most of the CVD growth assay of WS<sub>2</sub> film often led to the growth of WS<sub>2</sub> flakes that are randomly distributed instead of a continuous film. The lack of continuous film synthesis was primarily due to the presence of an interfacial oxide layer, which posed a significant challenge [13]. Rong et al. [49] reported the synthesis of WS<sub>2</sub> domains with edges up to 370  $\mu\text{m}$  using chemical vapor reaction of tungsten trioxide (WO<sub>3</sub>) and sulfur powder at a growth temperature of 860 °C. Such a growth process led to the growth of monolayer triangular flakes instead of a continuous WS<sub>2</sub> film governed by two transformation steps. Firstly, sulfur vapor reacts with WO<sub>3</sub> and forms WO<sub>3-x</sub>, further evaporated at high temperatures and reacted with sulfur to produce WS<sub>2</sub> at the substrate surface.

Another simple CVD growth method for large continuous areas of WS<sub>2</sub> was reported involves a two-step process in which a thin W film is first deposited on the substrate, followed by S vapor reaction in inert atmosphere and high temperatures ( $\sim 300$ – $900$  °C). This method has been successfully used for up to 350  $\mu\text{m}$  of WS<sub>2</sub> on SiO<sub>2</sub>/Si. To do so, the W-coated substrate, the growth substrate, and sulfur powder were placed in an inert CVD furnace and exposed to a constant flow of 200 sccm Ar at a growth temperature of 950 °C for 5 min [50]. On the other hand, halide salts considerably lower the melting temperature of metal precursors, making it easier to grow 2D TMDCs by forming metal oxychlorides. For instance, the formation of volatile WOCl<sub>4</sub> and WO<sub>2</sub>Cl<sub>2</sub> species through salt addition

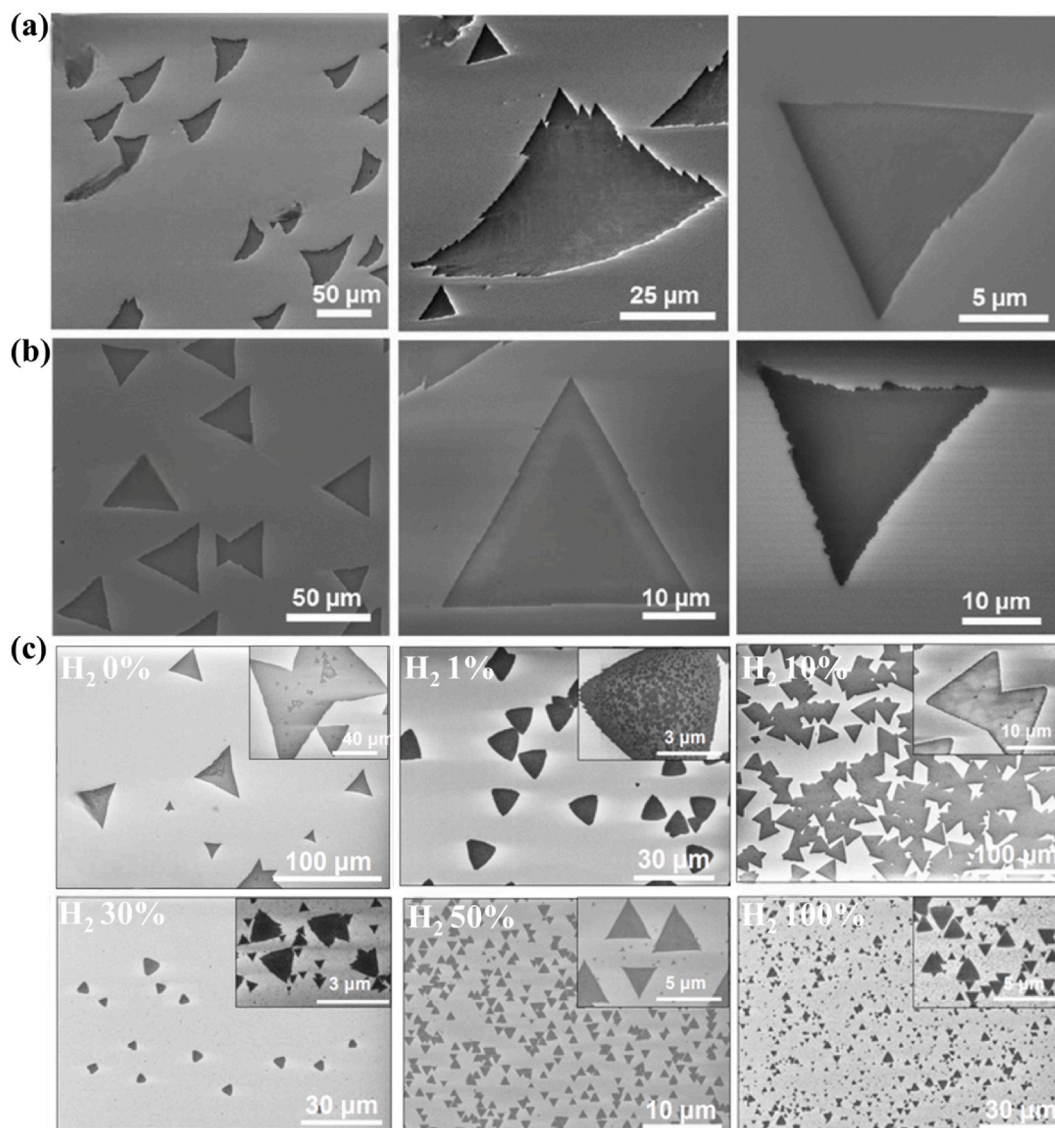


**Fig. 4.** H<sub>2</sub>-dependent WS<sub>2</sub> flakes morphology. a) SEM images of the WS<sub>2</sub> flakes grown under pure Ar gas flow, displaying jagged triangular edge. b) SEM images of the WS<sub>2</sub> flakes grown under mixed H<sub>2</sub> and Ar gas flow, displaying nearly equilateral with straight edges triangular WS<sub>2</sub>. Reproduced with permission from Ref. [55]. Copyright 2013, American Chemical Society. c) SEM images of the CVD-grown WS<sub>2</sub> under various H<sub>2</sub> concentrations from H<sub>2</sub>-free to 100 %, displaying the alignment evolution of the obtained WS<sub>2</sub> flakes in function of H<sub>2</sub> concentration. Reproduced with permission from Ref. [54]. Copyright 2017, American Chemical Society.

reduced the synthesis temperature and enlarged the crystal size of WS<sub>2</sub> compared to that without halide salts [51,52]. Similarly, adding Na has proven its potential in enhancing the chemical formation of monolayer WS<sub>2</sub>, lowering the energy barrier, and forming a large single crystal of WS<sub>2</sub> flakes, as we previously reported [21,53] (Fig. 3i-l).

Apart from the etching effect, which minimizes the formation of multilayer structure at each WS<sub>2</sub> domain center, H<sub>2</sub> also plays a key role in shaping and improving the alignment of the WS<sub>2</sub> flakes during the growth process [54,55]. Thus, the CVD growth of WS<sub>2</sub> flakes under pure Ar carrier gas flow mostly display an asymmetrical and jagged triangular edge (Fig. 4a). In comparison, introducing H<sub>2</sub> gas flow leads to the growth of nearly equilateral with straight edges triangular WS<sub>2</sub> (Fig. 4b and c). In particular, the chemical reduction of WO<sub>3</sub> into volatile WO<sub>3-x</sub> by H<sub>2</sub> creates a WO<sub>3-x</sub>-rich environment for the WS<sub>2</sub> growth, resulting in a stable triangular shape. H<sub>2</sub> also reduces multilayer formation and removes unstable defects during synthesis, forming pure-phase WS<sub>2</sub>. Table 1 summarizes some previously reported CVD growth of WS<sub>2</sub> with and without using H<sub>2</sub> under various growth conditions.

## 2.2. Metal-organic chemical vapor deposition (MOCVD)

Metal-organic chemical vapor deposition (MOCVD) is a subclass of conventional CVD; utilizes organic or metal-organic compound precursors as source materials for atomic thin film deposition [67,68]. During the MOCVD process, the desired growth atoms are usually combined with other complex organic molecules, which are further carried over the targeted substrate, decomposed by heat, and then deposited as a thin film with a high crystallinity following the atom-by-atom growth process. Therefore, the quality of the grown films can be engineered through the atomic composition variation to meet specific requirements. Using MOCVD, a successive series of surface reactions occurs, including precursor molecules adsorption, surface kinetics, nucleation, growth, and desorption of the volatile molecules. The working principle of the MOCVD growth method is illustrated in Fig. 5a, depicting the aforementioned growth steps involved in synthesizing 2D materials.

Recently, MOCVD has been utilized for 2D TMDCs growth due to its numerous pros, including uniform growth within a large-scale, precise control over both metal and chalcogen precursors, and the accessibility for controlling the composition and morphology of the grown substrate [69–71]. Kang et al. [72] conducted for the first time the large-scale synthesis of MoS<sub>2</sub> and WS<sub>2</sub> using MOCVD based on ethylene disulfide ((C<sub>2</sub>H<sub>5</sub>)<sub>2</sub>S), tungsten hexacarbonyl (W(CO)<sub>6</sub>), molybdenum hexacarbonyl (Mo(CO)<sub>6</sub>), and H<sub>2</sub> gas-phase precursors with Ar gas carrier. The MOCVD-grown WS<sub>2</sub> and MoS<sub>2</sub> films onto 4-inch substrates were further exploited to manufacture approximately 8000 field-effect transistor (FET) devices (Fig. 5b) with a field-effect mobility of 18 cm<sup>2</sup>V<sup>-1</sup>s<sup>-1</sup> (Fig. 5c).

Although MOCVD is described as versatile and scalable and allows for precise control over film stoichiometry, it still has an extremely low growth rate, and high production costs hinder the widespread use of its applications. Furthermore, the conventional hot-wall chamber MOCVD considered a high energy consumption technique, added to the complex growth process due to the possible decomposition of precursors during their carriage to the substrate. To overcome these issues, Choudhury et al. [73] suggested the usage of the cold-wall CVD chamber to synthesize WS<sub>2</sub> films within a reduced growth time of 30 min, as depicted in Fig. 5d. Contrary to the conventional hot-wall MOCVD, diethyl sulfide (DES-(C<sub>2</sub>H<sub>5</sub>)<sub>2</sub>S) as the S source was found inappropriate for cold-wall MOCVD system, as it can lead to the formation of graphitic carbon, which inhibits the growth of WS<sub>2</sub> and its lateral extension. In comparison, H<sub>2</sub>S is a good S precursor for the cold-wall MOCVD system, leading to the growth of WS<sub>2</sub> films with a relatively large grain size without any contamination related to carbon species (Fig. 5e and f). On the other hand, the reactivity of H<sub>2</sub>S towards the metal-containing precursor enables low-temperature processes (175–430 °C) compared to other S sources, including S<sub>8</sub> (300–500 °C). However, its toxic nature presents a concern; looking for other substitutes for H<sub>2</sub>S is therefore a high priority. Accordingly, Cwik et al. [69] demonstrated for the first time the usage of imido-amidinato complexes and elemental sulfur as precursors for the large-area synthesis of WS<sub>2</sub> and MoS<sub>2</sub> via cold-wall MOCVD. By using elemental sulfur instead of the toxic H<sub>2</sub>S precursor, the safety precautions of the MOCVD growth process can be significantly reduced, thus providing a cost-effective solution and offering a complete substitution for H<sub>2</sub>S. Similarly, Grundmann et al. [74] benefited from the similar lattice symmetry of WS<sub>2</sub> with the sapphire substrate for epitaxial coalescence of WS<sub>2</sub> films using tungsten hexacarbonyl (WCO) and di-tert-butyl sulfide (DTBS), and N<sub>2</sub> as carrier gas. Under optimized growth conditions,

**Table 1**  
Summary of previously reported WS<sub>2</sub> growth following atmospheric CVD with and without H<sub>2</sub> usage.

Carrier Gas	Growth temperature (°C)	Growth time (min)	Growth rate (μm/min)	Maximum edge length (μm)	Ref
Ar	950	5	74.0	370	[50]
Ar	1100	15	40	600	[56]
Ar	1070	15	17.1	256	[57]
Ar	900	10	23.3	233	[58]
Ar	900	10	39.4	394	[59]
Ar	750	30	2.3	70	[60]
Ar	860	60	6.2	370	[49]
Ar	750	5	35.6	178	[61]
Ar	800	5	12	60	[62]
Ar	875	5	92	460	[21]
Ar + H <sub>2</sub>	800	20	10	200	[63]
Ar + H <sub>2</sub>	750–850	3	100	300	[64]
Ar + H <sub>2</sub>	700–850	5	80	400	[51]
Ar + H <sub>2</sub>	850	10	21	210	[65]
Ar + H <sub>2</sub>	900	30	14.4	433	[66]

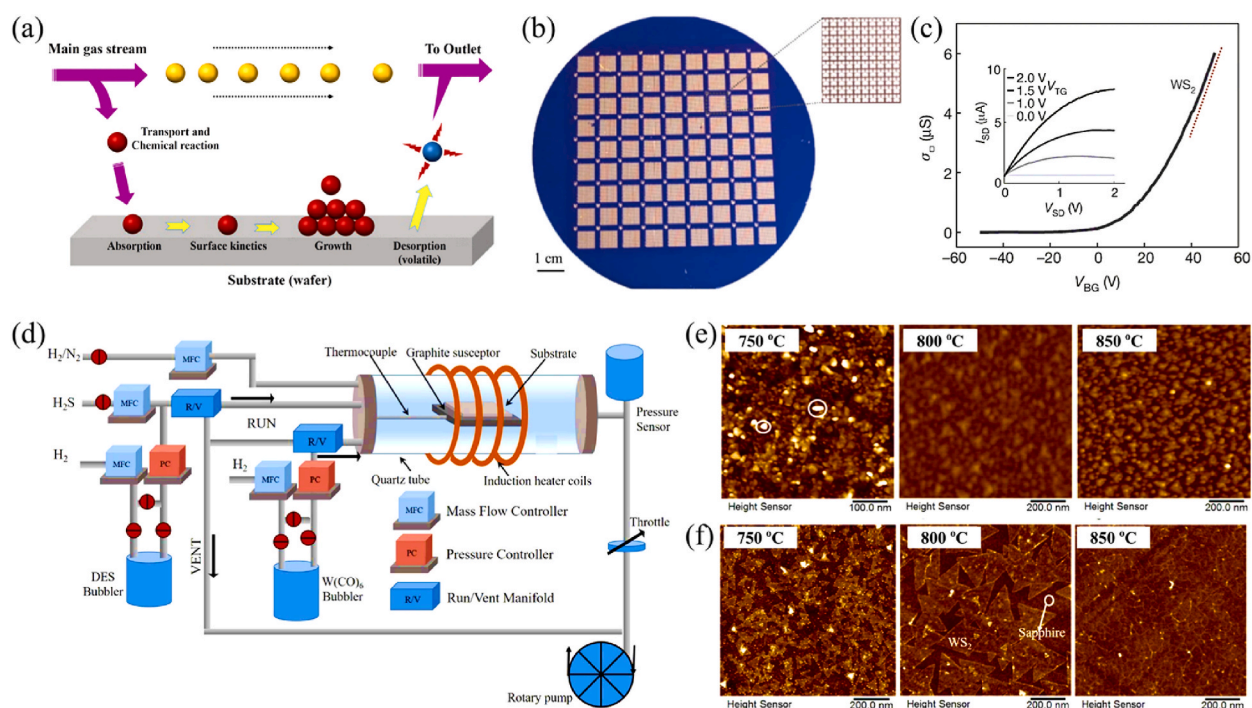


**Fig. 5.** MOCVD growth of  $\text{WS}_2$ . a) Schematic illustration of the MOCVD growth mechanism. Reproduced with permission from Ref. [8]. Copyright 2017, Elsevier B.V. b) Batch-fabrication of  $\text{MoS}_2$  FETs on a 4-inch wafer. Inset zoomed photograph of one square incorporating 100 FETs. c) Transfer characteristics of the grown monolayer  $\text{WS}_2$ -based FET. Reproduced with permission from Ref. [72]. Copyright 2015, Springer Nature. d) Schematic description of the cold-wall MOCVD system. e) AFM images of  $\text{WS}_2$  films grown at 750 °C, 800 °C and 850 °C using  $\text{W}(\text{CO})_6$  and DES and  $\text{W}(\text{CO})_6$  as tungsten sources and  $\text{H}_2\text{S}$  precursor. Reproduced with permission from Ref. [73]. Copyright 2018, American Chemical Society.

following this hydrogen sulfide ( $\text{H}_2\text{S}$ )-free, a fully coalesced  $\text{WS}_2$  monolayer was achieved, whereas its implementation into a light-emitting device yielded a bright red emission.

### 2.3. Atomic layer deposition (ALD)

Atomic Layer Deposition (ALD) is a layer-by-layer gas phase chemical process that allows the deposition of atomically thin films. While ALD has been widely performed for oxide materials synthesis, it has also been successfully implicated for several binary sulfide materials, including  $\text{SnS}$ ,  $\text{TiS}_2$ ,  $\text{Li}_2\text{S}$ ,  $\text{MoS}_2$ , and  $\text{WS}_2$ . Compared to the CVD growth process involving a continuous supply of precursors, ALD relies on the sequential delivery of precursors, leading to a layer-by-layer growth mode of thin films.  $\text{H}_2\text{S}$  and  $\text{WF}_6$  are commonly employed as the sources of S and W for the ALD synthesis of  $\text{WS}_2$  films [75–78]. Such a growth process is based on a ternary reaction cycle involving  $\text{WF}_6$  reaction,  $\text{H}_2$  plasma exposure, and  $\text{H}_2\text{S}$  reaction [78]. Goven et al. [77] resumed the ALD growth mechanism of  $\text{WS}_2$  into four main governing steps: gas precursor adsorption, adatom diffusion, and surface reactions, incorporation into  $\text{WS}_2$  crystals, followed by crystal ripening, and lastly, the coalescence of the  $\text{WS}_2$ .

Song et al. [79] reported the growth of  $\text{WS}_2$  at a wafer-scale via ALD using tungsten oxide ( $\text{WO}_3$ ) and  $\text{H}_2\text{S}$  precursors, as depicted in Fig. 6a. By varying the number of ALD cycles, the number of layers can be controlled effectively, leading to a controllable synthesis of mono-, bi-, and tetralayer  $\text{WS}_2$  on  $\text{SiO}_2$  substrate (Fig. 6b–e). The synthesized ALD monolayer  $\text{WS}_2$  was implemented into top-gated FETs configuration, leading to n-type conduction with electron mobility of  $3.9 \text{ cm}^2 \text{ V}^{-1} \text{ s}^{-1}$  (Fig. 6f). Additionally, the authors discussed the high conformal synthesizing of ALD and demonstrated the possibility of growing 1D  $\text{WS}_2$  nanotubes within a controllable thickness based on the sulfurization of Si nanowires deposited  $\text{WO}_3$  films. Besides, Delabie et al. [75] discussed synthesizing atomic layers  $\text{WS}_2$  using ALD at low growth temperatures (300–450 °C). The suggested growth protocol involves the usage of  $\text{WF}_6$  and  $\text{H}_2\text{S}$  as precursors, the semiconductor-compatible thin solid Si, and the  $\text{H}_2$  plasma as reducing agents without any annealing requirement. Interestingly, by increasing the growth temperatures from 300 to 450 °C, the orientation of the crystal structure was deformed from basal planes with parallel orientation to the substrate to a more randomly oriented crystal grain. Indeed, the  $\text{H}_2$  plasma is essential in synthesizing  $\text{WS}_2$  due to its reduction capability of the  $\text{WF}_6$  from the +6 oxidation state to +4, which allows for the formation of metallic W species during the ALD growth process. In addition to providing the necessary W precursor species,  $\text{H}_2$  plasma-assisted atomic layer deposition (ALD) was advantageous for achieving conformal deposition of  $\text{WS}_2$  onto narrow fins 3D structures [77]. However, as an alternative to  $\text{H}_2$  plasma, Heyne et al. developed an amorphous Si sacrifice layer as a reducing agent for converting  $\text{WF}_6$  to metallic W at a moderate temperature of 450 °C into the ALD system [80]. The obtained  $\text{WS}_2$  layers display a random basal plane orientation, which possesses the recrystallization capability toward larger crystals growth in selective deposition on large substrates

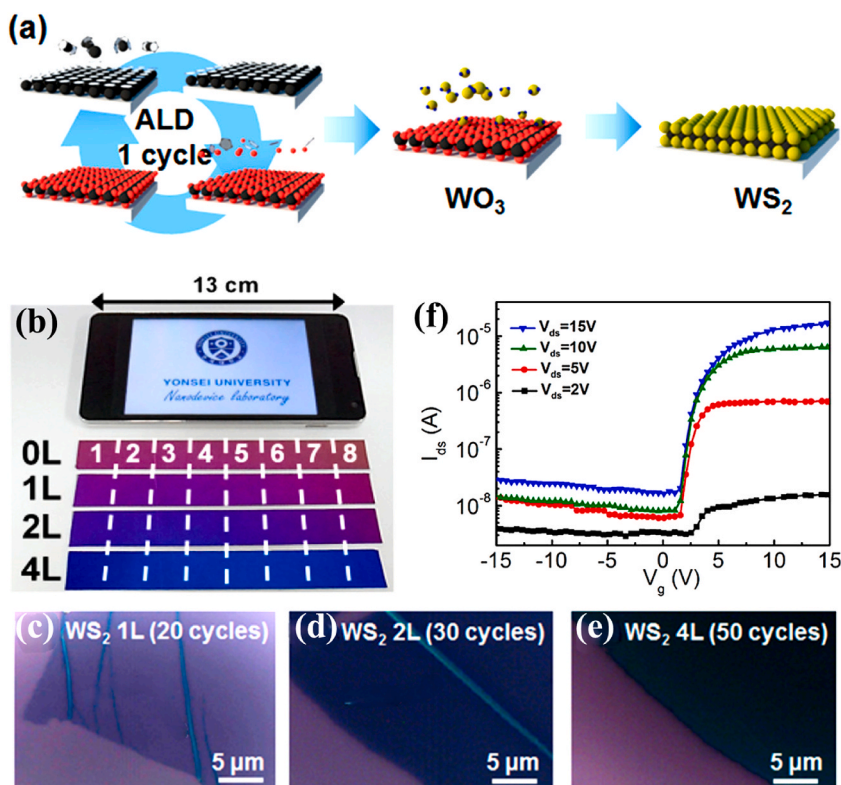


**Fig. 6.** ALD growth of WS<sub>2</sub>. a) Working principle of ALD. b) Large-area and controllable thickness growth of WS<sub>2</sub> on Si/SiO<sub>2</sub> substrate. c-e) Optical images of the transferred mono-, bi-, and tetralayer WS<sub>2</sub> to SiO<sub>2</sub> substrate, respectively. f) Transfer characteristics of WS<sub>2</sub> FET displaying n-type conduction behavior with electron mobility of 3.9 cm<sup>2</sup> V<sup>-1</sup> s<sup>-1</sup>. Reproduced with permission from Ref. [79]. Copyright 2013, American Chemical Society.

and heterostructure creation, making it a prominent method to stride numerous spintronics-, optics-and thin-film transistor (TFTs)-based applications.

In summary, ALD presents an effective technique for the growth of atomically thin WS<sub>2</sub> films due to its excellent growth control mechanism at the atomic level and low temperature. Such a unique growth mechanism can be utilized on large-area substrates, including features of 3D structures with high aspect ratios. Moreover, ALD is attractive for many advanced applications due to its compatible low process temperature. However, the ALD-grown films usually tend to be polycrystalline, non-uniform in thickness and have a small grain size, which can severely degrade their potential in electronic and optoelectronic applications. Additionally, the MOCVD nature of using expensive and highly sensitive precursors is still a big concern. Table 2 summarizes the pros and cons of CVD, MOCVD, and ALD growth techniques for WS<sub>2</sub>-based nanostructures.

**Table 2**  
Comparison of CVD, MOCVD, ALD methods advantages and disadvantages.

Techniques	Advantages	Disadvantages
Chemical Vapor Deposition (CVD)	<ul style="list-style-type: none"> <li>● High deposition rate</li> <li>● Simple setup</li> <li>● Possibility of mass production</li> <li>● Low Cost</li> </ul>	<ul style="list-style-type: none"> <li>● High temperature requirement</li> <li>● Low repetition rate</li> </ul>
Metal-Organic Chemical Vapor Deposition (MOCVD)	<ul style="list-style-type: none"> <li>● High repetition rate</li> <li>● High quality</li> </ul>	<ul style="list-style-type: none"> <li>● Time consuming</li> <li>● High cost</li> <li>● Precursors toxicity</li> </ul>
Atomic Layer Deposition (ALD)	<ul style="list-style-type: none"> <li>● High repetition rate</li> <li>● Good uniformity and conformality</li> <li>● Low substrate temperature</li> </ul>	<ul style="list-style-type: none"> <li>● High cost</li> <li>● Complex growth process</li> <li>● High material waste</li> <li>● Long time required for the chemical reactions</li> </ul>

### 3. Properties

#### 3.1. Crystal structure

The crystal structure of WS<sub>2</sub> is composed of stacked layers [11]. Each layer comprises three atomic planes arranged in a hexagonal pattern, with a W metal plane sandwiched between two S atom planes, resulting in an S–W–S structure. The layers are separated by a distance of approximately 0.65 nm without dangling bonds, making the surface extremely stable and non-reactive. These layers are held together by weak van der Waals interactions, allowing the easy exfoliation of WS<sub>2</sub> crystal. The coordination of W in the 2H phase WS<sub>2</sub> (1H phase for single layer) is defined as trigonal prismatic. Meanwhile, the octahedral coordination is present in the meta-stable 1T phase WS<sub>2</sub> [13]. Other polymorphs based on stacking differences and lattice distortion were identified and detailed elsewhere [81].

WS<sub>2</sub> exhibits a layer-dependent bandgap, as depicted in Fig. 7a. The monolayer structure of WS<sub>2</sub> crystal has a direct band gap, with the valence band maximum (VBM) and conduction band minimum (CBM) stationed at the K point. As the number of layers increases, the VBM shifts toward  $\Gamma$  point while the CBM is relocated between K and  $\Gamma$  points at Q point. Like other semiconducting TMDCs, the band gap value of WS<sub>2</sub> decreases with increasing layer number [82]. At Q<sub>c</sub> and  $\Gamma_v$  (with c and v are the conduction and valence bands, respectively), the contribution from the S p<sub>z</sub> orbitals becomes significant, affecting the transition from a direct band gap in monolayer WS<sub>2</sub> to an indirect band gap in bilayer and bulk structure of WS<sub>2</sub>. The close proximity of S p<sub>z</sub> orbitals in different layers leads to significant hopping, altering the energies of Q<sub>c</sub> and  $\Gamma_v$ . Therefore, the transition from direct to indirect band gap results from interlayer hopping [83]. Such a transition from indirect to direct band structure of WS<sub>2</sub> results in strong photoluminescence (PL), as seen in the inset of Fig. 7b. As the number of layers decreases, the PL intensity from direct interband transitions increases significantly and reaches its maximum with the monolayer structure of WS<sub>2</sub>. Besides the photoluminescence emission resulting from the direct transition at the K point, which corresponds to the A exciton, another less intense PL peak (B) is also detected at a higher energy level (Fig. 7c). The A and B emissions come from splitting the valence band at the K points, mainly due to spin-orbit coupling [84,85]. According to theoretical predictions, the energy at which the I peak emerges from the indirect band gap transition gradually shifts towards higher values and disappears at the monolayer limit [84].

Raman spectroscopy is a highly effective and non-destructive technique for characterizing 2D materials [86]. In the case of bulk WS<sub>2</sub>, using backscattering geometry under 488 nm laser wavelength excitation, Raman spectrum displays both E<sub>2g</sub>( $\Gamma$ ) and A<sub>1g</sub>( $\Gamma$ ) modes correspond to the first-order modes at the Brillouin zone centered at 356 cm<sup>-1</sup> and 418 cm<sup>-1</sup> (Fig. 7d). The spectrum also displays another zone-edge mode activated by disorder (LA(M)) at 176 cm<sup>-1</sup>, which has been identified as the longitudinal acoustic mode at the M point and represents the in-plane collective movements of the lattice atoms [87]. The Raman spectrum of WS<sub>2</sub> crystal is dependent on the excitation wavelength [88]. Therefore, other Raman peaks are thought to be resulted from multi-phonon combinations of the aforementioned modes under higher laser wavelength excitation. Under 514.5 nm laser wavelength excitation, Berkdemir et al. [88] recorded a plentiful Raman spectrum with multiple second-order peaks. Moreover, the strongest peak is ascribed to 2LA(M) mode at 352 cm<sup>-1</sup>, and the E<sub>2g</sub>( $\Gamma$ ) recorded a coincidence with 2LA(M) peak. The abundance of Raman peaks excitation at

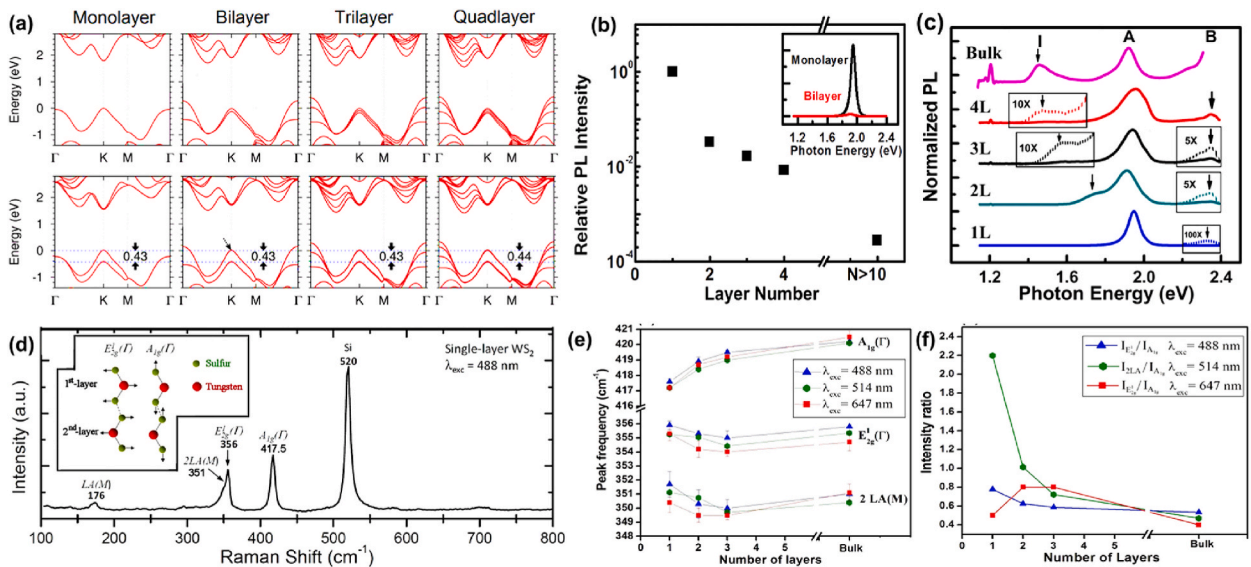


**Fig. 7.** WS<sub>2</sub> layer-dependent band structure and Raman spectroscopy phonon Modes. a) WS<sub>2</sub> layer-dependent band structure without (upper panel) and with (down panel) spin-orbit coupling. The valence band splitting at K point remains constant at approximately 0.43 eV as going from monolayer to quadlayer. b) Layer-dependent relative PL intensity. Inset is PL spectra of monolayer and bilayer WS<sub>2</sub>. c) WS<sub>2</sub> Thickness-dependent normalized PL spectra. Reproduced with permission from Ref. [84]. Copyright 2013, Springer Nature. d) Raman spectroscopy of single layer WS<sub>2</sub> using 488 nm light excitation. Inset displays the atomic displacements of E<sub>2g</sub>( $\Gamma$ ) and A<sub>1g</sub>( $\Gamma$ ) modes. e) Layer-dependent peak frequencies, and f) Relative intensity ratio using various light excitations. Reproduced with permission from Ref. [88]. Copyright 2013, Springer Nature.

514.5 nm is due to the double-resonance Raman process, which stimulates the second-order Raman peaks [87,88]. Similar results, with rich Raman peaks, were also observed under the excitation by 532 and 647 nm laser wavelengths [61,89].

Multiple studies reveal the high sensitivity of the Raman spectrum to the layer counting and doping level of WS<sub>2</sub> [88,90]. By increasing the number of layers, A<sub>1g</sub>(Γ) mode displays a blueshift, whereas E<sub>2g</sub>(Γ) and 2LA(M) phonon modes exhibit a slight redshift (Fig. 7e). On the other hand, the relative intensity of the significant Raman peaks is also influenced by the number of layers (Fig. 7f). Besides, another fascinating aspect of the Raman spectroscopy is the ratio intensity of 2LA(M)/A<sub>1g</sub>(Γ), which is mostly higher than 2 for the single layer of WS<sub>2</sub> when excited with 514.5 nm laser wavelength excitation, serving as a fingerprint to distinguish single layer from the multi-layer structure of WS<sub>2</sub> [88]. Additionally, Raman spectrum is also greatly influenced by the strain [91], where the E<sub>2g</sub>(Γ) mode is particularly vulnerable to the strain variation due to its expanded in-plane opposite displacements of W and S atoms. Thus, as the strain increases, the E<sub>2g</sub>(Γ) mode displays a redshift and subdivides into two sub-modes: E<sub>2g</sub><sup>1/2</sup> and E<sub>2g</sub><sup>3/2</sup>. On the other hand, the A<sub>1g</sub>(Γ) mode represents the perpendicular vibration of S atoms, and displays a high response to the doping level, leading to its softening and broadening by increasing the electron doping [92,93]. Consequently, when WS<sub>2</sub> is p-type doped, the A<sub>1g</sub>(Γ) mode experiences a p-type doping levels-dependent blueshift [94]. Overall, all these findings uplift the usefulness of Raman spectroscopy for the characterization and identification of physical properties of WS<sub>2</sub>.

### 3.2. Conductivity and light-matter interaction

Monolayer tungsten disulfide displays outstanding electrical properties among MX<sub>2</sub> material types (M = Mo, W and X = S, Se), which makes it a promising candidate for high-performance field-effect transistors (FETs). In addition, the greater effective hole mass and mobility suggest that hole transport experiences less scattering with phonons. The theoretical room temperatures hole and electron mobilities of the monolayer WS<sub>2</sub> have been estimated to be 540 and 320 cm<sup>2</sup> V<sup>-1</sup> s<sup>-1</sup>, respectively [95]. Whereas, if only long-wave acoustic phonons are considered, the theoretical simulation shows that the electron mobility of WS<sub>2</sub> monolayers is greater than 1100 cm<sup>2</sup> V<sup>-1</sup> s<sup>-1</sup> at room temperature [96]. Like other semiconductor TMDCs, in the visible light range, WS<sub>2</sub> exhibits a strong peak ascribed to the state density Van Hove singularities [97]. These Van Hove singularities enhance light-matter interaction and improve photon absorption, creating additional electron-hole pairs. Both experimental and theoretical studies indicate that monolayer WS<sub>2</sub> possesses the absorption ability of more than 10 % of incident light with a high absorption coefficient of approximately  $\approx 1.5 \times 10^6$  cm<sup>-1</sup>, demonstrating its strong light-matter interaction [98]. These findings showcase the tremendous promise of WS<sub>2</sub> in various photonic and optoelectronic applications.

### 3.3. Field emission properties

Electrons drawing from the surface of conducting and semiconducting materials, driven by a high external electric field under an ultra-high vacuum condition, is defined as quantum tunneling phenomenon also known as field emission (FE) [99]. This FE phenomenon finds diverse applications in various vacuum microelectronic devices, including flat panel displays, traveling wave tubes, and x-rays generation [100]. Driven by the notable high field enhancement factors attributed to nanoscale emission sites, the field emission of various nanomaterials featuring diverse dimensions and morphologies has been investigated [101].

WS<sub>2</sub>, with its lower band gap energy, limited number of dangling bonds, prolonged mechanical stability, and non-toxic nature over an extended period, emerges as an appealing nanomaterial for field emitter-based devices [102]. Consequently, there has been an exploration of WS<sub>2</sub> 2D nanosheets, heterostructures, and rolled sheet arrays for the development of field emitter-based devices, placing a particular emphasis on the design of exceptionally stable field emitter devices [100]. For instance, the spectral analysis of current fluctuations in WS<sub>2</sub> nanosheets-based emitters delved into the 1/f<sup>α</sup> type of noise with an α value approximately equal to 1.05 [103]. The variations in the emission current and the significant alterations in the α value were ascribed to the dual physiochemical process, namely the adsorption, migration, and/or desorption of residual gas species on the emitter's surface. On the other hand, WS<sub>2</sub> nanotube has shown potential in emitter-based devices. Viskadourous et al. [102] conducted a study wherein WS<sub>2</sub> nanotubes showcased efficient field emission (FE) performance with a low turn-on field of 1 V μm<sup>-1</sup>, a field enhancement factor of approximately 3526, and a consistent emission current stability sustained over an extended period of 18 h. In another study, Grillo et al. [104] followed the high temperature solid-gas synthetic method for the synthesis of Multiwalled WS<sub>2</sub> nanotubes using H<sub>2</sub>, H<sub>2</sub>S and tungsten oxide nanoparticles as precursor and reactive gases, respectively. The issued nanotubes demonstrate an impressive field emission current density up to 600 kA cm<sup>-2</sup> with a field-enhancement factor of 50 and a turn-on field of approximately 100 V μm<sup>-1</sup>. Overall, underscore the considerable potential of WS<sub>2</sub> in a variety of devices relying on field emission across various fields.

### 3.4. Biocompatibility and toxicity evaluation

Ongoing attempts are being made to discover the potential biomedical uses of tungsten disulfide. However, its toxic effects in living organisms are still a major hindrance, where the integration of WS<sub>2</sub>-based nanomedicine in a safe manner and a better understanding of its toxicity in living organisms is a critique key attributes of mainstream research. Although safety assessments of WS<sub>2</sub> are common in related studies, which is usually limited to mice or based on simple one-sided evaluation criteria. In addition, the absence of a standardized evaluation system presents an additional challenge in comparing various research studies outcomes, as they employ different dosages and methods of intake. In this subsection, we reviewed the recent studies on the biological toxicity of WS<sub>2</sub> to guide future investigations, where most toxicity studies were conducted in vitro. To illustrate, the biocompatibility of WS<sub>2</sub> within its Inorganic Fullerene-like Nanoparticles (IFWS<sub>2</sub>) and multiwall Inorganic Nanotube (INT-WS<sub>2</sub>) structures toward salivary gland cells

was investigated by Goldman et al. [105]. The toxicity of both structures was evaluated using RSC and A5 cells at different concentrations (0.22–100  $\mu\text{g}/\text{mL}$ ), in which both cell lines did not show any significant variations in their kinetic behavior or growth and survival rates. Additionally, such microstructures were observed in the cytoplasm, rather than the nucleus, and surrounded by a membrane, suggesting their biocompatibility and potential for medical applications. Appel et al. [106] conducted the cytotoxicity and genotoxicity examination of  $\text{WS}_2$  nanoparticles and  $\text{WS}_2$  nanosheet for *S. Typhimurium* TA100 bacteria and HEK293f human kidney cells. According to ROS test, mutagenic assessment, and live-dead fluorescence assay,  $\text{WS}_2$  did not trigger the high levels of ROS generation that typically result in cell death. Therefore, the *S. Typhimurium* bacteria did not display any significant mutations even after the exposition to a high concentration of  $\text{WS}_2$  (100  $\mu\text{g}/\text{mL}$ ) for an extended period of 24 h.

Nevertheless, it is worth noting that *in vitro* experiments cannot fully predict real-sample biological outcomes. To assess the posed toxicity by nanomaterials, researchers have studied both chronic and acute toxicity [107–109]. Correspondingly, Hao et al. [110] have conducted a 30-day *in vivo* toxicology test of three PEGylated TMDCs, including  $\text{WS}_2$ ,  $\text{MoS}_2$ , and  $\text{TiS}_2$ . Accordingly,  $\text{WS}_2$  showed more stability and longer *in vivo* retention than  $\text{MoS}_2$  and  $\text{TiS}_2$  due to its antioxidant response pros. Nonetheless,  $\text{MoS}_2$  was oxidized into water-soluble MoVI-oxide species, which led to its degradation and total excretion within one month. Furthermore, histological and blood analysis showed no significant long-term toxicity of  $\text{WS}_2$  at the tested dose. However, numerous side effects have been reported, such as hemolysis, platelet function, and coagulation [111]. To sum up, plenty of research highlights the remarkable biocompatibility and safety of  $\text{WS}_2$  in cell experiments. However, when considering its integration into human body, various studies still need to be carried out considering the side-effect of potential hazards such as thrombosis and inflammatory gene induction [111,112]. In addition, to advance  $\text{WS}_2$  clinical potential, a fitting toxicity evaluation is crucial to be promptly devised.

## 4. Biomedical applications of $\text{WS}_2$

### 4.1. Biosensing applications

#### 4.1.1. Optical biosensors

The adoption of optical measurement techniques in biosensing applications led to the creation of a new generation of biosensing platforms with high sensitivity down to single molecule detection [26]. Tungsten disulfide nanosheet, with its lowered background and high fluorescence quenching efficiency, affords an attractive sensing platform. DNA interaction with  $\text{WS}_2$  nanosheet

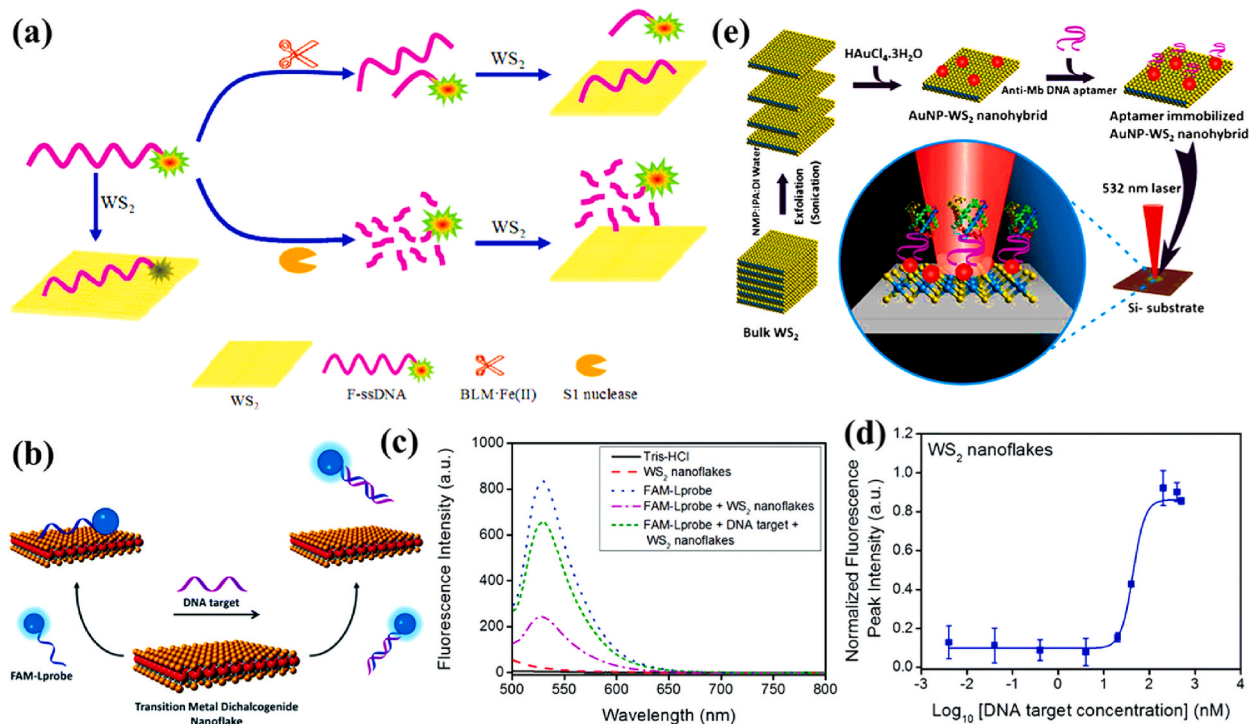


**Fig. 8.** Tungsten disulfide nanoarchitecture-based optical biosensors. a) Schematic illustration of bleomycin and nuclease biosensor's detection principle. Reproduced with permission from Ref. [113], Copyright 2015, Elsevier B.V. b) Schematic diagram of  $\text{WS}_2$ -based DNA detection using FAM-Lprobe DNA, and its associated c) fluorescence emission under various experimental conditions, and d) the extracted normalized fluorescence peak as varying the DNA target concentration. Reproduced with permission from Ref. [119], Copyright 2016, Royal Society of Chemistry. e) Schematic representative of the  $\text{WS}_2$ -based optical biosensor for myoglobin (MB) monitoring workflow. Reproduced with permission from Ref. [120], Copyright 2018, Springer Nature.

architecture-based optical biosensor platform has been widely performed for the detection of nuclease [113], protein CEA and DNA [114], metal ion [115], microRNA [116,117], and DNA glycosylases [118]. Qin et al. [113] successfully developed a sensing fluorescence platform for detecting bleomycin and nuclease based on WS<sub>2</sub> nanosheet (Fig. 8a). The working principle was based on WS<sub>2</sub>'s different affinity to different ssDNA lengths and its excellent fluorescence quenching ability advantages. The proposed sensor exhibits high sensitivity with a detection limit of 0.01 U mL<sup>-1</sup> for S1 nuclease and 0.3 nM for bleomycin within a wide linear range. Additionally, Yuan et al. [114] proposed a water-soluble WS<sub>2</sub> nanosheet based on a one-step sonication method, with which they proved its applicability in DNA detection through single-strand DNA (ssDNA) chains adsorption on the WS<sub>2</sub>. The interaction with other biomolecules disposed of the detachment of the adsorbed ssDNA, resulting in the restoration of the fluorescence. The developed fluorescence DNA biosensor exhibited an auspicious sensitivity with a LOD of 60 pM. In another work, Loo et al. [119] investigated the fluorescence quenching degree of MoS<sub>2</sub> and WS<sub>2</sub> nanoflakes using FAM-Lprobe as a fluorescent DNA oligonucleotide for DNA-related Alzheimer's disease detection (Fig. 8b–d). As a comparative study, both TMDCs nanoflakes displayed a similar fluorescence quenching degree; however, MoS<sub>2</sub> exhibited better performance over WS<sub>2</sub> regarding detection range and selectivity.

Additionally, it is noteworthy that nanoparticles incorporation into the WS<sub>2</sub> can increase the sensitivity. Parallel to this line of thought, Shorie et al. [120] suggested the development of a surface-enhanced Raman spectroscopy (SERS) biosensor based on AuNPs-decorated WS<sub>2</sub> for myoglobin (MB) detection. The utilized composite of AuNPs/WS<sub>2</sub> was functionalized with DNA aptamer of anti-MB (Fig. 8e), leading to a low limit of detection of 0.5 aM toward MB with high selectivity against hemoglobin (Hb) and bovine serum albumin (BSA). Though Wang et al. [121] reported the combination of WS<sub>2</sub> and aptamer-modified upconversion NPs to develop a sensitive, selective, and rapid optical *E. coli* biosensor (Fig. 9a). In this work, the WS<sub>2</sub> nanosheets are excellent energy acceptors because of their large adsorption spectrum, possibly enhancing the gadget's performance. Thus, such a fluorescent biosensor can be considered an observance platform of numerous bacterial pathogens via a simple alteration of the specific aptamer.

Besides the DNA and WS<sub>2</sub> nanosheet interaction, dye-labeled peptide substrate for the detection of disease biomarkers has also been investigated. Giving the example of Zuo et al. work [122], in which they used for the first time the fluorescence biosensor based on WS<sub>2</sub> nanosheet and peptide interaction for the detection of Alzheimer's biomarker disease  $\beta$ -secretase (BACE1). By measuring the fluorescence variation associated with the FAM-labeled peptide quenching, the developed biosensor displayed high sensitivity and selectivity with a low detection limit (LOD) of 66 pM. Additionally, Kang et al. [123] developed a photoluminescence detection

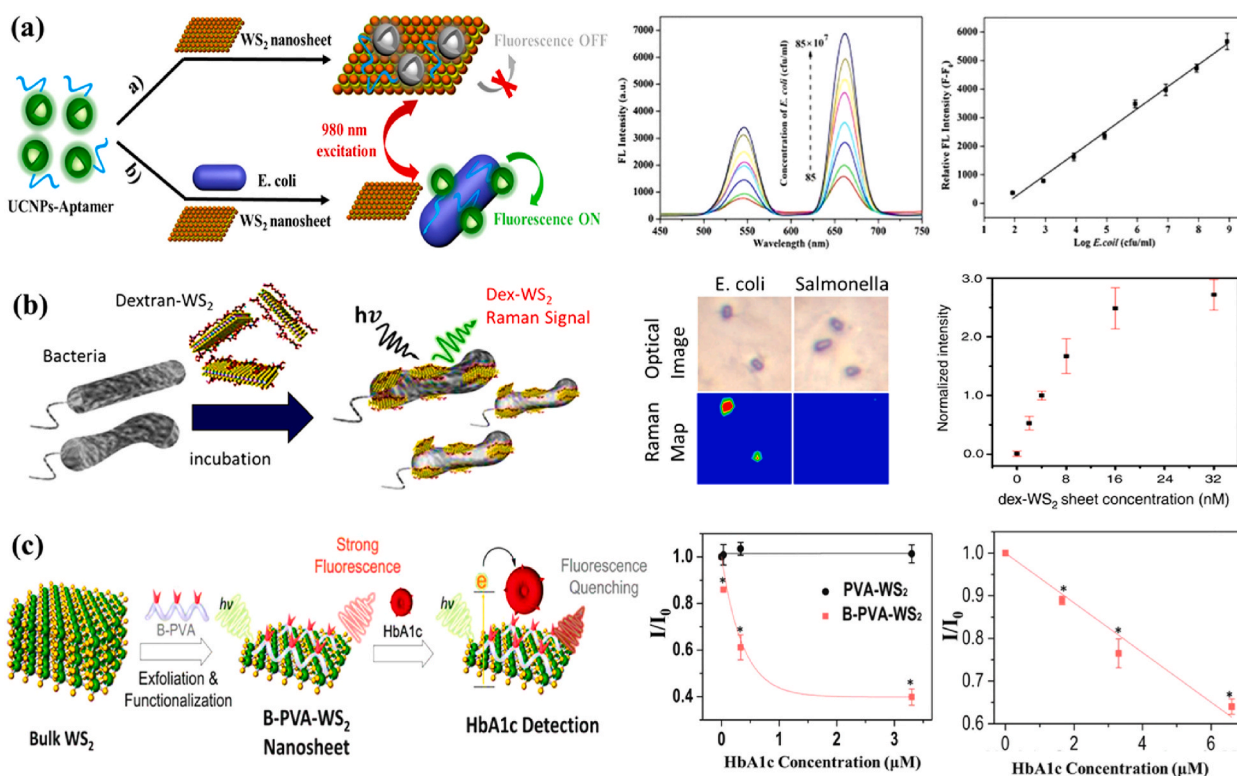


**Fig. 9.** a) Schematic illustration of WS<sub>2</sub>/UCNPs-based *Escherichia coli* fluorescence biosensor, and its associated fluorescence intensity and calibration curve at various *E. coli* concentrations. Reproduced with permission from Ref. [121]. b) Schematic illustration of dex-WS<sub>2</sub>-based bacteria monitoring using antibody-free detection strategy; Optical photographs and Raman mapping of single bacterium copy of *E. coli* and *Salmonella*, and the calibration curve of *E. coli* detection in the function of dex-WS<sub>2</sub> concentrations. Reproduced with permission from Ref. [123], Copyright 2018, Springer Nature. c) Schematic diagram of the WS<sub>2</sub> nanosheets-based HbA1c biosensor, and boronic-acid effect on PL quenching responses in the presence of HbA1c at various concentrations. Reproduced with permission from Ref. [124]. Copyright 2018, Wiley-VCH.

strategy for *E. coli* within a strong affinity of  $K_d = 11$  nM using an antibody-free manufacturing process (Fig. 9b). The working principle was based on dextran (dex)-functionalized WS<sub>2</sub> monolayers that were highly specific toward the *E. coli* O157:H7 strain than other *E. coli* strains tested. Interestingly, negligible binding was noticed for both *Staphylococcus aureus* and Salmonella. Compared to those based on antibody immobilization methods, the developed biosensor displays the advantages of being more easily prepared and showing less environmental fluctuations affect. In another work, Yang et al. [124] demonstrated the dual functionality of boronic acid-modified PVA (B-PVA) in the exfoliation and surface functionalization of the WS<sub>2</sub> nanosheets for fluorescence determination of glycosylated hemoglobin (HbA1c). The synthesized B-PVA-WS<sub>2</sub> using pulsed sonication process results in the creation of a specific sensitivity toward HbA1c due to the specific biorecognition moieties of boronic acid, whereas only PVA-WS<sub>2</sub>, without boronic-acid, displays no fluorescence variation upon the addition of HbA1c (Fig. 9c). The developed optical biosensor displays a high sensitivity and selectivity toward HbA1c as against glucose within an LOD of  $3.3 \times 10^{-8}$  M.

Optical biosensors can be classified into direct and indirect biosensor techniques. While the first class requires the complex formation on the transducer surface, the second requires the implication of chromophores and fluorophores as labeling tagged for binding identification and signal amplification. Although the advantage of generating higher signal levels using indirect techniques, they are limited by high reagent costs due to the labeling process and non-specific binding. Tungsten disulfide quantum dots (WS<sub>2</sub>-QD) also stands as a potential candidate for optical biosensing applications owing to their excellent essential fluorescent features [125]. Zhao et al. [126] used the WS<sub>2</sub>-QD as an efficient probe for fluorescence detection of dopamine within an LOD as low as  $3.3 \mu\text{M}$ . Similarly, Irani-nezhad et al. [125] implicated the usage of WS<sub>2</sub>-QD and fluorescein as a ratiometric fluorescence probe for the detection of Cefixime (CEF). Furthermore, Guo et al. [127] detailed the manufacturing of luminescence from WS<sub>2</sub> dots via a simple hydrothermal procedure through reduced L-glutathione and sodium tungstate. The obtained nanocomposite was further implicated as a fluorescent

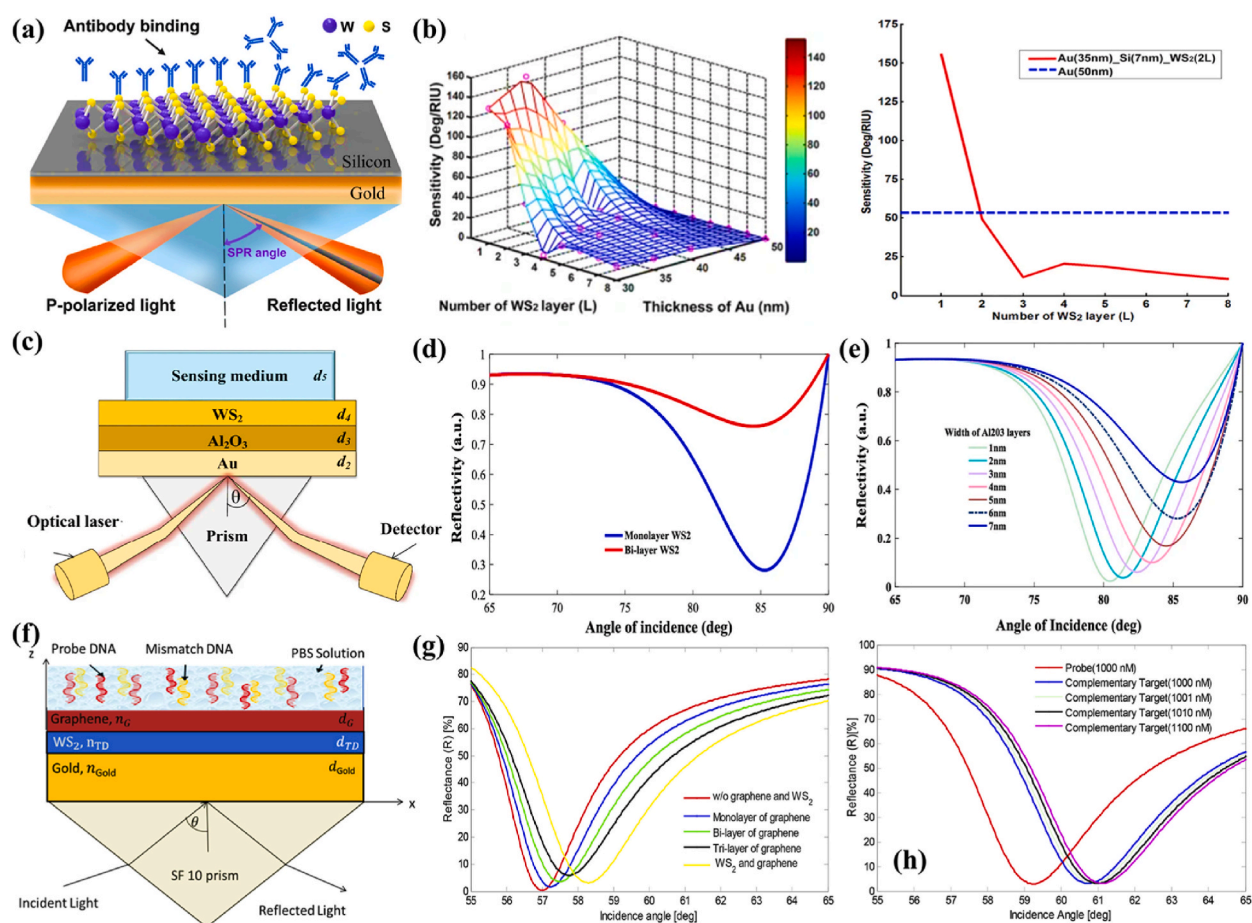


**Fig. 10.** WS<sub>2</sub>-based SPR biosensor. (a) Schematic illustration of silicon-WS<sub>2</sub> based SPR biosensor, (b) the sensitivity variation as a function of WS<sub>2</sub> layers number, and the thickness of Au thin film. Reproduced with permission from Ref. [128]. Copyright 2016, Springer Nature. (c) Schematic diagram of WS<sub>2</sub> and Al<sub>2</sub>O<sub>3</sub> based SPR biosensor, and the reflectivity versus angle of incidence of the developed SPR in the function of (d) WS<sub>2</sub> layers, and (e) Al<sub>2</sub>O<sub>3</sub> thickness. Reproduced with permission from Ref. [129]. Copyright 2019, Springer Nature. (f) Schematic of the developed graphene coated WS<sub>2</sub> based SPR biosensor. (g) Reflection intensity spectra at various numbers of graphene film. (h) DNA sensing efficiency of the developed graphene-coated WS<sub>2</sub> configuration. Reproduced with permission from Ref. [130]. Copyright 2018, Elsevier B.V. (For interpretation of the references to color in this figure legend, the reader is referred to the Web version of this article.)

probe for the specific quantification of nitrofurazone (NFZ) in water samples and nasal drops. The associated emitted fluorescence signal upon the presence of NFZ within a linear range of 0.17–166  $\mu\text{mol L}^{-1}$  was investigated, and the LOD was found to be 0.055  $\mu\text{mol L}^{-1}$ .

Recently, Surface plasmon resonance (SPR) has gained much attention in the fundamental optical-based biosensing application because of its appealing achievement in multiple fields, including the biochemical discovery and healing of disease.  $\text{WS}_2$ , with its prominent optical characteristics as a sensing layer or sandwiched between metal and sensing layers, has uplifted the usage of SPR biosensors through the noticeable performance increase where the detection accuracy, quality factor, and sensitivity are the key concerns. Ouyang et al. [128] demonstrated the feasibility of the coupled structure of silicon nanosheet and 2D  $\text{MX}_2$  film in enhancing SPR biosensors (Fig. 10a). Four models were suggested based on silicon, and each of  $\text{MoS}_2$ ,  $\text{WSe}_2$ ,  $\text{MoSe}_2$ , and  $\text{WS}_2$  as a sensing film at five excitation wavelengths (600, 633, 660, 785, and 1024 nm). Consequently, all four developed structures displayed an enhanced sensing performance compared to that made of conventional Au thin film. Whereas, using thick  $\text{MX}_2$  via an excessive layer was found to reduce the biosensor sensitivity and uplift the energy loss. Therefore, an attempt to optimize the structure toward higher sensitivity through multiple combinations between layer numbers and thickness of Au film was carried out (Fig. 10b). Accordingly, the highest sensitivity of 155.68 Deg/RIU was achieved using 7 nm of  $\text{WS}_2$  and 35 nm of Au under an excitation wavelength of 600 nm. However, a higher sensitivity of 227.5 Deg/RIU was achieved by Nur et al. [129] using one layer of  $\text{WS}_2$  and six layers of  $\text{Al}_2\text{O}_3$  with a quality factor of 28.26 RIU $^{-1}$  and detection accuracy of 1.1123 (Fig. 10c–e). On the other hand, the deposition of graphene film into  $\text{WS}_2$ -based SPR biosensing has shown immense enhancement in biosensing efficiency and sensitivity. Rahman et al. [130] suggested the insertion of  $\text{WS}_2$  between the metal film (Au) and the graphene-based SPR biosensor for DNA hybridization detection (Fig. 10f–h). The authors found the suggested SPR biosensor structure more effective than the conventional model of the graphene-based SPR biosensor. Also, the authors stated that the suggested SPR biosensor model could provide a novel route for detecting biomolecule interaction.

#### 4.1.2. Electrochemical biosensors

For decades, electrochemical biosensors-based screen-printed electrodes and semiconductors compounds were massively studied and implicated for numerous applications in multiple fields [131–136]. TMDCs incorporation into the electrochemical sensing interface has led to the development of novel biosensors with more favorable and enhanced performances [137]. Among TMDCs,  $\text{WS}_2$  has shown a promising capability for ssDNA and dsDNA discrimination, which catalyzes the usage of TMDCs nanosheets in the field of biosensing [114,116]. In line with this fact, Yang et al. [138] combined the poly (indole-6-carboxylic acid) (PIn6COOH) with  $\text{WS}_2$  nanosheets as a sensing interface for the development of an electrochemical DNA biosensor. Firstly, the (PIn6COOH) was electropolymerized on the  $\text{WS}_2$  nanosheet-modified carbon paste electrode (CPE), then the ssDNA probe was non-covalently attached to the nanocomposite substrate through  $\pi$ - $\pi$  interaction (Fig. 11a–c). Following this strategy, a detection limit of  $2.3 \times 10^{-18}$  mol/L was achieved under a dynamic concentration of PIK3CA gene ranging from  $10^{-17}$  to  $10^{-11}$  mol/L. In another work, Li et al. [137] developed an electrochemical biosensor based on a self-assembled DNA aptamer at  $\text{WS}_2$  nanoarchitecture for the detection of adenosine triphosphate (ATP). Firstly, the thiol-terminated DNA group (-SH DNA) was tethered to the Au substrate, then  $\text{WS}_2$  nanosheets

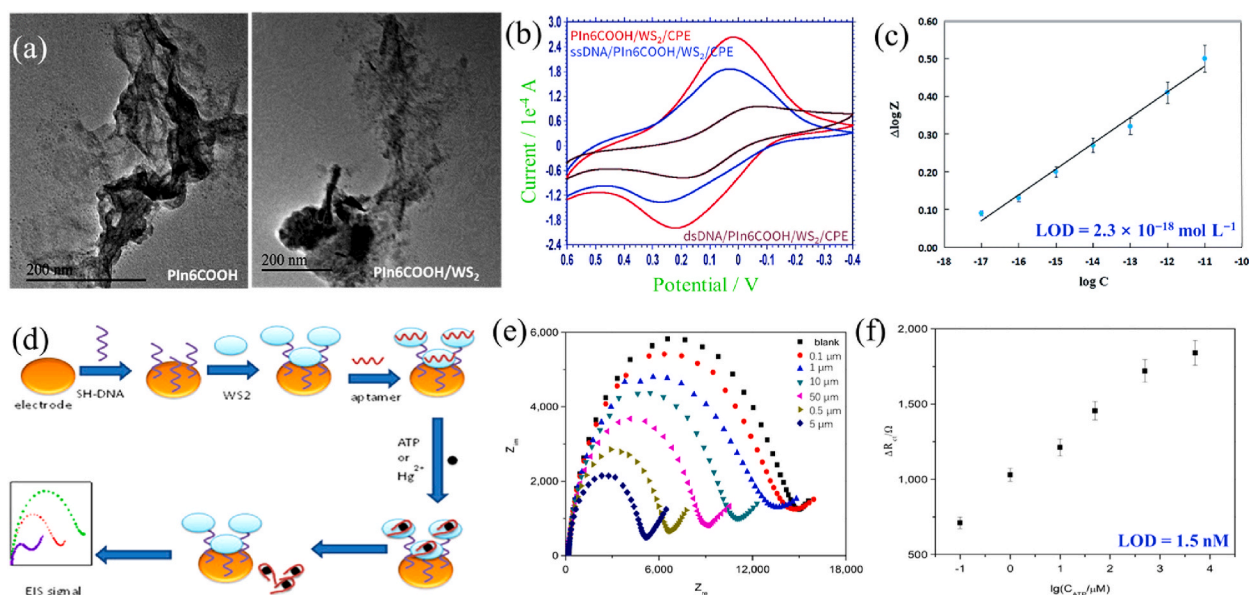


**Fig. 11.**  $\text{WS}_2$ -based electrochemical biosensor. (a) TEM image of PIn6COOH and PIn6COOH/ $\text{WS}_2$ , (b) Cyclic voltammograms of PIn6COOH/ $\text{WS}_2$  based PIK3CA biosensor at different functionalization steps. (c) Calibration curve of the developed PIn6COOH/ $\text{WS}_2$ -based PIK3CA biosensor. Reproduced with permission from Ref. [138]. Copyright 2019, Royal Society of Chemistry. (d) Working principle of  $\text{WS}_2$  modified aptamer-based ATP and  $\text{Hg}^{2+}$  biosensor. (e) EIS response of ATP detection at different concentrations. (f) Calibration curve of the developed  $\text{WS}_2$  modified aptamer biosensor for ATP detection. Reproduced with permission from Ref. [137]. Copyright 2017, Elsevier B.V.

were attached to the DNA layer on account of the strong affinity interaction between DNA and WS<sub>2</sub>. Further, the binding aptamer of adenosine triphosphate was immobilized to the WS<sub>2</sub> nanosheet (Fig. 11d–f). What is more, Li et al. followed the same immobilization strategy but for the detection of Hg<sup>2+</sup> through mercury-specific aptamer (MSO) immobilization, in which the developed electrochemical biosensor still exhibited its high sensitivity, selectivity, and stability. On the other hand, using WS<sub>2</sub> nanotubes functionalized with carboxylic acid (WS<sub>2</sub>-COOH), Palomar et al. [23] have unlocked the potential application of WS<sub>2</sub> in catechol and dopamine quantification (Fig. 12a–e). Herewith, authors used the dispersion-filtration transfer method for nanotubes deposition on GCE, whereas EDC/NHS coupling reaction was used for surface functionalization with tyrosinase enzyme. Following this simple handling method of WS<sub>2</sub> nanotubes, the authors state that the recorded performance of the developed sensor is comparable to those made of carbon nanotubes, which makes it a promising nanomaterial for biosensing design and applications.

The combination of nanomaterials, including nanoparticles (NPS) with the electroactive metal tungsten (W) for signal amplification, has led to the conduction of a new generation of hybrid nanoarchitecture-based biosensors. The electrical conductivity of WS<sub>2</sub> is mostly upgraded by combining conductive metallic compounds such as gold, platinum, and silver nanoparticles using electrodeposition techniques [139]. The superior obtained performance of such a matrix was successfully performed in medical diagnosis, environmental contamination, and the observation of DNA hybridization, proteins, and enzymes. Giving the example of Shuai et al. [140], which proposed the synthesis of WS<sub>2</sub>-acetylene black (WS<sub>2</sub>-AB) through a simple hydrothermal method based GCE modified AuNPs for the development of electrochemical DNA biosensors (Fig. 12f–j). The fabrication process requires the usage of Au–S bond capture probe and two auxiliary hairpin DNA (Bio-H1 and Bio-H2) for the signal amplification of the hybridization chain reaction (HCR) through the catalytic reaction of hydrogen peroxide + hydroquinone system. The two auxiliary DNA were designed to be opened by the recognition probe and the horseradish peroxidase enzymes for immobilization into the nicked double helices of HCR via

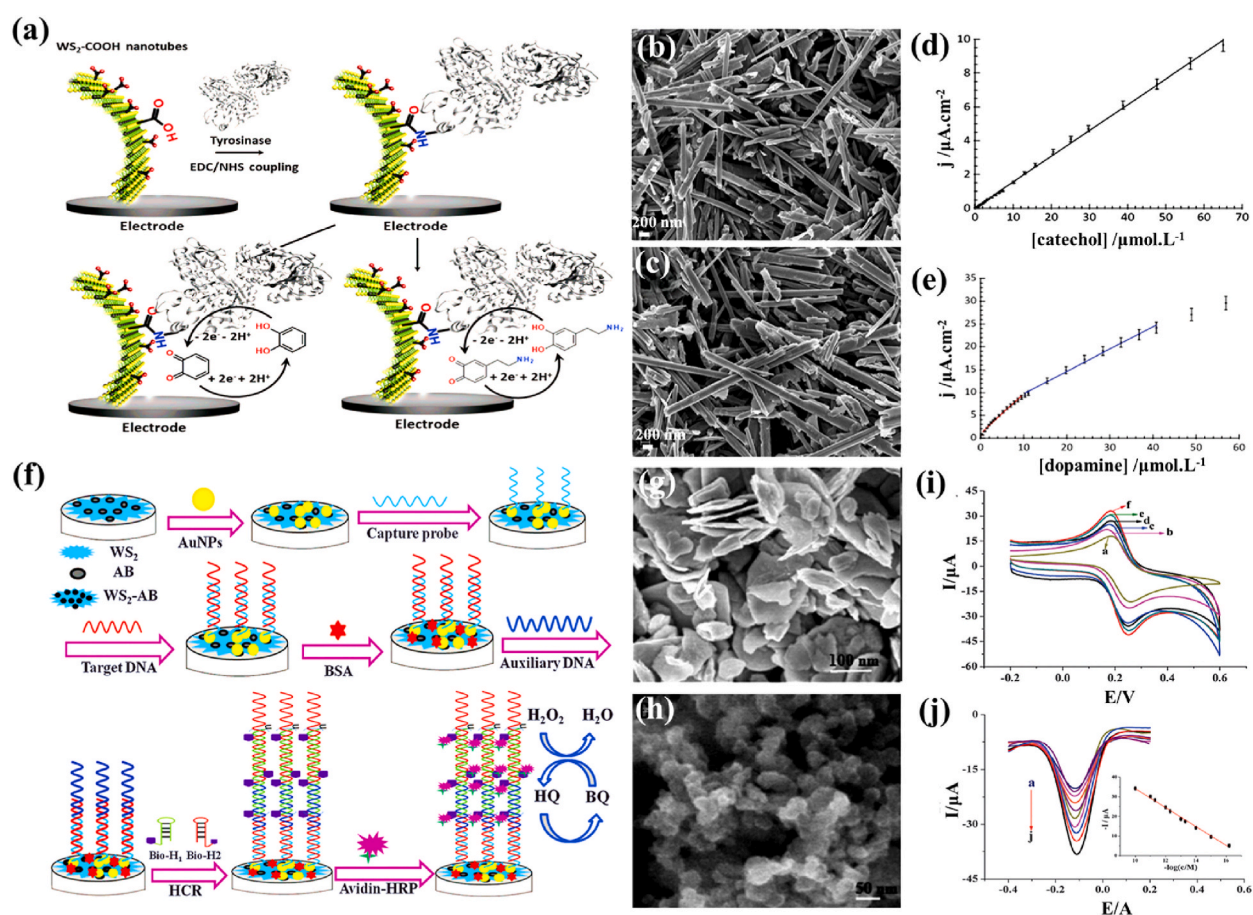


**Fig. 12.** WS<sub>2</sub>-based electrochemical biosensor for catecholamines and DNA detection. (a) Functionalization step of WS<sub>2</sub> modified GCE for the detection of dopamine (bottom right) and catechol (bottom left). SEM image of the synthesized (b) WS<sub>2</sub>-COOH powder and (c) WS<sub>2</sub>-COOH nanotube. Calibration curves of (d) catechol and (e) dopamine. Reproduced with permission from Ref. [23]. Copyright 2020, Royal Society of Chemistry. (f) Sketch of the functionalization steps and working principle of HCR-based DNA biosensor. SEM image of the WS<sub>2</sub> nanosheet (g) before and (h) after acetylene black functionalization. (i) Cyclic Voltammetry of the GCE at different mass ratios of WS<sub>2</sub> and AB from 3: 1 to 1: 1 (b→f). (j) Difference pulse voltammetry of the developed DNA biosensor at various target DNA concentrations (from 0, 1 × 10<sup>-15</sup> to 1.0 × 10<sup>-10</sup> M); Inset is the peak current and target DNA concentration relationship. Reproduced with permission from Ref. [140]. Copyright 2016, Royal Society of Chemistry.

biotin-avidin reaction (Fig. 12f). Under optimized operating conditions, including the WS<sub>2</sub> and AB mass ratios (Fig. 12i), the biosensor displays a linear current response versus logarithmic concentration values of target DNA and a limit of detection down to 0.12 fM. Along the same lines, Huang et al. [141] suggested the dual signal amplification platform based on combining WS<sub>2</sub>/Gr and AuNPs composites. The electron transfer resistance ( $R_{et}$ ) of the glassy carbon electrode (GCE) at each functionalization step was investigated using electrochemical impedance spectroscopy (EIS). Subsequently, the decrease in  $R_{et}$  from 55 to 30  $\Omega$  after WS<sub>2</sub>/Gr coating and its sharp decrease with an almost straight line after the AuNPs incorporation confirmed the good conductivity enhancement following the suggested protocol. This dual signal amplification strategy also showed a strong ability to distinguish the complementary DNA from single/three-base mismatched DNA sequences with good selectivity and sensitivity down to the femtomolar scale.

In addition, the implementation of WS<sub>2</sub>-QD in electrochemical biosensing applications has resulted in a new efficient and straightforward detection approach with improved sensitivity toward targeted biomolecules. Hence, Wang et al. [142] proposed the usage of WS<sub>2</sub>-QD for label-free and sensitive tracing of sulfamethazine (SMZ) residue for food safety and environmental contamination monitoring. The combination of WS<sub>2</sub>-QD with NPs has created a new type of semiconductor used as an electrochemical modifier to uplift the biosensor efficiency in terms of sensitivity, selectivity, and response time. Accordingly, Pourakbari et al. [139] reported the exertion of WS<sub>2</sub>-QDs/AuNPs to develop a new biosensing approach with quick and sensitive electrochemical identification of the c-Met protein. Their method implicated the GCE to be modified with WS<sub>2</sub>-QD, functionalized with AuNPs, and thereafter the c-Met bacteriophage immobilization as a biorecognition element of c-Met protein. The designed protein biosensor displays a low LOD of 1 pg/mL within a linear detection range of 1–1000 pg/mL of c-Met protein.

Over and above, the combination of high conductivity carbon nanotubes (CNTs) and multi-walled carbon nanotubes (MWCNTs) with the catalytic sites of WS<sub>2</sub> dedicated electrochemical sensors applications has led to the new development of robust, quick, non-toxic, and a sensitive platform throughout in vitro toxicity control. Wu et al. [143] suggested the usage of a hybrid composite composed of WS<sub>2</sub> and hydroxylated MWCNTs based on screen-printed carbon electrodes with the benefits of energy efficiency and minimal costs. Modifying the screen-printed carbon electrodes with the obtained hybrid materials considerably enhanced the rate of selectivity and sensitivity behaviors. In this work, cyclic voltammetry was conducted for the electrochemical reaction monitoring of the Grass Carp Kidney (CIK) cell. Whereas the cytotoxic effects of polystyrene nanoplastics (PSNPs), bisphenol AF (BPAF), and 2,4,6-trichlorophenol (2,4,6-TCP) were determined to be compared with the suggested sensor using the course of MTT assay. Besides, Santos et al. [144] combined the CNTs with the WS<sub>2</sub> nanosheet for the development of an isoniazid electrochemical sensor. The synthesized WS<sub>2</sub>/CNTs/GCE sensor exhibits a limit of detection of 0.24  $\mu$ M toward isoniazid and displays recovery values ranging from 96.9 % to 104.5 %, confirming the satisfactory accuracy of the suggested method. Table 3 summarizes the WS<sub>2</sub> nanoarchitecture-based electrochemical biosensors, reporting their measurement techniques, designed structure, the obtained LOD, and dynamic ranges.

#### 4.1.3. Nanopore biosensors

Nanopore sensing technique was first raised by the resistive pulse concept, established from the apparatus of the Coulter counter for sizing and counting particles in electrolytes. Since that, the nanopore system has been extensively studied and developed to attract wide attention not only in protein and DNA sequencing [149–154] but also expanded to cover the field of single molecules sensing [155], small molecules, and bacteria [156], chirality discrimination [157], single-cell matter transport [158], and digital storage domains [159]. The initial development of the nanopores system was made of self-assembling wild proteins, was constructed by inserting the protein pores into a phospholipid bilayer, thus known as biological nanopores [160]. Due to their biocompatibility, stability, and uniformity in structure, protein nanopores provide consistent sensing results with exceptionally low noise levels, high signal-to-noise ratios, and significant repeatability [161]. However, the usage of biological nanopores in scaled fabrication is limited due to their sensitivity to external factors such as small pore size, bias potential, and pH conditions [162]. As an alternative, artificial

**Table 3**

Summary of most WS<sub>2</sub>-nanoarchitecture-based biosensors for various target detection using electrochemical methods.

Electrochemical technique	Structure	Target	Detection limit	Detection range	Ref
EIS	PIIn6COOH/WS <sub>2</sub> /CPE	PIK3CA gene	2.3 $10^{-18}$ mol/L	$10^{-17}$ – $10^{-11}$ mol/L	[138]
EIS	WS <sub>2</sub> /SH-DNA/Au	ATP	1.5 nM	0.1 $\mu$ M–5mM	[137]
Amperometry	Tyrosinase/WS <sub>2</sub> -COOH/GCE	Hg <sup>2+</sup>	0.5 pM	0.1 nM–500 nM	[23]
		Catechol Dopamine	–	0.6–70 $\mu$ mol L <sup>-1</sup> 0.5–40 $\mu$ mol L <sup>-1</sup>	
DPV	HRP/HCR/auxiliary/target/probe/AuNPs/WS <sub>2</sub> -AB/GCE	Target DNA	0.12 fM	0.001–100 pM	[140]
DPV	AuNPs/WS <sub>2</sub> -Gr/GCE	Target DNA	0.0023 pM	0.01–500 pM	[141]
DPV	Aptamer/CQDs-WS <sub>2</sub> /GCE	Sulfamethazine	4.0 pM	10 pM–1.0 $\mu$ M	[142]
SWV	AuNPs/WS <sub>2</sub> QDs/GCE	c-Met protein	1 pg/mL	1–1000 pg/mL	[139]
DPV	WS <sub>2</sub> /CNTs/GCE	isoniazid	0.24 $\mu$ M	10–80 $\mu$ M	[144]
DPV	WS <sub>2</sub> -B QDs/SPE	ferritin	3.8 ng/mL	10–1500 ng/mL	[145]
DPV	HRP/HCR/aDNA/tDNA/cDNA/AuNPs/WS <sub>2</sub> -MWCNT/GCE	hepatitis B virus	2.5 fM	10 fM–0.1 nM	[146]
EIS	bacteria/aptamer/WS <sub>2</sub> /SPE	Listeria	10 CFU/mL	$10^{-10}$ CFU/mL	[147]
DPV	WS <sub>2</sub> NPs-MIP/SPE	Glycated Hemoglobin	0.01 pM	0.01 pM to 100 mM	[148]

nanopores, known as solid-state nanopores (SSN), have gained particular attention due to their stability, durability, and ability to be integrated into other techniques. The SSN sensing process typically involves an insulating membrane with a nanosized aperture sandwiched with a double chamber flow cell (*cis* and *trans*) filled with a buffer solution. While applying a potential difference across the buffer solution generates a stable ionic current flow through the nanopore, the passage of any analyte through the nanopore generates a fluctuation of the ionic current that can be used to identify the analytes based on their size, charge, and other properties. This working principle is illustrated in Fig. 13a, which displays the strand DNA translocation through the SSN and the ionic current fluctuation depending on each base interaction with the nanopore surface.

SSNs were first created using anisotropic silicon nitride using electron-ion milling [162]. Nowadays, multiple other materials have been used to construct biosensor-based SSN, including organic, metallic oxide, silicon-based materials, metal-based materials, hybrid materials, and carbon-based materials [163–168]. Besides the above-listed materials, 2D materials, such as black phosphorene, silicene, graphene, hBN, SnS<sub>2</sub>, MoS<sub>2</sub>, and WS<sub>2</sub>, are becoming a preferred choice for nanopore carriers in DNA analysis due to their high spatial resolution [169–171]. These materials usually display single atom-thickness and possess exceptional semiconductive electronic and optical properties, making them ideal for photoelectric and FETs devices. To achieve practical DNA bases discrimination using 2D materials, durable membranes with adjustable chemical properties for sensitive biomolecule detection are necessary.

Nanopore technology relies on the precise creation and manipulation of the nanoscale orifice, where researchers have made

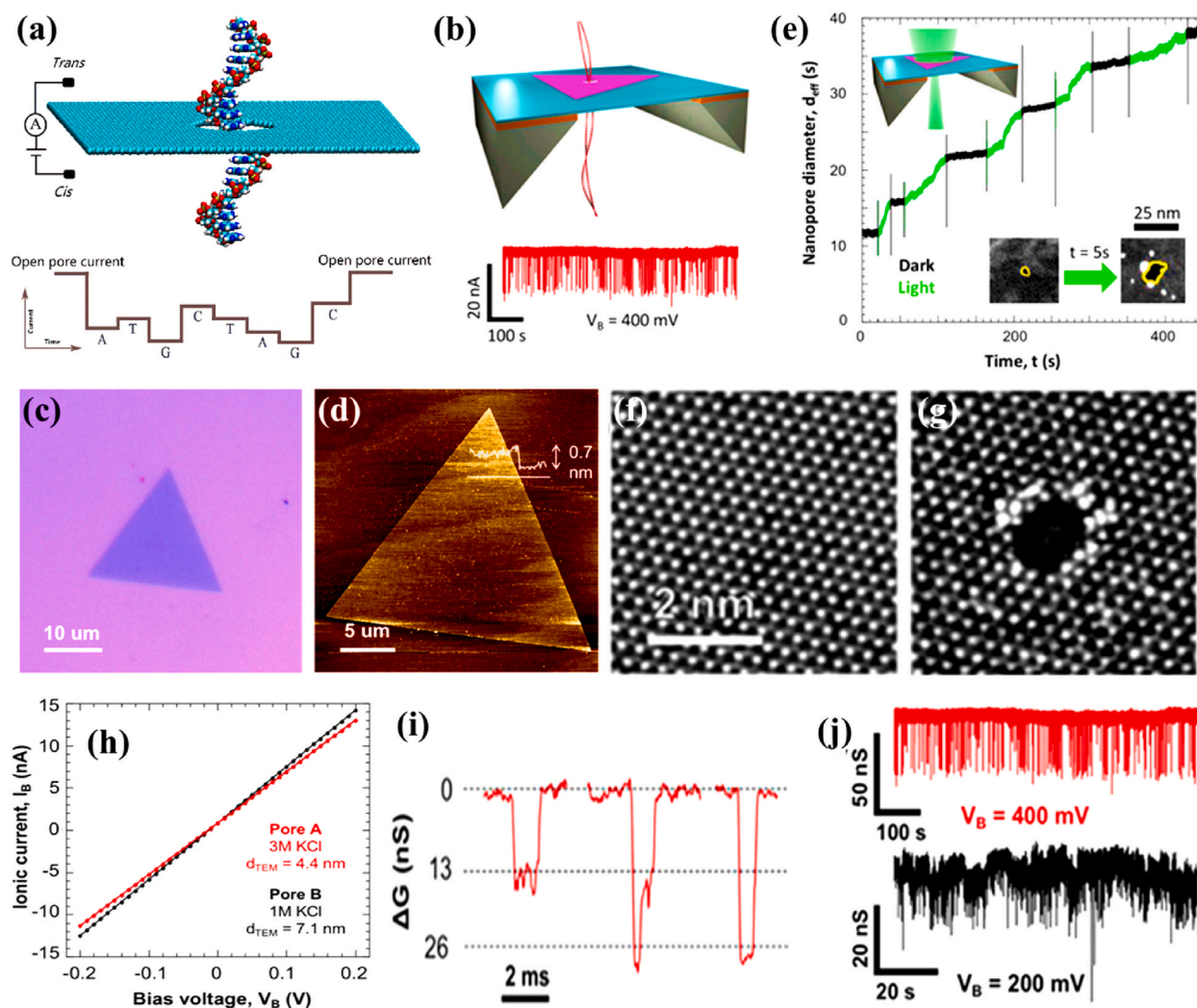


**Fig. 13.** WS<sub>2</sub>-based nanopore biosensor. (a) Figure illustration of DNA sequencing principle through nanopore technology, where the passage of each nucleobase through the pore produces a unique ionic current blockage. Reproduced with permission from Ref. [174]. Copyright 2014, Springer Nature. (b) Schematic illustration of WS<sub>2</sub> nanopore-based DNA translocation. (c) Optical and (d) AFM images of the CVD-grown WS<sub>2</sub> crystal. (e) Nanopore diameter variation versus time under laser exposure. HRSTEM of suspended WS<sub>2</sub> membrane before (f) and after (g) 80 K voltage drilling. (h) Pore diameter and KCl buffer concentration effect on the Current-Voltage measurement of the drilled WS<sub>2</sub> nanopore. (i) DNA translocation events ascribed to unfolded, partially folded, and folded (left to right). (j) Ionic conductance versus time of DNA translocation events at different applied bias voltage sweep. Reproduced with permission from Ref. [173]. Copyright 2017, American Chemical Society.

significant strides in understanding how to generate, shape, and stabilize these orifices. Ryu et al. [172] aimed to understand the impact of temperature on the defect dynamics of TMDCs. By altering the heating temperature from ambient to 1000 °C, the authors followed the thermal activation effect on the movement of S vacancies and the formation of nanopores. Therefore, the temperature of 500 °C was optimal for promoting S vacancy diffusion and increasing defect density, leading to stable single-layered nanopores (SLNPs) in WS<sub>2</sub>. These nanopores are formed through the reconstruction of atoms surrounding a solitary vacancy site of W, and they remain stable upon subsequent irradiation. Furthermore, it was noted that Mo-based TMDCs like MoS<sub>2</sub> did not exhibit SLNPs. This implies that WS<sub>2</sub> holds promise in developing sub-nanometer pores based on 2D materials. In another work, Danda et al. [173] demonstrated the use of WS<sub>2</sub> nanopore-based light-responsive biosensors for DNA Translocation (Fig. 13b–j). The monolayer structure of the CVD-grown WS<sub>2</sub> was well characterized using AFM, Raman spectroscopy, and TEM. PL spectra was used to follow the damage of the suspended WS<sub>2</sub> supported on a silicon substrate during the nanopore drilling step through a focused electron beam. In this work, authors also reveal that by utilizing focused 532 nm laser illumination in a solution, WS<sub>2</sub> nanopores can be methodically enlarged at an effective rate of around ~0.2–0.4 nm/s, which is not possible using the conventional SiNx nanopore. Therefore, following this strategy, authors provided an atomic level precision in nanopore size control using short light pulses.

#### 4.1.4. Field-effect transistor biosensors

To date, there are several detection methods utilized in biosensors, including high-performance liquid chromatography (HPLC) [175], surface plasmon resonance (SPR) [176], fluorescence-based optical detection [177], quartz crystal microbalance (QCM) [178], and electrochemical impedance spectroscopy [179–181]. Despite their advanced development, these techniques are sophisticated,

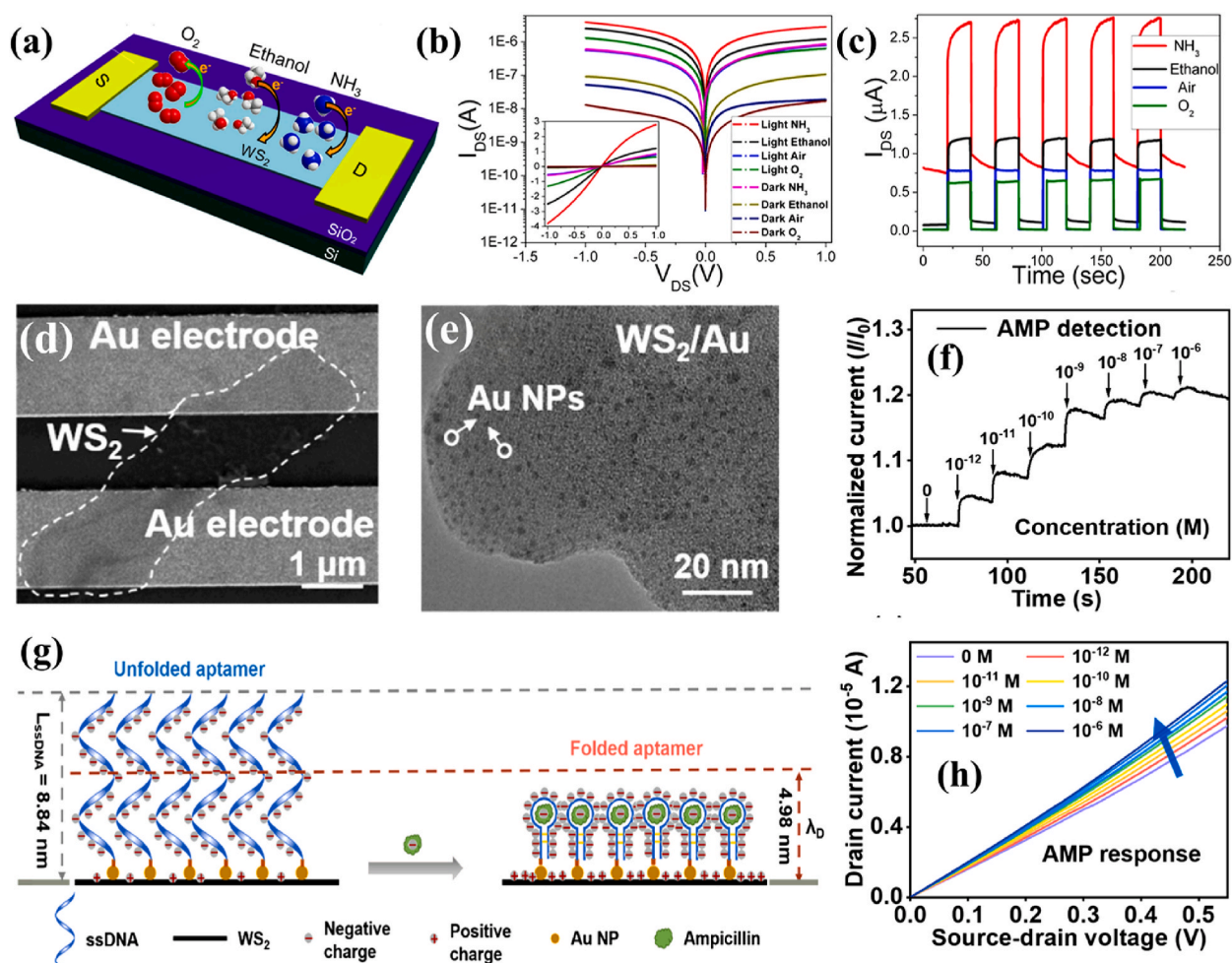


**Fig. 14.** a) Schematic of the transfer process between WS<sub>2</sub> nanoflakes and the adsorbed gas molecules onto WS<sub>2</sub> microchannel based FET. b) In dark and light photocurrent response at various gas entities. c) photocurrent response versus time under multiple gas atmospheres. Adapted from Ref. [198]. Copyright 2014, Springer Nature. d) SEM image of the bridged WS<sub>2</sub> film onto interdigitated gold electrodes. e) TEM image of the WS<sub>2</sub>/Au composite. f) Time response of WS<sub>2</sub> FET biosensor at different AMP concentrations. g) Structure variation of the AMP aptamer before and after the presence of AMP. h) Output characteristics of the WS<sub>2</sub> FET biosensor at various AMP concentrations (0–10<sup>-6</sup> M). Adapted from Ref. [199]. Copyright 2023, Elsevier B.V. (For interpretation of the references to color in this figure legend, the reader is referred to the Web version of this article.)

costly, and require consistently trained operators and tedious sample preparation. By contrast, FET-based biosensing brings various benefits, including high sensitivity, low limit of detection, rapid detection time, low cost, miniaturization, and attractiveness to label-free detection strategy [1,21,86,182,183]. Additionally, the rapid advancements in solid-state technologies have paved the way for the emergence of FET-based biosensors as a promising technology for applications in various fields requiring fast response time with high sensitivity. Furthermore, the integration of CMOS manufacturing techniques has facilitated their miniaturization, thus giving it a competitive edge over other bio-sensing mechanisms.

FET presents the main component of today's integrated circuits. By continuously minimizing its characteristic length (channel size) following Moore's law, new materials and new structures were explored. 2D semiconductor materials with their ultrathin thickness, moderate bandgap, CMOS compatibility, and exceptional high-carrier mobility are intensively studied [184,185]. In this regard, 2D  $\text{WS}_2$  is anticipated to be a promising candidate for high-performance transistors [66–68], being advantageous of the large band gap, where their transistor displays a relatively large ON/OFF current ratio of ( $>10^5$ ) [37,186–189], with the prediction to bear the high electron mobility as the rest of TMDCs. Furthermore, compared to  $\text{MoS}_2$ ,  $\text{WS}_2$  exhibits greater thermal stability [190] and higher intrinsic electric conductivity [191]. However,  $\text{MoS}_2$ -based FETs have gained significant interest for their potential in detecting a variety of biomolecules, such as proteins [192], heavy metals [193], antibiotics [194], DNA [195], and disease biomarkers [196]. Nevertheless, the detection of such biomolecules using  $\text{WS}_2$  FET has not been fully explored. Therefore, below, we come up with an exclusive overview of the existing research works related to  $\text{WS}_2$  FET as a gas sensing and biosensing platform.

In addition to the above-mentioned advantages list, TMDCs possess low operating temperatures over conventional metal oxide, making it an attractive platform for chemical gas sensor-based field effect transistors. Accordingly, Järvinen et al. [197] developed a  $\text{WS}_2$  FET-based gas sensing for the detection of  $\text{NH}_3$  analytes in the air at 30 °C. The  $\text{WS}_2$  nanochannel was grown using the thermal sulfurization of sputter deposition metal films. The unique  $\text{NH}_3$  gas sensor displays a particularly high sensitivity of  $0.10 \pm 0.02 \text{ ppm}^{-1}$  and selectivity against  $\text{H}_2$ ,  $\text{H}_2\text{S}$ , and  $\text{CO}$  analytes. Similarly, Huo et al. [198] elaborated a  $\text{WS}_2$  multilayer FET biosensor for detecting  $\text{NH}_3$  and ethanol (Fig. 14a–c). Both target analytes were found to be electron donors, enhancing the photo-responsivity ( $R_L$ ) and external quantum efficiency (EQE) response to 5.7 A/W and 1118 %, respectively. This work demonstrates the  $\text{WS}_2$  nanoflakes' integrity as a significant FET channel for highly sensitive gas sensors-based field-effect transistor applications.

Another worth mentioning research work based on  $\text{WS}_2$  FET is that of Wei et al. [199], in which they suggested a specific, fast, and ultrasensitive detection of ampicillin (AMP) within a wide linear range of concentration ranging from  $10^{-12}$  to  $10^{-6}$  M as depicted in Fig. 14d–h. The developed biosensor was based on spin coating deposition of thin film tungsten disulfide as a sensing channel and ssDNA anchored to gold nanoparticles via thiolate terminated bond as a detection probe. Following this strategy, the suggested AMP biosensor displayed an LOD down to 0.556 pM and a fast response to AMP within 5 s. A real sample measurement was carried out in the water, proving its potential application in practical AMP detection. Debye screening effect is an important indicator of the charge

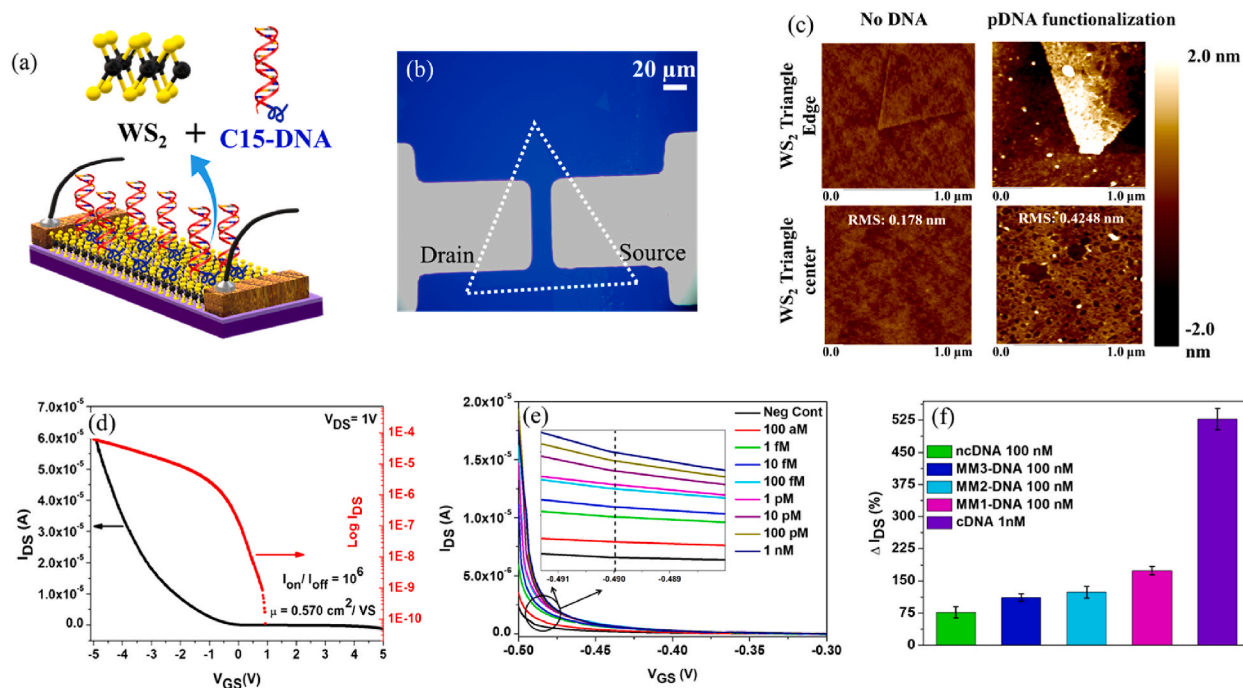


**Fig. 15.** a) Schematic illustration and b) optical image of  $\text{WS}_2$  FET. c) AFM topography of the CVD-grown  $\text{WS}_2$  before and after DNA probe incubation. d) Electrical characteristics of the developed  $\text{WS}_2$  FET. e) Drain-source versus gate potential response under different complementary DNA concentrations. f) Selectivity test of the  $\text{WS}_2$  FET with the existence of non-complementary and various mismatched DNA sequences. Reproduced with permission from Ref. [21]. Copyright 2022, American Chemical Society.

transfer, which implies the electrical double layer (EDL) existence and one of the main factors limiting the biosensor's efficiency, especially for a purely electronic device like FETs [86]. Physically, the screening effect depends on the Debye length ( $\lambda_D$ ), which defines the distance separating the charged ions in the solution and the sensing surface; within it, the charges can still have an electrical effect on the sensing surface. To overcome such a limit, Wei et al. also assumed that the AMP aptamer (ssDNA) is supposed to be folded into a specific stable loop structure under ampicillin. Such folded ssDNA structure led to a strong signal in the biosensor through the electrostatic effect, thus overcoming the Debye length by folding.

Besides the covalent approach, we followed the non-covalent approach to anchor the probe molecules to WS<sub>2</sub> FET channel for DNA hybridization detection via poly-cytosine (poly-C) DNA (Fig. 15a–f) [21]. To synthesize the WS<sub>2</sub> monolayer with large-area and high-quality, NaCl-assisted atmospheric pressure of CVD growth method was adapted, leading to a high field-effect mobility of  $\sim 0.57 \text{ cm}^2\text{V}^{-1}\text{s}^{-1}$  and an ON/OFF current ratio of  $\sim 10^6$ . At the same time, the successful anchoring of the DNA probe onto the WS<sub>2</sub> sensing channel was confirmed via AFM by following the surface roughness variation from 0.178 to 0.424 nm before and after DNA probe incubation, respectively. In this work, the first block of the absorbed DNA probe was intentionally designed with successive cytosine DNA (C15 DNA) for strongly anchoring to the WS<sub>2</sub>. The second block, however, remains lifted at the surface for target DNA recognition. The resulting WS<sub>2</sub>-based FET biosensor demonstrated a significantly improved response to complementary DNA within a concentration ranging from  $10^{-16}$  to  $10^{-9}$  M, leading to a limit of detection (LOD) of 3 aM. Additionally, it can differentiate between the target DNA, non-complementary, and mismatched DNA sequences, thus confirming its high selectivity and ultra-sensitivity for complementary DNA detection. The high sensitivity and selectivity were referred to the fully saturated WS<sub>2</sub> sensing channel with poly-C DNA, which showed a high affinity to most 2D materials like GO, MoS<sub>2</sub>, Au, graphene, ZnO, and WS<sub>2</sub> [200,201]. Such a high affinity was attributed to the fact that inorganic material usually exists reflecting a periodic structure equipollent to the length of DNA

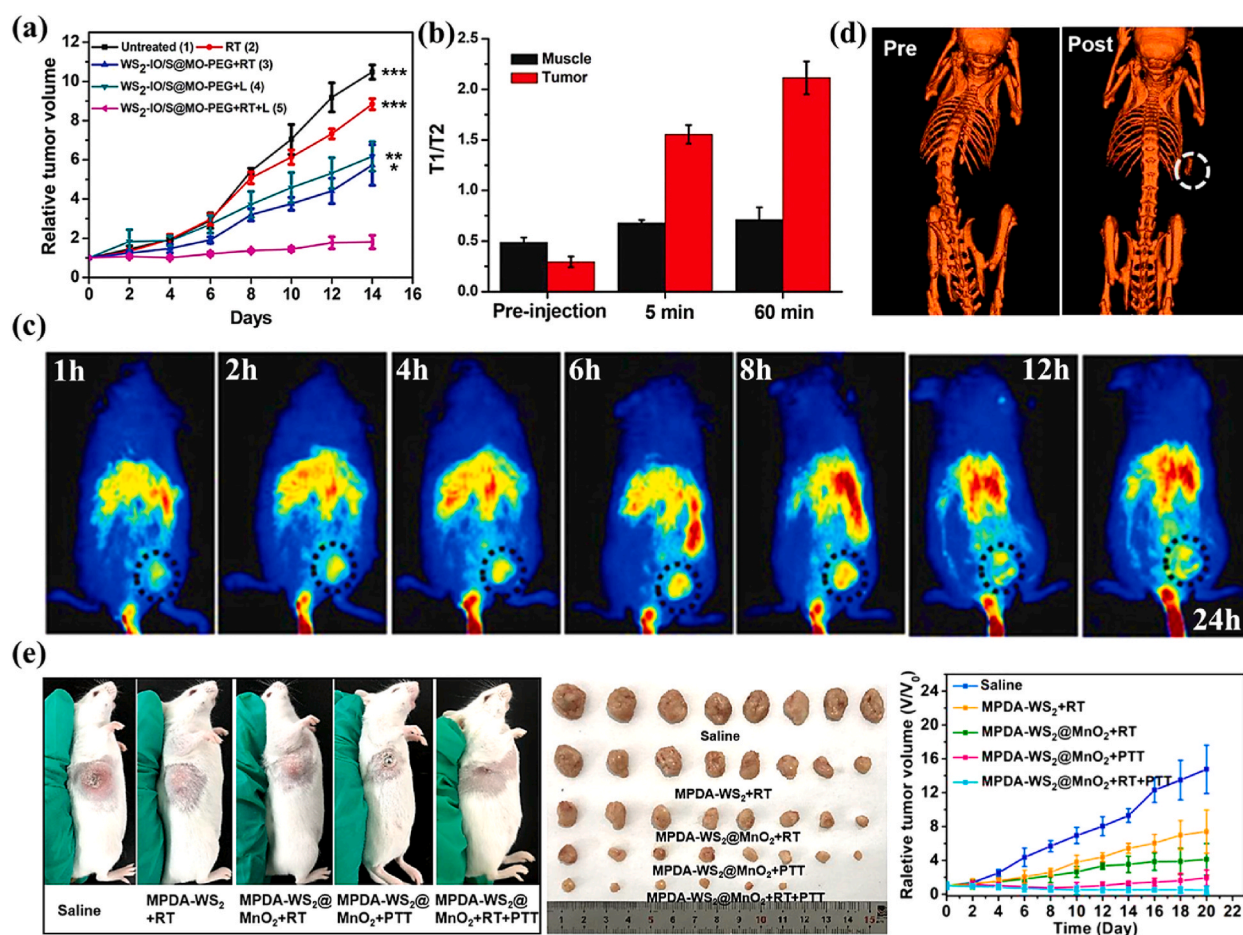


**Fig. 16.** WS<sub>2</sub> nanoarchitecture-based tumor therapy. (a) Relative tumor volume versus time of multiple mice following different treatments using WS<sub>2</sub>-IO/S@MO-PEG. (b) In muscle and tumor T1/T2 signals analysis versus time before and after WS<sub>2</sub>-IO/S@MO-PEG injection. (c) In vivo fluorescence image analysis at various time points after WS<sub>2</sub>-IO/S@MO-PEG injection of mice. Reproduced with permission from Ref. [208]. Copyright 2017, Wiley-VCH. (d) Computed tomography imaging of tumor before and after MPDA-WS<sub>2</sub>@MnO<sub>2</sub> NPs injection of mice, white dotted circles corresponding to the tumor region. (e) Therapeutic effects of tumor-bearing mice on the 20th day of various components injection and therapy treatment; Tumors photograph; and relative tumor volume curves of different mice groups after different treatments. Reproduced with permission from Ref. [209]. Copyright 2019, Elsevier B.V.

nucleotide (0.34 nm), displaying a good and simple repeating sequence for the DNA to be adhered to Ref. [202]. Therefore, adopting this DNA anchoring theory, the developed FET biosensor displayed an ultrasensitive detection of DNA following a simple detection method, chemical-free treatment of the sensing interface, and time-gaining, along with a lower cost.

## 4.2. Nanomedicine applications of WS<sub>2</sub>

### 4.2.1. Oncotherapy

Due to its biological stability, inherent therapeutic property, near-infrared light absorption, and responsiveness to external stimuli characteristics, WS<sub>2</sub> has been widely performed in various oncotherapy, where various nanotechnology platforms have been developed [25]. Moreover, tungsten disulfide nanosheet exhibited a lower cytotoxicity degree than MoS<sub>2</sub> and WSe<sub>2</sub> nanosheets [203], making it an auspicious candidate for tumor cell elimination-based photothermal treatment [204].

Nandi et al. [205] demonstrated the bifunctional activity of WS<sub>2</sub> nanorods and carbon dots (C-dots) mixture in multicolor cell imaging and targeted photothermal therapy (PTT). Such bifunctionality was mainly referred to as the combination of the photothermal activity of WS<sub>2</sub> and the photoluminescence of C-dots. Meanwhile, the modification of the WS<sub>2</sub> nanosheet with the paramagnetic Ga<sup>3+</sup>, PEG, and short peptide-dedicated specific tumor marker was promising for the treatment and detection of HCC-expressing GPC3. The developed WS<sub>2</sub>-Ga<sup>3+</sup>-peptide-PEG membrane for PTT displays the ability to eliminate the tumor within 24 h and to identify small tumor masses via Gd<sup>3+</sup>-mediated magnetic resonance imaging (MRI) [206].

In contrast, due to the weak penetration of near-infrared power (NIR), the effectiveness of PTT in deep-seated tumor treatment is limited. While using radiotherapy (RT), the ionizing radiation has no depth limitation and can reach deep tumors, but less effective on account of the low oxygen levels in solid tumors. Therefore, combining PTT and RT can overcome these limitations and provide a more powerful anti-tumor effect. However, the key challenge lies in developing a biocompatible nano-platform that simultaneously delivers

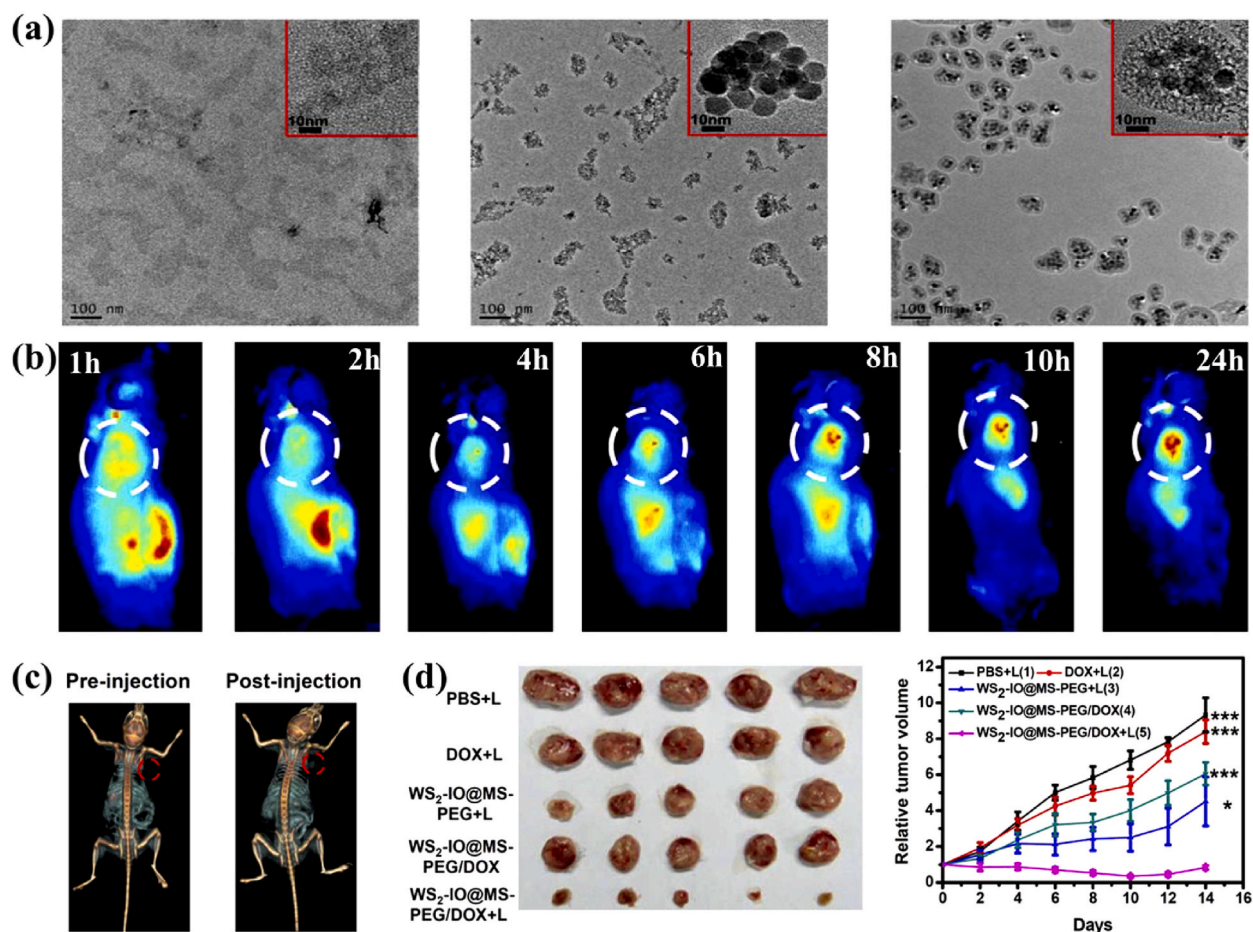


**Fig. 17.** WS<sub>2</sub>-IO@MS-PEG based tumor therapy. (a) TEM images of WS<sub>2</sub>, WS<sub>2</sub>-IO, and WS<sub>2</sub>-IO@MS-PEG, respectively from left to right. (b) In vivo fluorescence image analysis of 4T1 tumor at various time points after mice injection with Cy5.5 labeled WS<sub>2</sub>-IO@MS-PEG. White dotted circles correspond to the tumor region. (c) Computed tomography imaging of tumor before and after 24 h of WS<sub>2</sub>-IO@MS-PEG injection. (d) 4T1 tumors photograph after 14 days of various treatments in different mice groups; and tumor growth profile of different mice groups after various treatments. Reproduced with permission from Ref. [218]. Copyright 2015, Elsevier B.V.

photothermal sensitizers and radiosensitizers. Accordingly, WS<sub>2</sub> dots were found to combine the good PTT/RT synergy with precise tumor targeting and the CT/PA imaging capability at its bare state without further modification [207]. Additionally, Yang et al. [208] coated the WS<sub>2</sub> nanoflakes with iron oxide nanoparticles (IONPs), silica, manganese dioxide (MnO<sub>2</sub>), and polyethylene glycol (PEG) for pH-responsive MRI (Fig. 16a–c). In this work, the developed WS<sub>2</sub>-IO/S@MO-PEG is basically used for a synergistic combination of tumor therapy based on the mixture of WS<sub>2</sub> absorbance ability of X-ray and near-infrared for RT and PTT enhancement, as well as MnO<sub>2</sub> capability to break down tumor-generated hydrogen peroxide and alleviate tumor hypoxia to defeat radiotherapy resistance caused by low oxygen levels. Such a combination with WS<sub>2</sub>-IO/S@MO-PEG issues a remarkable impact on tumor destruction, suggesting a potential nanocomposite for simultaneously performing imaging and treatment in the tumor microenvironment to improve precision cancer therapy. Similarly, the embedding of WS<sub>2</sub> QDs mesoporous polydopamine (MPDA) followed by MnO<sub>2</sub> integration led to multifunctional nanoplatforms with enhanced tumor oxygenation and improved RT efficacy (Fig. 16d and e) [209]. Not to mention that the incorporation of the radioisotope Rhenium-188 (188Re) into PEG-modified WS<sub>2</sub> nanoflakes significantly enhanced the effectiveness of RT and allowed greater absorption of 188Re ionizing radiation by W atoms [210].

On the other hand, combining chemotherapy (CT) and PTT has shown great potential in effectively minimizing the therapeutic doses of the drug, which effectively reduces the tumor's resistance to the drug [211–217]. However, to achieve optimal results using photothermal-chemotherapy (PCT), the used nanoplatform must combine excellent target abilities with good biocompatibility, high photothermal conversion efficiency, and stability. To do so, Yang et al. [218] used WS<sub>2</sub>-IO@MS-PEG to effectively target the tumors and enable imaging-guided PCT through various techniques like fluorescence, MRI, and X-ray computed tomography (Fig. 17a–d). The suggested nanocomposite possesses various unique properties, such as high absorption X-rays, near-infrared light, and strong superparamagnetic. Additionally, the authors demonstrated the mesoporous silica shell's ability to be filled with the chemotherapy drug doxorubicin (DOX), which is further released within cells via NIR-induced photothermal heating for increased cancer cell destruction. Finally, the combination of PTT, photodynamic therapy (PDT), and RT was also performed via WS<sub>2</sub>@PANI/Ce<sub>6</sub>-HA nanoplatform, in which using single or double treatment did not successfully inhibit the growth and prevent any recurrence of the tumor as using triple treatment [204]. Table 4 summarizes previous works reporting the modifier and the associated therapy method of WS<sub>2</sub> nanoarchitecture-based tumor therapy.

#### 4.2.2. Drug delivery and nanocarriers

Conventional drug delivery methods, such as oral and injection, require high doses of medication to produce a therapeutic effect, which is often followed by a side effect in some clinical cases. However, recent advances in nanomedicine have led to the development of stimuli-responsive drug delivery systems that possess a controllable drug dosage possibility through magnetic fields, pH, light, ultrasound, or electrical stimulation.

Tungsten disulfide, with its excellent biocompatibility and high drug-loading capacity, holds the potential to improve therapeutic outcomes, reduce side effects, and enable combination therapies [207]. For example, Li et al. [221] investigated the WS<sub>2</sub>/Au-lipid

**Table 4**  
WS<sub>2</sub> nanoarchitecture-based Tumor therapy.

Method	Modifier	Remark	Therapy	Ref
Monotherapy	C-dots	Photoluminescence imaging	PTT	[205]
	PEI <sup>a</sup>	–	PTT	[219]
	Ga <sup>3+</sup>	Target	PTT	[206]
	PEG	Magnetic resonance imaging		
	Peptide	Photoluminescence imaging Photoacoustic imaging		
Combined therapy	PANI <sup>a</sup>	–	PDT	[204]
	HA <sup>a</sup>		PTT	
	Ce6 <sup>a</sup>		RT	
	PEG	Photoluminescence imaging	PTT-CT	[218]
	Silica	Magnetic resonance imaging		
	Fe <sub>3</sub> O <sub>4</sub>	Computed tomography imaging		
	PEG	Magnetic resonance imaging	PTT-RT	[208]
	Fe <sub>3</sub> O <sub>4</sub>			
	Silica			
	MnO <sub>2</sub>			
	188Re	–	PTT-RT	[210]
	PEG			
	MPDA <sup>a</sup>	Computed tomography imaging Photoacoustic imaging	PTT-RT	[209]
	MnO <sub>2</sub>	Magnetic resonance imaging		
–	Computed tomography imaging Photoacoustic imaging	PTT-RT	[207]	
PEG	Computed tomography imaging	PTT-RT	[220]	
Gd <sup>3+</sup>	Photoacoustic imaging Magnetic resonance imaging			

<sup>a</sup> PEI: Poly (ethylene imine), \*PANI: Polyaniline, \*HA: Targeting molecule, \*Ce6: Photosensitizer, \*MPDA: Mesoporous PDA, \*PVP: Polyvinylpyrrolidone.

loading capacity of the anti-cancer drug DOX for photo-chemotherapy of tumors. Firstly, the suggested nanoarchitecture was based on lipid-modified single-layered WS<sub>2</sub> doped AuNPs, aiming to enhance the biocompatibility, hydrophilicity, and stability properties (Fig. 18a). The WS<sub>2</sub>/Au-lipid complex displayed a reliable drug carrier through a drug release pattern as a response of both pH and NIR light variations, making it advantages for combined phototherapy and chemotherapy treatments. Additionally, the WS<sub>2</sub>/Au-lipid-DOX + NIR structure was found to be the most effective tumor suppression without significant weight loss in the mice, leading to a

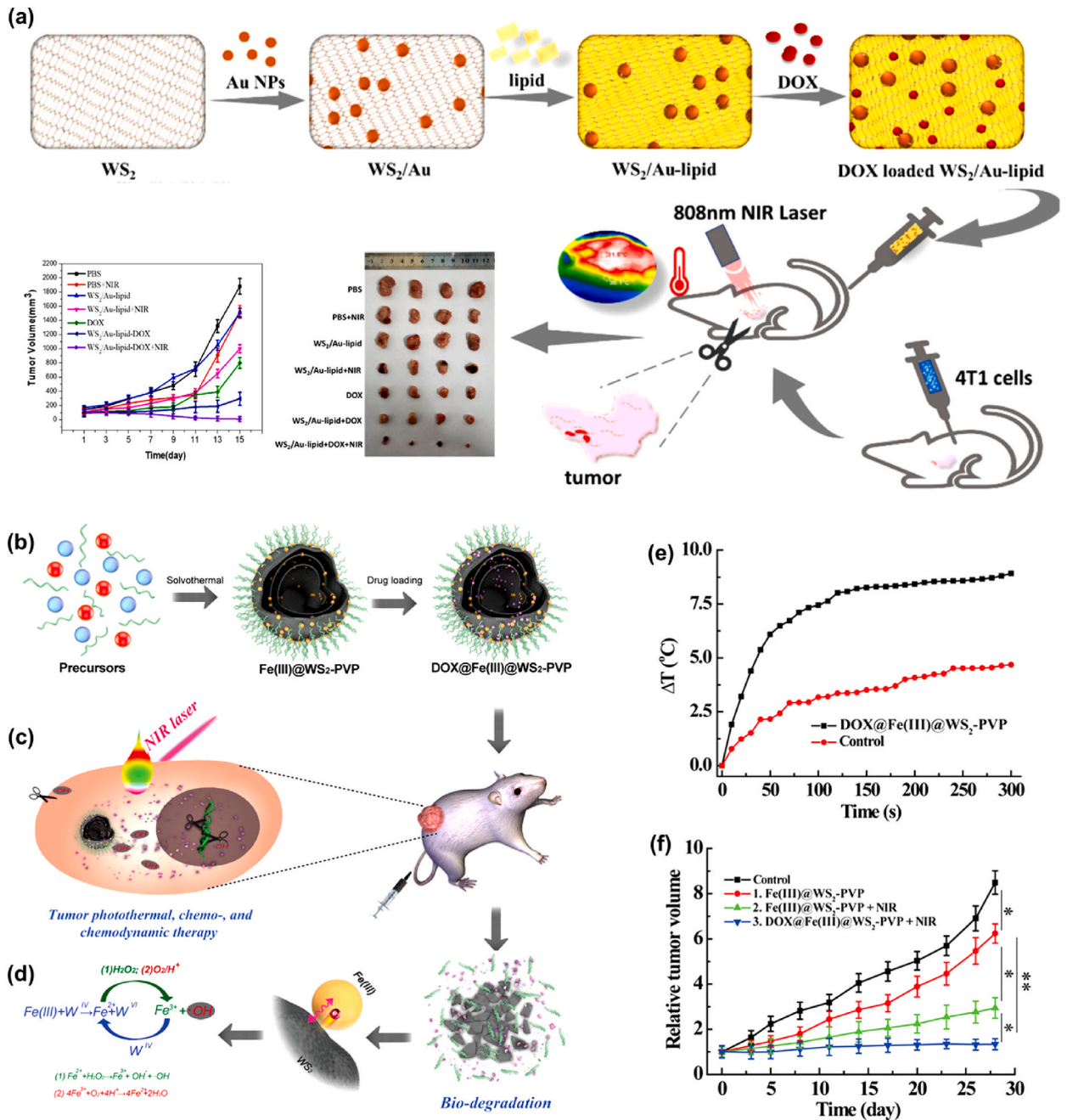
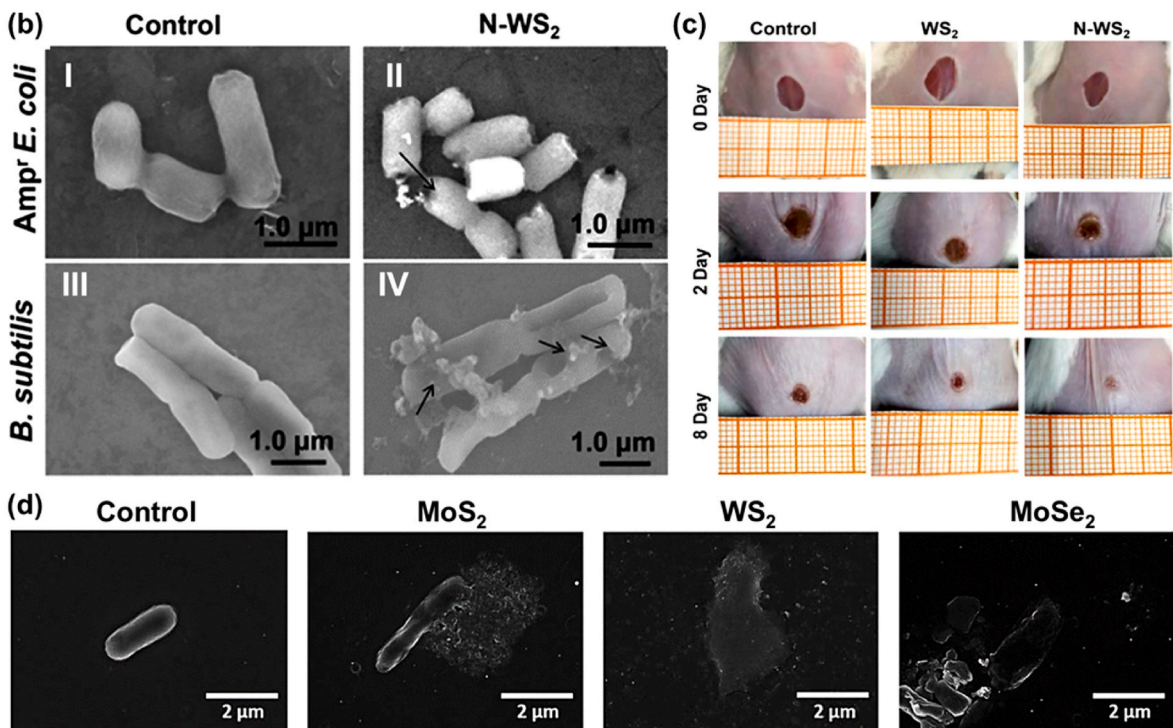
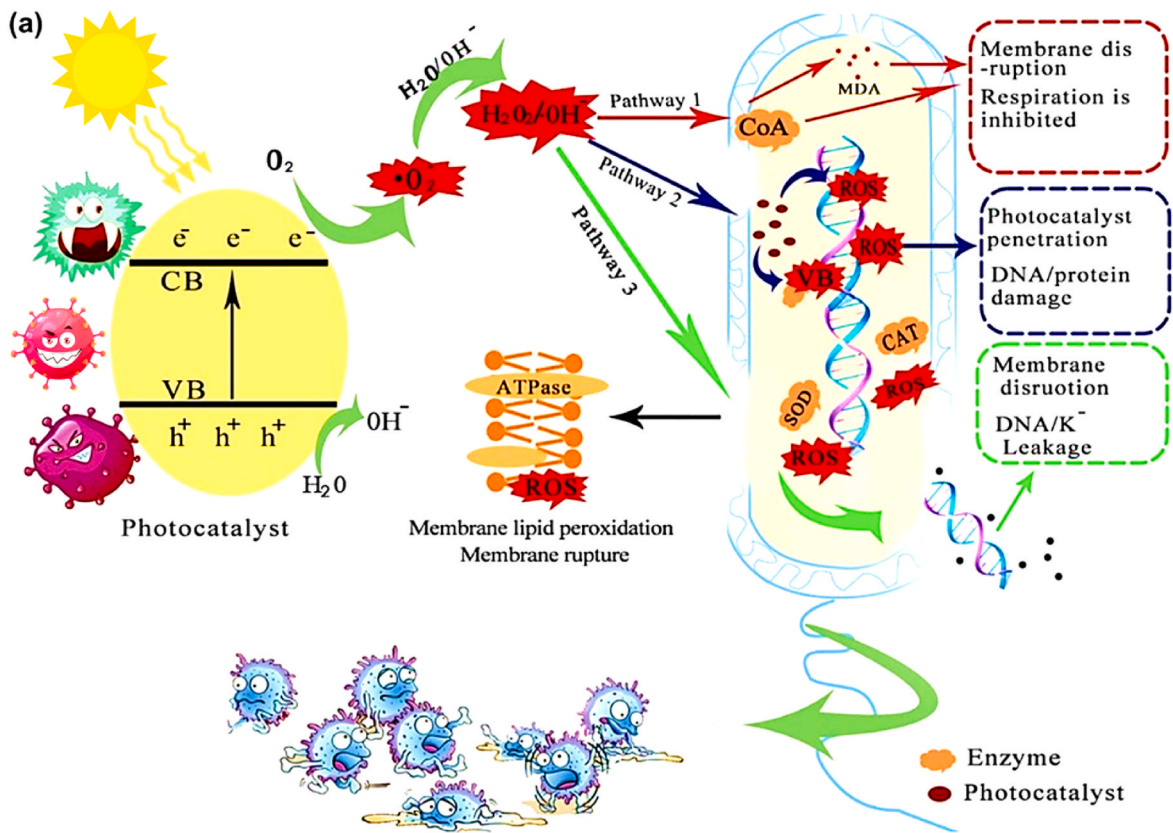


**Fig. 18.** Tungsten disulfide (WS<sub>2</sub>)-based drug delivery and nanocarrier applications. a) Schematic illustration of WS<sub>2</sub>/Au-lipid synthesis and photo-chemotherapy combination for anti-breast cancer cells (4T1) application. Reproduced with permission from Ref. [221]. Copyright 2022, Elsevier B. V. b) Schematic description of the solvothermal synthesis and drug loading phases of Fe(III)@WS<sub>2</sub>-PVP nanocapsules. c) Tumor photothermal, chemo-and chemodynamic therapy. d) The repeated redox reaction and H<sub>2</sub>O<sub>2</sub> and H<sup>+</sup>-based biodegradation enhancement. Green lines, pink and yellow circles depict the PVP, DOX, and Fe(III), respectively. e) Tumor heating versus time curves of mice under NIR laser irradiation. f) Relative HT29 tumor growth of mice after various treatments. Reproduced with permission from Ref. [224]. Copyright 2019, Wiley-VCH. (For interpretation of the references to color in this figure legend, the reader is referred to the Web version of this article.)



(caption on next page)

**Fig. 19.** a) Schematic of photocatalytic antibacterial mechanism. Reproduced with permission from Ref. [229]. Copyright 2020, Royal Society of Chemistry. b) FE-SEM of *AmprE. Coli* and *B. subtilis* treated with PBS (I and III) and (II and IV) defect-rich N-WS<sub>2</sub> nanosheets. c) Photographs of *AmprE. coli* infected mice treated with WS<sub>2</sub>, and defect-rich N-WS<sub>2</sub> nanosheets within 8 days. Reproduced with permission from Ref. [231]. Copyright 2020, Royal Society of Chemistry. d) SEM images of *E. Coli* cells in the control and incubation stages with MoS<sub>2</sub>, WS<sub>2</sub>, and WSe<sub>2</sub> nanomaterials. Reproduced with permission from Ref. [233]. Copyright 2019, IOP Publishing.

successful eradication of the tumor after only a 15-day treatment period. The remarkable response was primarily attributed to the lipid modification, which improves the hydrophilicity of WS<sub>2</sub>/Au for tumor accumulation enhancement. Secondly, the employed photo-thermal therapy that destroys tumors and facilitates drug release within the tumor tissues, yielding highly effective results. Similarly, Sobhani et al. [222] investigated the near-infrared (NIR) irritant in Pioglitazone (PG) release from thermosensitive nanocarrier made of dendrimers grafted Poly (N-Vinylcaprolactam) modified WS<sub>2</sub> nanosheets. The manufactured structures underwent testing simulation of human blood for diabetes treatment, releasing only 18 % of the total drug at 37 °C and 98 % at 50 °C within 6 h in the absence of IR irradiation. In contrast, the application of near-infrared (NIR) laser light heat on the modified WS<sub>2</sub> nanocarrier induced the shrinkage of the polymer and the total release of the PG drug within 15 min.

Another notable survey is that of Hsiao et al. [223], in which an electrically responsive model for 5-fluorouracil (5-FU) as anti-cancer drug loading was developed. To do so, the exfoliated WS<sub>2</sub> was modified with thiol-terminated ligands, such as thioglycolic acid (TGA), 2-ethanethiol (2 E T), and dimercaptosuccinic acid (MSA), then coated with the electrically conductive polypyrrole (PPy). The TGA-WS<sub>2</sub>-PPy structure showed higher drug release (90 %) than MSA and 2 E T, while the TGA-WS<sub>2</sub>-PPy-FU system showed no significant cytotoxicity to HaCaT cells without electrical stimulation. Raman mapping was conducted to follow the carrier's penetration into the skin, confirming a deeper penetration of the drug under electrical stimulation and the death of the HaCaT cells. Lastly, to illustrate WS<sub>2</sub> efficiency in drug delivery system further, consider the following study of Wu et al. [224], in which authors suggested a one-pot synthesis method to create biocompatible (Fe(III)@WS<sub>2</sub>-PVP) nanocapsules with improved biodegradability and high doxorubicin (DOX) loading capacity. The nanocapsules were exposed to a redox reaction between Fe(III) and WS<sub>2</sub>, creating Fe<sup>2+</sup> and WO<sub>4</sub><sup>2-</sup> for biodegradation enhancement and the release of DOX. The presence of H<sub>2</sub>O<sub>2</sub> and mild acidity in the tumor microenvironment further accelerate such a process, where the generated Fe<sup>2+</sup> leads to a fast Fenton reaction with H<sub>2</sub>O<sub>2</sub> in the tumor cells, producing toxic hydroxyl radicals for nanocatalytic tumor therapy. Simultaneously, the nanocapsules possess high photothermal transforming ability, combining endogenous redox reaction and exogenous tumor microenvironment-augmented photothermal therapy, chemotherapy, and nanocatalytic therapy (Fig. 18b–f).

#### 4.2.3. Antibacterial applications

The special traits of tungsten disulfide offer a new solution for tackling bacterial infections [225]. Compared to traditional inorganic nanomaterials like Ag, Zn, and Ti, WS<sub>2</sub> displays well-dispersed S3p orbitals and a larger anion radius of the S atoms, leading to a narrower band gap energy (~ 1.8 eV) with a lower level of toxicity, and a higher photothermal conversion rate [226]. Such pros make the WS<sub>2</sub> an effective candidate for antibacterial/antifouling coatings on medical equipment, water filtration, food packaging, and implants. Additionally, WS<sub>2</sub>-based antibacterial is also cost-effective and has a lower risk of bacterial resistance compared to traditional antibiotics or antimicrobial peptides. Thus, uplifting the tungsten disulfide to get a promising direction in addressing the growing issue of drug-resistant bacteria [227]. To date, multiple antibacterial mechanisms have been identified, including piezocatalytic breakdown, antibacterial nanozymes, photocatalytic antibacterial activity, harm to the membrane, photothermal impact, and the release of polysulfane [228]. Among them, photocatalytic and membrane damage mechanisms are frequently mentioned and performed.

The photocatalysis mechanism implicates generating reactive oxygen species (ROS) to disrupt cell structure. Under light irradiation with an energy higher than the band gap, causes the activation of photocatalyst and consequently the creation of photoinduced electron-hole pairs. Consequently, these pairs lead to the formation of various ROS, such as superoxide (O<sub>2</sub>•<sup>-</sup>), hydrogen peroxide (H<sub>2</sub>O<sub>2</sub>), singlet oxygen (<sup>1</sup>O<sub>2</sub>), or hydroxyl radicals (•OH), ensuing the peroxidation of lipid membranes, inactivation of proteins, and ultimately, the germs death (Fig. 19a). The membrane damage mechanism is based on the initiation of electron transfer from the bacterium's membrane to the nanomaterial when it comes into direct contact with the cell membrane. This interaction disrupts the bacterium's respiration and creates oxidative stress and energy deprivation, resulting in a loss of membrane stability and inactivation of the bacterium [229]. For instance, Liu et al. [230] investigated the potential of WS<sub>2</sub> nanosheet as against *Staphylococcus aureus* (*S. aureus*) and *Escherichia coli* (*E. coli*). The WS<sub>2</sub> samples showed antibacterial activity, slowing bacterial growth by fully covering the bacterium dependent on time and concentration. In addition, the close contact of WS<sub>2</sub> nanosheets to the bacterium's cell membrane caused cell death and damage to the membrane. Additionally, Wang et al. [231] developed N-doped and defect-rich WS<sub>2</sub> nanosheets using a two-step gas expansion and exfoliation process. These nanosheets displayed good antibacterial properties due to the cell wall-damaging ability of WS<sub>2</sub> and the healing improvement of bacteria-infected wounds through the enhancement of peroxidase-like catalytic activity (Fig. 19b and c). Gao et al. [232] reported a facile and in-situ growth method of silver nanoparticles on exfoliated WS<sub>2</sub> nanosheet. The antibacterial property of the developed WS<sub>2</sub>/Ag<sub>2</sub>S heterojunction was further investigated using *Pseudomonas aeruginosa* (*P. aeruginosa*), *E. coli*, and *S. aureus* bacteria, displaying a highly enhanced antibacterial and durability, bringing a new perspective in biomedicine, food packing, and water disinfection fields. Lastly, Kim et al. [233] explored the antibacterial activities of MoS<sub>2</sub>, WS<sub>2</sub>, and MoSe<sub>2</sub> toward *E. coli* bacteria. The antibacterial capacity of these TMDs was investigated through their electrical conductivity and chemical oxidizing capability, which lead to ongoing bacterial disruption and the loss of cellular components (Fig. 19d). Interestingly, the antibacterial properties of 1T-phase WS<sub>2</sub> were remarkable, referring to its increased production of reactive

oxygen species (ROS), along with a strong ability to oxidize glutathione and the physical stress imposed on the bacterial cell membrane.

4.2.4. Tissue engineering and implant

Tungsten disulfide with its nanotube configuration (WSNTs) possesses a high bending modulus of 217 GPa [234,235] and an outstanding mechanical property over Young’s modulus of 150 GPa, along with the dispersion possibility in polymers, resins, epoxy, and organic solvent [236]. Such appealing characteristics of WSNTs were found to expand their potential in extending the mechanical properties of biodegradable polymers in bone tissue engineering [237]. For instance, Lalwani et al. [238] explored the potential application of WSNTs in the reinforcement of poly (propylene fumarate) (PPF) composite at a concentration of 0.01–0.2 wt% (Fig. 20). The WSNTs demonstrated a uniform dispersion with high crosslinking density and no aggregation in the polymer matrix (Fig. 20a–f). Instead, Single-walled carbon nanotubes (SWCNTs) and MWCNTs displayed a micron-sized aggregation in the PPF matrix. Besides, WSNTs-reinforced PPF nanocomposites displayed a notable improvement in mechanical properties as that of neat PPF (Fig. 20g–i), making the WSNTs an attractive candidate for tissue engineering applications.

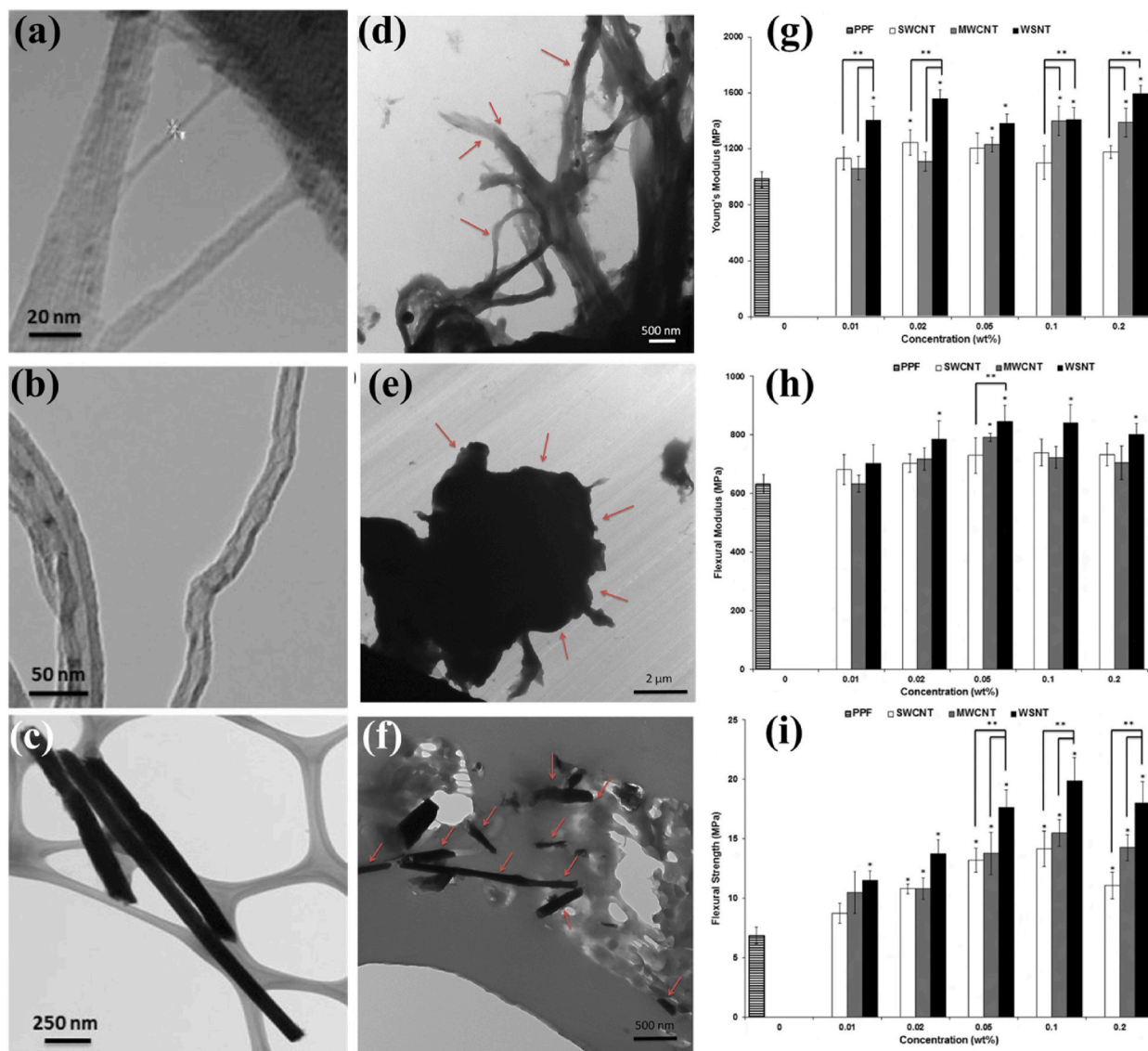


Fig. 20. WSNTs reinforced PPF for bone tissue engineering. TEM images of (a) SWCNTs, (b) MWCNTs, (c) and WSNTs. TEM images of PPF loaded (a) SWCNTs, (b) MWCNTs, and (c) and WSNTs. Red arrows represent the nanoparticles existence. (g) Compressive Modulus, (h) flexural modulus and (i) flexural yield strength of PPF and PPF loaded SWCNTs, MWCNTs, and WSNTs at various concentration. Reproduced with permission from Ref. [238]. Copyright 2013, Elsevier B.V. (For interpretation of the references to color in this figure legend, the reader is referred to the Web version of this article.)

Orthodontic treatment involves dental arch and archwires, mainly consisting of friction force between the wire and bracket that works against the orthodontic force. Nowadays, the primary focus is reducing friction, shortening treatment time, and minimizing root resorption risk. In this framework, the hexagonal structure of tungsten disulfide ( $WS_2$ ) has been identified as an ideal candidate due to its exceptional lubricating property, that under specific conditions, such a structure can even bend to form graphite-like configurations [239]. Accordingly, Gracco et al. [240] investigated the effect of Ni, Ni +  $MoS_2$ , and Ni +  $WS_2$  coated stainless steel on Damon Q and In-Ovation self-ligating brackets under dry and wet conditions. Electrodeposition was used to apply nanoparticles to the steel at a coating thickness of 10  $\mu m$ , 15  $\mu m$ , and 20  $\mu m$  for Ni, Ni +  $WS_2$ , and Ni +  $MoS_2$ , respectively. In testing, only Ni-coated wires showed no damage under the maximum binding, while coating with nanoparticles reduced friction compared to uncoated steel. The authors found that Ni +  $WS_2$  and Ni +  $MoS_2$  performed better than stainless steel or Ni-coated steel, significantly decreasing friction between the archwire and In-Ovation bracket under dry conditions.

Additionally, the use of fullerene-like tungsten disulfide ( $WS_2$ ) has led to the development of orthodontic stainless-steel wires with enhanced properties. Giving the example of Redlich et al. [241] work, in which they used the electroless deposition method to deposit the nickel-phosphorus (Ni-P) and  $WS_2$  on stainless steel for tooth sliding model design. Consequently, the friction coefficients decreased from 0.25 to 0.08 with a reduction of force by up to 54 %. Whereas Tammaro et al. [242] designed a nanocomposite made of  $WS_2$  and Poly (L-lactide) (PLLA) for bioresorbable vascular scaffolds (BVS). The  $WS_2$  nanoparticles, with their exceptional mechanical and flexible properties, were found to increase the strength of PLLA without thickness affect. After solvent casting, the PLLA- $WS_2$  composite was synthesized by adding 0.05 %  $WS_2$  to PLLA followed by hot press method. The composite's mechanical properties were tested by stretching it at a rate of 500 mm/min and 90 °C temperature. The results showed up to 100 % strain in both nanocomposite and neat polymer in the stress-strain profile.

Tungsten disulfide in TMDCs, with its good biocompatibility and photoelectrochemical properties, as against uncontrollable degradation rate and bioactivity lack of currently used materials in bone fractures and osteoporosis treatment, is recently described as a potential competitor. Chen et al. [243] used the chlorophyll molecules for the synthesis of the  $WS_2$  nanosheet through the liquid-phase exfoliation method, which was further mixed with polycaprolactone (PCL) and calcium silicate (CS) to form the biocompatible composite of  $WS_2$ /PCL/CS. The obtained composite displays no toxicity, while its macro-pore structure facilitated better nutrient transport, osteogenesis, angiogenesis, and cell growth. Compared to PCL/CS solely, the manufactured composite of  $WS_2$ /PCL/CS showed an increase in Young's modulus from 32 MPa to 145 MPa and improved compression strength from 2 MPa to 6 MPa. In addition, the in vivo bone regeneration study demonstrated a 120 % improvement compared to commercially available mineral trioxide aggregate material and a 300 % enhancement in mechanical properties compared to PCL/CS, making the suggested  $WS_2$ /PCL/CS an excellent candidate for bone regeneration composites.

## 5. Summary and outlook

Over the past two decades, significant progress in 2D  $WS_2$  material research has resulted in an exponential increase in publications yearly. Therefore, this review not only provides a comprehensive overview of the fundamental properties and up-to-date account of CVD-based  $WS_2$  growth methods but also serves as an in-depth summary of the  $WS_2$  research trends in biosensing and nanomedicine applications. Despite the potential advances in  $WS_2$ -based nanoarchitecture for biomedical applications, commercial products from these research efforts remain limited, which calls for more attention.

Even with the delightful achievement of synthesizing and utilizing  $WS_2$ , there are still significant opportunities for further advancement. The practical applications of  $WS_2$  require reliable production methods. However, large-scale synthesis of  $WS_2$  with a high-quality and controllable layer number remains a major challenge. On the other hand, large-area growth of monolayer  $WS_2$  can be obtained using various CVD methods, but not with sufficient quality for industrial applications. Furthermore, the growth of high-quality  $WS_2$  films typically requires high temperatures, which is incompatible with standard COMS technology. As such, developing low-temperature growth techniques or an effective contamination-free and crackless transfer method to transfer synthesized  $WS_2$  to target substrates is crucial. While certain low-temperature growth techniques have been devised, the quality of the synthesized  $WS_2$  has not yet reached that of mechanically exfoliated  $WS_2$  flakes. Nevertheless, the ongoing progress in sophisticated synthetic methods within laboratories holds promise for achieving applications that have the potential to revolutionize biosensing and the nanomedicine field.

Regarding  $WS_2$  toxicity and biocompatibility, numerous studies have demonstrated the favorable biocompatibility of  $WS_2$  for both in vitro and in vivo applications. Despite this, there is still a big question mark over its safety. Accordingly, toxicology tests still need to be conducted as a design guideline for developing appropriate toxicological evaluation criteria, enabling the full exploitation of  $WS_2$  clinical potential. Accordingly, to unlock the full potential of therapeutic  $WS_2$  nanomaterials in clinical settings, it is imperative to foster increased cooperation and synergy among material scientists, biologists, chemists, toxicologists, physicists, and medical scientists.

Besides, to advance the development toward the next generation of  $WS_2$ -based biosensors, it is crucial to consider the possibility of its integration, implantability, and miniaturization. In addition, during the detection stage, complex biological environments can have a degradable effect on the  $WS_2$  biosensor performance. Therefore, it is necessary to conduct thorough examinations of the  $WS_2$  stability and coating strategy to prevent degradation and enhance the device's sensing abilities. Similarly, future research related to  $WS_2$ -based anti-cancer agents should prioritize accurate targeting, treatment dosage, and evaluation of the treatment progression to allow for simultaneous treatment of multiple tumors, as well as biodegradability and rapid elimination, to avoid potential long-term toxicity.

Future research on nanomaterial-based biomedical applications should focus on converging biosensing systems with therapeutic capabilities within a unified theranostic platform, presenting significant potential in biomedicine. Ongoing research endeavors are

focused on seamlessly incorporating nanomaterials into micro-devices using wireless technology, specifically for early cancer detection. In theory, biosensors based on WS<sub>2</sub> nanoarchitecture could discern tumor markers and transmit information wirelessly to surface electronic devices. These devices, equipped with algorithms designed to create personalized treatment plans, guide the WS<sub>2</sub> nanomaterial to release drugs through wireless signals. Upon completion of the therapeutic process, the WS<sub>2</sub> undergoes biodegradation, detaches from micro-devices, and is subsequently eliminated from the body.

In conclusion, TMDCs WS<sub>2</sub> possess favorable biocompatibility and diverse properties, making it a competitive alternative candidate in various fields such as antibacterial, bioimaging/therapy, and biosensing applications. More in-depth studies of its unique features, medical applications, and toxicity levels still need to be performed to enhance the emergence of the WS<sub>2</sub> as a strong contender in clinical practice.

### CRedit authorship contribution statement

**Mohamed Bahri:** Writing – original draft, Conceptualization. **Dongmei Yu:** Conceptualization. **Can Yang Zhang:** Writing – review & editing. **Zhenglin Chen:** Writing – review & editing. **Chengming Yang:** Writing – review & editing. **Lyes Douadji:** Methodology, Formal analysis. **Peiwu Qin:** Writing – review & editing, Supervision, Funding acquisition.

### Declaration of competing interest

The authors declare that they have no known competing financial interests or personal relationships that could have appeared to influence the work reported in this paper.

### Acknowledgments

The authors appreciate the supports from the National Natural Science Foundation of China 31970752, 32350410397; Science Technology Innovation Commission of Shenzhen Municipality, JCYJ20220530143014032, JCYJ20230807113017035, WDZC20200820173710001; Shenzhen Medical Research Funds, D2301002; Department of Chemical Engineering-iBHE special cooperation joint fund project, DCE-iBHE-2022-3; Tsinghua Shenzhen International Graduate School Cross-disciplinary Research and Innovation Fund Research Plan, JC2022009; and Bureau of Planning, Land and Resources of Shenzhen Municipality (2022) 207. The authors are indebted for the generous permission granted by the respective publishers/authors to include their figures, in this article.

### Data availability statement

Data will be made available on request.

### References

- [1] M. Bahri, S.H. Gebre, M.A. Elaguech, F.T. Dajan, M.G. Sendeku, C. Tlili, D. Wang, Recent advances in chemical vapour deposition techniques for graphene-based nanoarchitectures: from synthesis to contemporary applications, *Coord. Chem. Rev.* 475 (2023) 214910, <https://doi.org/10.1016/J.CCR.2022.214910>.
- [2] A. Kumar, L. Viscardi, E. Faella, F. Giubileo, K. Intonti, A. Pelella, S. Sleziona, O. Kharsah, M. Schleberger, A. Di Bartolomeo, Black phosphorus unipolar transistor, memory, and photodetector, *J. Mater. Sci.* 58 (2023), <https://doi.org/10.1007/s10853-023-08169-0>.
- [3] G.A. Ozin, S. Ozkar, Intrazeolite metal carbonyl phototopaxy: from tungsten(VI) oxide quantum dots to a zero-dimensional semiconductor quantum supralattice, *J. Phys. Chem.* 94 (1990) 7556–7561, <https://doi.org/10.1021/J100382A046>.
- [4] Z. Wang, C. Zhao, R. Gui, H. Jin, J. Xia, F. Zhang, Y. Xia, Synthetic methods and potential applications of transition metal dichalcogenide/graphene nanocomposites, *Coord. Chem. Rev.* 326 (2016) 86–110, <https://doi.org/10.1016/J.CCR.2016.08.004>.
- [5] C. Cao, Y. Qu, M. Bahri, D. Lyes, D. Wang, Toward selective transfer of CVD monolayer WS<sub>2</sub> based on laser-cutting dedicated FET applications, <https://doi.org/10.1117/12.2668065>, 2023.
- [6] A. Pelella, O. Kharsah, A. Grillo, F. Urban, M. Passacantando, F. Giubileo, L. Iemmo, S. Sleziona, E. Pollmann, L. Madauß, M. Schleberger, A. Di Bartolomeo, Electron irradiation of metal contacts in monolayer MoS<sub>2</sub> field-effect transistors, *ACS Appl. Mater. Interfaces* 12 (2020), <https://doi.org/10.1021/acsami.0c11933>.
- [7] R. Gangopadhyay, A. De, Conducting polymer nanocomposites: a brief overview, *Chem. Mater.* 12 (2000) 608–622, <https://doi.org/10.1021/CM990537F>.
- [8] W. Choi, N. Choudhary, G.H. Han, J. Park, D. Akinwande, Y.H. Lee, Recent development of two-dimensional transition metal dichalcogenides and their applications, *Mater. Today* 20 (2017) 116–130, <https://doi.org/10.1016/J.MATTOD.2016.10.002>.
- [9] L. Wang, D. Xu, L. Jiang, J. Gao, Z. Tang, Y. Xu, X. Chen, H. Zhang, Transition metal dichalcogenides for sensing and oncotherapy: status, challenges, and perspective, *Adv. Funct. Mater.* 31 (2021), <https://doi.org/10.1002/ADFM.202004408>.
- [10] S. Anju, P.v. Mohanan, Biomedical applications of transition metal dichalcogenides (TMDCs), *Synth. Met.* 271 (2021) 116610, <https://doi.org/10.1016/J.SYNTHMET.2020.116610>.
- [11] W.J. Schutte, J.L. de Boer, F. Jellinek, Crystal structures of tungsten disulfide and diselenide, *J. Solid State Chem.* 70 (1987) 207–209, [https://doi.org/10.1016/0022-4596\(87\)90057-0](https://doi.org/10.1016/0022-4596(87)90057-0).
- [12] D. Singh Rana, N. Thakur, D. Singh, P. Sonia, Molybdenum and tungsten disulfide based nanocomposites as chemical sensor: a review, *Mater. Today Proc.* 62 (2022) 2755–2761, <https://doi.org/10.1016/J.MATPR.2022.01.147>.
- [13] C. Lan, C. Li, J.C. Ho, Y. Liu, 2D WS<sub>2</sub>: from vapor phase synthesis to device applications, *Adv. Electron. Mater.* 7 (2021) 2000688, <https://doi.org/10.1002/AELM.202000688>.
- [14] C. Murugan, V. Sharma, R.K. Murugan, G. Malaiamegu, A. Sundaramurthy, Two-dimensional cancer theranostic nanomaterials: synthesis, surface functionalization and applications in photothermal therapy, *J. Contr. Release* 299 (2019) 1–20, <https://doi.org/10.1016/J.JCONREL.2019.02.015>.

- [15] M. Ensoylu, A.M. Deliormanli, H. Atmaca, Tungsten disulfide nanoparticle-containing PCL and PLGA-coated bioactive glass composite scaffolds for bone tissue engineering applications, *J. Mater. Sci.* 56 (2021) 18650–18667, <https://doi.org/10.1007/S10853-021-06494-W>.
- [16] Y. Zhang, J. Zhang, Q. Jia, J. Ge, P. Wang, Innovative strategies of hydrogen peroxide-involving tumor therapeutics, *Mater. Chem. Front.* 5 (2021) 4474–4501, <https://doi.org/10.1039/D1QM00134E>.
- [17] W.Z. Teo, E.L.K. Chng, Z. Sofer, M. Pumera, Cytotoxicity of Exfoliated Transition-Metal Dichalcogenides (MoS<sub>2</sub>, WS<sub>2</sub>, and WSe<sub>2</sub>) is Lower Than That of Graphene and its Analogues, *Chem. Eur. J.* 20 (2014) 9627–9632, <https://doi.org/10.1002/CHEM.201402680>.
- [18] Z. Kayani, N. Islami, N. Behzadpour, N. Zahraie, S. Imanlou, P. Tamaddon, F. Salehi, F. Daneshvar, G. Perota, E. Sorati, S. Mohammadi, N. Sattarahmady, Combating cancer by utilizing noble metallic nanostructures in combination with laser photothermal and X-ray radiotherapy, *J. Drug Deliv. Sci. Technol.* 65 (2021) 102689, <https://doi.org/10.1016/J.JDDST.2021.102689>.
- [19] L. Liu, K. Ye, C. Lin, Z. Jia, T. Xue, A. Nie, Y. Cheng, J. Xiang, C. Mu, B. Wang, F. Wen, K. Zhai, Z. Zhao, Y. Gong, Z. Liu, Y. Tian, Grain-boundary-rich polycrystalline monolayer WS<sub>2</sub> film for atomolar-level Hg<sup>2+</sup> sensors, *Nat. Commun.* 12 (2021) 1–12, <https://doi.org/10.1038/s41467-021-24254-x> (2021) 1–8.
- [20] L. Liu, K. Ye, Q. Zhan, T. Xue, K. Zhai, Y. Cheng, Z. Jia, A. Nie, J.Y. Xiang, C.P. Mu, B. Wang, F. Wen, Z. Zhao, Y. Gong, Y. Tian, Z. Liu, Ultrasensitive biochemical sensors based on controllably grown films of high-density edge-rich multilayer WS<sub>2</sub> islands, *Sensor. Actuator. B Chem.* 353 (2022) 131081, <https://doi.org/10.1016/J.SNB.2021.131081>.
- [21] M. Bahri, B. Shi, M.A. Elaguech, K. Djebbi, D. Zhou, L. Liang, C. Thili, D. Wang, Tungsten disulfide nanosheet-based field-effect transistor biosensor for DNA hybridization detection, *ACS Appl. Nano Mater.* 5 (2022) 5035–5044, <https://doi.org/10.1021/ACSANM.2C00067>.
- [22] M. Pumera, A.H. Loo, Layered transition-metal dichalcogenides (MoS<sub>2</sub> and WS<sub>2</sub>) for sensing and biosensing, *TrAC, Trends Anal. Chem.* 61 (2014) 49–53, <https://doi.org/10.1016/J.TRAC.2014.05.009>.
- [23] Q. Palomar, C. Gondran, J.P. Lellouche, S. Cosnier, M. Holzinger, Functionalized tungsten disulfide nanotubes for dopamine and catechol detection in a tyrosinase-based amperometric biosensor design, *J. Mater. Chem. B* 8 (2020) 3566–3573, <https://doi.org/10.1039/C9TB01926J>.
- [24] M. Ghodrati, A. Mir, A. Farmani, Sensitivity-enhanced surface plasmon resonance sensor with bimetal/tungsten disulfide (WS<sub>2</sub>)/MXene (Ti<sub>3</sub>C<sub>2</sub>T<sub>x</sub>) hybrid structure, *Plasmonics* 17 (2022) 1973–1984, <https://doi.org/10.1007/S11468-022-01685-W>.
- [25] C. Gu, Z. Wang, Y. Pan, S. Zhu, Z. Gu, Tungsten-based nanomaterials in the biomedical field: a bibliometric analysis of research progress and prospects, *Adv. Mater.* 35 (2023) 2204397, <https://doi.org/10.1002/ADMA.202204397>.
- [26] A. Bolotsky, D. Butler, C. Dong, K. Gerace, N.R. Glavin, C. Muratore, J.A. Robinson, A. Ebrahimi, Two-dimensional materials in biosensing and healthcare: from in vitro diagnostics to optogenetics and beyond, *ACS Nano* 13 (2019) 9781–9810, <https://doi.org/10.1021/acsnano.9b03632>.
- [27] M.Y. Li, C.H. Chen, Y. Shi, L.J. Li, Heterostructures based on two-dimensional layered materials and their potential applications, *Mater. Today* 19 (2016) 322–335, <https://doi.org/10.1016/J.MATTOD.2015.11.003>.
- [28] Z. Cai, B. Liu, X. Zou, H.M. Cheng, Chemical vapor deposition growth and applications of two-dimensional materials and their heterostructures, *Chem. Rev.* 118 (2018) 6091–6133, <https://doi.org/10.1021/ACS.CHEMREV.7B00536>.
- [29] G.R. Bhimanapati, Z. Lin, V. Meunier, Y. Jung, J. Cha, S. Das, D. Xiao, Y. Son, M.S. Strano, V.R. Cooper, L. Liang, S.G. Louie, E. Ringe, W. Zhou, S.S. Kim, R. R. Naik, B.G. Sumpter, H. Terrones, F. Xia, Y. Wang, J. Zhu, D. Akinwande, N. Alem, J.A. Schuller, R.E. Schaak, M. Terrones, J.A. Robinson, Recent advances in two-dimensional materials beyond graphene, *ACS Nano* 9 (2015) 11509–11539, <https://doi.org/10.1021/ACS.NANO.5B05556>.
- [30] G. Plechinger, P. Nagler, J. Kraus, N. Paradiso, C. Strunk, C. Schüller, T. Korn, Identification of excitons, trions and biexcitons in single-layer WS<sub>2</sub>, *Phys. Status Solidi Rapid Res. Lett.* 9 (2015) 457–461, <https://doi.org/10.1002/PSSR.201510224>.
- [31] L. Ottaviano, S. Palleschi, F. Perrozzi, G. D'Olimpio, F. Priante, M. Donarelli, P. Benassi, M. Nardone, M. Gonchigsuren, M. Gombosuren, A. Lucia, G. Moccia, O.A. Cacioppo, Mechanical exfoliation and layer number identification of MoS<sub>2</sub> revisited, *2D Mater.* 4 (2017) 045013, <https://doi.org/10.1088/2053-1583/AA8764>.
- [32] J.N. Coleman, M. Lotya, A. O'Neill, S.D. Bergin, P.J. King, U. Khan, K. Young, A. Gaucher, S. De, R.J. Smith, I.v. Shvets, S.K. Arora, G. Stanton, H.Y. Kim, K. Lee, G.T. Kim, G.S. Duesberg, T. Hallam, J.J. Boland, J.J. Wang, J.F. Donegan, J.C. Grunlan, G. Moriarty, A. Shmeliov, R.J. Nicholls, J.M. Perkins, E. M. Grievson, K. Theuwissen, D.W. McComb, P.D. Nellist, V. Nicolosi, Two-dimensional nanosheets produced by liquid exfoliation of layered materials, *Science* (2011) 568–571, <https://doi.org/10.1126/SCIENCE.1194975>, 1979). 331.
- [33] R. Yang, L. Mei, Q. Zhang, Y. Fan, H.S. Shin, D. Voiry, Z. Zeng, High-yield production of mono- or few-layer transition metal dichalcogenide nanosheets by an electrochemical lithium ion intercalation-based exfoliation method, *Nat. Protoc.* 17 (2022) 358–377, <https://doi.org/10.1038/s41596-021-00643-w>, 2022 17: 2.
- [34] L. Tian, H. Qiao, Z. Huang, X. Qi, Li-ion intercalated exfoliated WS<sub>2</sub> nanosheets with enhanced electrocatalytic hydrogen evolution performance, *Cryst. Res. Technol.* 56 (2021) 2000165, <https://doi.org/10.1002/CRRAT.202000165>.
- [35] D. Doonyapisut, P.K. Kannan, B. Kim, C.H. Chung, Electrochemically exfoliated WS<sub>2</sub> nanosheets for the electrochemical impedimetric detection of NADH, *Chemelectrochem* 8 (2021) 4597–4604, <https://doi.org/10.1002/CELC.202101343>.
- [36] B. Zhang, X. Chen, H. Zhao, H. Xie, H. Yin, Electrochemically exfoliated WS<sub>2</sub> in molten salt for sodium ion battery anode, *SSRN Electron. J.* (2022), <https://doi.org/10.2139/SSRN.4049703>.
- [37] D. Ovchinnikov, A. Allain, Y.S. Huang, D. Dumcenco, A. Kis, Electrical transport properties of single-layer WS<sub>2</sub>, *ACS Nano* 8 (2014) 8174–8181, <https://doi.org/10.1021/NN502362B>.
- [38] V. Nicolosi, M. Chhowalla, M.G. Kanatzidis, M.S. Strano, J.N. Coleman, Liquid exfoliation of layered materials, *Science* (2013) 340, <https://doi.org/10.1126/SCIENCE.1226419>, 1979.
- [39] X.Q. Zhang, C.H. Lin, Y.W. Tseng, K.H. Huang, Y.H. Lee, Synthesis of lateral heterostructures of semiconducting atomic layers, *Nano Lett.* 15 (2015) 410–415, <https://doi.org/10.1021/NL503744F>.
- [40] H. Kim, D. Ovchinnikov, D. Deiana, D. Unuchek, A. Kis, Suppressing nucleation in metal-organic chemical vapor deposition of MoS<sub>2</sub> monolayers by alkali metal halides, *Nano Lett.* 17 (2017) 5056–5063, <https://doi.org/10.1021/ACS.NANO.7B02311>.
- [41] H. Yin, X. Zhang, J. Lu, X. Geng, Y. Wan, M. Wu, P. Yang, Substrate effects on the CVD growth of MoS<sub>2</sub> and WS<sub>2</sub>, *J. Mater. Sci.* 55 (2020) 990–996, <https://doi.org/10.1007/S10853-019-03993-9>.
- [42] X. Ling, Y.H. Lee, Y. Lin, W. Fang, L. Yu, M.S. Dresselhaus, J. Kong, Role of the seeding promoter in MoS<sub>2</sub> growth by chemical vapor deposition, *Nano Lett.* 14 (2014) 464–472, <https://doi.org/10.1021/NL4033704>.
- [43] Y. Gao, Z. Liu, D.M. Sun, L. Huang, L.P. Ma, L.C. Yin, T. Ma, Z. Zhang, X.L. Ma, L.M. Peng, H.M. Cheng, W. Ren, Large-area synthesis of high-quality and uniform monolayer WS<sub>2</sub> on reusable Au foils, *Nat. Commun.* 6 (2015), <https://doi.org/10.1038/NCOMMS9569>.
- [44] S. Sharma, B.P. Jaisi, K.P. Sharma, M.I. Araby, G. Kalita, M. Tanemura, Synthesis of freestanding WS<sub>2</sub> trees and fibers on Au by chemical vapor deposition (CVD), *Phys. Status Solidi* 215 (2018) 1700566, <https://doi.org/10.1002/PSSA.201700566>.
- [45] A. Patsha, V. Sheff, A. Ismach, Seeded-growth of WS<sub>2</sub> atomic layers: the effect on chemical and optical properties, *Nanoscale* 11 (2019) 22493–22503, <https://doi.org/10.1039/C9NR06515F>.
- [46] J. Han, R. Fang, L. Zhu, Z. Geng, X. He, CVD growth of monolayer WS<sub>2</sub> through controlled growth temperature and time, *Ferroelectrics* 562 (1) (2020) 51–57.
- [47] W. Srirachat, U. Pancharoen, S. Kheawhom, An investigation of saturated vapor pressure regarding low-volatility organophosphorus extractants Di-(2-ethylhexyl) phosphoric acid and tributyl phosphate: correlation and thermodynamics study, *Vacuum* 156 (2018) 237–247, <https://doi.org/10.1016/J.VACUUM.2018.07.036>.
- [48] J. Park, W. Lee, T. Choi, S.H. Hwang, J.M. Myoung, J.H. Jung, S.H. Kim, H. Kim, Layer-modulated synthesis of uniform tungsten disulfide nanosheet using gas-phase precursors, *Nanoscale* 7 (2015) 1308–1313, <https://doi.org/10.1039/C4NR04292A>.
- [49] Y. Rong, Y. Fan, A. Leen Koh, A.W. Robertson, K. He, S. Wang, H. Tan, R. Sinclair, J.H. Warner, Controlling sulphur precursor addition for large single crystal domains of WS<sub>2</sub>, *Nanoscale* 6 (2014) 12096–12103, <https://doi.org/10.1039/C4NR04091K>.

- [50] B. Shi, D. Zhou, S. Fang, K. Djebbi, S. Feng, H. Zhao, C. Tlili, D. Wang, Facile and controllable synthesis of large-area monolayer WS<sub>2</sub> flakes based on WO<sub>3</sub> precursor drop-casted substrates by chemical vapor deposition, *Nanomaterials* 9 (2019), <https://doi.org/10.3390/nano9040578>.
- [51] S. Li, S. Wang, D.M. Tang, W. Zhao, H. Xu, L. Chu, Y. Bando, D. Golberg, G. Eda, Halide-assisted atmospheric pressure growth of large WSe<sub>2</sub> and WS<sub>2</sub> monolayer crystals, *Appl. Mater. Today* 1 (2015) 60–66, <https://doi.org/10.1016/j.apmt.2015.09.001>.
- [52] F. Reale, P. Palczynski, I. Amit, G.F. Jones, J.D. Mehew, A. Bacon, N. Ni, P.C. Sherrell, S. Agnoli, M.F. Craciun, S. Russo, C. Mattevi, High-mobility and high-optical quality atomically thin WS<sub>2</sub>, *Sci. Rep.* 7 (2017) 1–7, <https://doi.org/10.1038/s41598-017-14928-2>, 2017) 1–10.
- [53] B. Shi, D. Zhou, R. Qiu, M. Bahri, X. Kong, H. Zhao, C. Tlili, D. Wang, High-efficiency synthesis of large-area monolayer WS<sub>2</sub> crystals on SiO<sub>2</sub>/Si substrate via NaCl-assisted atmospheric pressure chemical vapor deposition, *Appl. Surf. Sci.* 533 (2020) 147479, <https://doi.org/10.1016/j.apsusc.2020.147479>.
- [54] H.G. Ji, Y.C. Lin, K. Nagashio, M. Maruyama, P. Solís-Fernández, A. Sukma Aji, V. Panchal, S. Okada, K. Suenaga, H. Ago, Hydrogen-assisted epitaxial growth of monolayer tungsten disulfide and seamless grain stitching, *Chem. Mater.* 30 (2018) 403–411, <https://doi.org/10.1021/ACS.CHEMMATER.7B04149>.
- [55] Y. Zhang, Y. Zhang, Q. Ji, J. Ju, H. Yuan, J. Shi, T. Gao, D. Ma, M. Liu, Y. Chen, X. Song, H.Y. Hwang, Y. Cui, Z. Liu, Controlled growth of high-quality monolayer WS<sub>2</sub> layers on sapphire and imaging its grain boundary, *ACS Nano* 7 (2013) 8963–8971, <https://doi.org/10.1021/NN403454E>.
- [56] A. Zafar, Z. Zafar, W. Zhao, J. Jiang, Y. Zhang, Y. Chen, J. Lu, Z. Ni, A. Zafar, J. Jiang, J. Lu, Z. Ni, Z. Zafar, W. Zhao, Y. Zhang, Y. Chen, Sulfur-mastery: precise synthesis of 2D transition metal dichalcogenides, *Adv. Funct. Mater.* 29 (2019) 1809261, <https://doi.org/10.1002/ADFM.201809261>.
- [57] L. Dong, Y. Wang, J. Sun, C. Pan, Q. Zhang, L. Gu, B. Wan, C. Song, F. Pan, C. Wang, Z. Tang, J. Zhang, Facile access to shape-controlled growth of WS<sub>2</sub> monolayer via environment-friendly method, *2D Mater.* 6 (2018) 015007, <https://doi.org/10.1088/2053-1583/AAE7EB>.
- [58] Y. Yue, J.C. Chen, Y. Zhang, S.S. Ding, F. Zhao, Y. Wang, D. Zhang, R.J. Li, H. Dong, W. Hu, Y. Feng, W. Feng, Two-dimensional high-quality monolayered triangular WS<sub>2</sub> flakes for field-effect transistors, *ACS Appl. Mater. Interfaces* 10 (2018) 22435–22444, <https://doi.org/10.1021/ACSAMI.8B05885>.
- [59] P. Liu, T. Luo, J. Xing, H. Xu, H. Hao, H. Liu, J. Dong, Large-area WS<sub>2</sub> film with big single domains grown by chemical vapor deposition, *Nanoscale Res. Lett.* 12 (2017) 1–10, <https://doi.org/10.1186/s11671-017-2329-9>.
- [60] A. Thangaraja, S.M. Shinde, G. Kalita, M. Tanemura, Effect of WO<sub>3</sub> precursor and sulfurization process on WS<sub>2</sub> crystals growth by atmospheric pressure CVD, *Mater. Lett.* 156 (2015) 156–160, <https://doi.org/10.1016/j.matlet.2015.05.020>.
- [61] C. Cong, J. Shang, X. Wu, B. Cao, N. Peimyo, C. Qiu, L. Sun, T. Yu, Synthesis and optical properties of large-area single-crystalline 2D semiconductor WS<sub>2</sub> monolayer from chemical vapor deposition, *Adv. Opt. Mater.* 2 (2014) 131–136, <https://doi.org/10.1002/ADOM.201300428>.
- [62] Z. Wang, Y. Xie, H. Wang, R. Wu, T. Nan, Y. Zhan, J. Sun, T. Jiang, Y. Zhao, Y. Lei, M. Yang, W. Wang, Q. Zhu, X. Ma, Y. Hao, NaCl-assisted one-step growth of MoS<sub>2</sub>-WS<sub>2</sub> in-plane heterostructures, *Nanotechnology* 28 (2017) 325602, <https://doi.org/10.1088/1361-6528/AA6F01>.
- [63] A. George, C. Neumann, D. Kaiser, R. Mupparapu, T. Lehnert, U. Hübner, Z. Tang, A. Winter, U. Kaiser, I. Staude, A. Turchanin, Controlled growth of transition metal dichalcogenide monolayers using Knudsen-type effusion cells for the precursors, *J. Phys.: Materials* 2 (2019) 016001, <https://doi.org/10.1088/2515-7639/AAF982>.
- [64] J. Zhou, J. Lin, X. Huang, Y. Zhou, Y. Chen, J. Xia, H. Wang, Y. Xie, H. Yu, J. Lei, D. Wu, F. Liu, Q. Fu, Q. Zeng, C.H. Hsu, C. Yang, L. Lu, T. Yu, Z. Shen, H. Lin, B.I. Yakobson, Q. Liu, K. Suenaga, G. Liu, Z. Liu, A library of atomically thin metal chalcogenides, *Nature* 556 (2018) 7701, <https://doi.org/10.1038/s41586-018-0008-3>, 556 (2018) 355–359.
- [65] X. Li, J. Zhang, N. Zhou, H. Xu, R. Yang, Insight into the role of H<sub>2</sub> in WS<sub>2</sub> growth by chemical vapor deposition, *ACS Appl. Electron. Mater.* 3 (2021), <https://doi.org/10.1021/acsaem.1c00891>.
- [66] K.N. Kang, K. Godin, E.H. Yang, The growth scale and kinetics of WS<sub>2</sub> monolayers under varying H<sub>2</sub> concentration, *Sci. Rep.* 5 (2015), <https://doi.org/10.1038/srep13205>.
- [67] H.M. Manasevit, SINGLE-CRYSTAL gallium arsenide on insulating substrates, *Appl. Phys. Lett.* 12 (2003) 156, <https://doi.org/10.1063/1.1651934>.
- [68] J. Cheon, J.E. Gozum, G.S. Girolami, Chemical vapor deposition of MoS<sub>2</sub> and TiS<sub>2</sub> films from the Metal–Organic precursors Mo(S<sub>2</sub>-t-Bu)<sub>4</sub> and Ti(S<sub>2</sub>-t-Bu)<sub>4</sub>, *Chem. Mater.* 9 (1997) 1847–1853, <https://doi.org/10.1021/CM970138P>.
- [69] S. Cwik, D. Mitoraj, O. Mendoza Reyes, D. Rogalla, D. Peeters, J. Kim, H.M. Schütz, C. Bock, R. Beranek, A. Devi, Direct growth of MoS<sub>2</sub> and WS<sub>2</sub> layers by metal organic chemical vapor deposition, *Adv. Mater. Interfac.* 5 (2018) 1800140, <https://doi.org/10.1002/ADML.201800140>.
- [70] D. Andrzejewski, H. Myja, M. Heuken, A. Grundmann, H. Kalisch, A. Vescan, T. Kümmell, G. Bacher, Scalable large-area p-i-n light-emitting diodes based on WS<sub>2</sub> monolayers grown via MOCVD, *ACS Photonics* 6 (2019) 1832–1839, <https://doi.org/10.1021/ACSPhotonics.9B00311>.
- [71] A. Cohen, A. Patsha, P.K. Mohapatra, M. Kazes, K. Ranganathan, L. Houben, D. Oron, A. Ismach, Growth-etch metal-organic chemical vapor deposition approach of WS<sub>2</sub> atomic layers, *ACS Nano* 15 (2021) 526–538, <https://doi.org/10.1021/ACSANO.0C05394>.
- [72] K. Kang, S. Xie, L. Huang, Y. Han, P.Y. Huang, K.F. Mak, C.J. Kim, D. Muller, J. Park, High-mobility three-atom-thick semiconducting films with wafer-scale homogeneity, *Nature* 520 (2015) 656–660, <https://doi.org/10.1038/nature14417>, 2015 520:7549.
- [73] T.H. Choudhury, H. Simchi, R. Boichot, M. Chubarov, S.E. Mohney, J.M. Redwing, Chalcogen precursor effect on cold-wall gas-source chemical vapor deposition growth of WS<sub>2</sub>, *Cryst. Growth Des.* 18 (2018) 4357–4364, <https://doi.org/10.1021/ACS.CGD.8B00306>.
- [74] A. Grundmann, D. Andrzejewski, T. Kümmell, G. Bacher, M. Heuken, H. Kalisch, A. Vescan, H<sub>2</sub>S-free metal-organic vapor phase epitaxy of coalesced 2D WS<sub>2</sub> layers on sapphire, *MRS Adv* 4 (2019) 593–599, <https://doi.org/10.1557/ADV.2018.669>.
- [75] A. Delabie, M. Caymax, B. Groven, M. Heyne, K. Haesevoets, J. Meersschant, T. Nuytten, H. Bender, T. Conard, P. Verdonck, S. van Elshocht, S. de Gendt, M. Heyns, K. Barla, I. Radu, A. Thean, Low temperature deposition of 2D WS<sub>2</sub> layers from WF<sub>6</sub> and H<sub>2</sub>S precursors: impact of reducing agents, *Chem. Commun.* 51 (2015) 15692–15695, <https://doi.org/10.1039/C5CC05272F>.
- [76] B. Groven, A.N. Mehta, H. Bender, Q. Smets, J. Meersschant, A. Franquet, T. Conard, T. Nuytten, P. Verdonck, W. Vandervorst, M. Heyns, I. Radu, M. Caymax, A. Delabie, Nucleation mechanism during WS<sub>2</sub> plasma enhanced atomic layer deposition on amorphous Al<sub>2</sub>O<sub>3</sub> and sapphire substrates, *J. Vac. Sci. Technol. A: Vacuum, Surfaces, and Films* 36 (2017) 01A105, <https://doi.org/10.1116/1.5003361>.
- [77] B. Groven, A. Nalin Mehta, H. Bender, J. Meersschant, T. Nuytten, P. Verdonck, T. Conard, Q. Smets, T. Schram, B. Schoenaers, A. Stesmans, V. Afanas' Ev, W. Vandervorst, M. Heyns, M. Caymax, I. Radu, A. Delabie, Two-dimensional crystal grain size tuning in WS<sub>2</sub> atomic layer deposition: an insight in the nucleation mechanism, *Chem. Mater.* 30 (2018) 7648–7663, <https://doi.org/10.1021/ACS.CHEMMATER.8B02924>.
- [78] B. Groven, M. Heyne, A. Nalin Mehta, H. Bender, T. Nuytten, J. Meersschant, T. Conard, P. Verdonck, S. van Elshocht, W. Vandervorst, S. de Gendt, M. Heyns, I. Radu, M. Caymax, A. Delabie, Plasma-enhanced atomic layer deposition of two-dimensional WS<sub>2</sub> from WF<sub>6</sub>, H<sub>2</sub> plasma, and H<sub>2</sub>S, *Chem. Mater.* 29 (2017) 2927–2938, <https://doi.org/10.1021/ACS.CHEMMATER.6B05214>.
- [79] J.G. Song, J. Park, W. Lee, T. Choi, H. Jung, C.W. Lee, S.H. Hwang, J.M. Myoung, J.H. Jung, S.H. Kim, C. Lamsalot-Matras, H. Kim, Layer-controlled, wafer-scale, and conformal synthesis of tungsten disulfide nanosheets using atomic layer deposition, *ACS Nano* 7 (2013) 11333–11340, <https://doi.org/10.1021/NN405194E>.
- [80] M.H. Heyne, J.F. de Marneffe, T. Nuytten, J. Meersschant, T. Conard, M. Caymax, I. Radu, A. Delabie, E.C. Neyts, S. de Gendt, The conversion mechanism of amorphous silicon to stoichiometric WS<sub>2</sub>, *J. Mater. Chem. C Mater* 6 (2018) 4122–4130, <https://doi.org/10.1039/C8TC00760H>.
- [81] A. v Kolobov, J. Tominaga, in: *Springer Series in Materials Science* 239 Two-Dimensional Transition-Metal Dichalcogenides, Springer Cham, Switzerland, 2016, [https://doi.org/10.1007/978-3-319-31450-1\\_XVII-538](https://doi.org/10.1007/978-3-319-31450-1_XVII-538).
- [82] Z.Y. Zhu, Y.C. Cheng, U. Schwingenschlög, Giant spin-orbit-induced spin splitting in two-dimensional transition-metal dichalcogenide semiconductors, *Phys. Rev. B Condens. Matter* 84 (2011) 153402, <https://doi.org/10.1103/PHYSREVB.84.153402>.
- [83] G. bin Liu, D. Xiao, Y. Yao, X. Xu, W. Yao, Electronic structures and theoretical modelling of two-dimensional group-VIB transition metal dichalcogenides, *Chem. Soc. Rev.* 44 (2015) 2643–2663, <https://doi.org/10.1039/C4CS00031B>.
- [84] H. Zeng, G. bin Liu, J. Dai, Y. Yan, B. Zhu, R. He, L. Xie, S. Xu, X. Chen, W. Yao, X. Cui, Optical signature of symmetry variations and spin-valley coupling in atomically thin tungsten dichalcogenides, *Sci. Rep.* 3 (2013) 1–5, <https://doi.org/10.1038/srep01608>, 2013 3:1.
- [85] D.W. Latzke, W. Zhang, A. Suslu, T.R. Chang, H. Lin, H.T. Jeng, S. Tongay, J. Wu, A. Bansil, A. Lanzara, Electronic structure, spin-orbit coupling, and interlayer interaction in bulk MoS<sub>2</sub> and WS<sub>2</sub>, *Phys. Rev. B Condens. Matter* 91 (2015) 235202, <https://doi.org/10.1103/PHYSREVB.91.235202>.

- [86] M. Bahri, B. Shi, K. Djebbi, M.A. Elaguech, D. Zhou, M. Ben Ali, C. Thili, D. Wang, Toward clean and crackless polymer-assisted transfer of CVD-grown graphene and its recent advances in GFET-based biosensors, *Mater. Today Chem.* 22 (2021) 100578, <https://doi.org/10.1016/J.MTChem.2021.100578>.
- [87] C. Sourisseau, F. Cruege, M. Fouassier, M. Alba, Second-order Raman effects, inelastic neutron scattering and lattice dynamics in 2H-WS<sub>2</sub>, *Chem. Phys.* 150 (1991) 281–293, [https://doi.org/10.1016/0301-0104\(91\)80136-6](https://doi.org/10.1016/0301-0104(91)80136-6).
- [88] A. Berkdemir, H.R. Gutiérrez, A.R. Botello-Méndez, N. Perea-López, A.L. Elías, C.I. Chia, B. Wang, V.H. Crespi, F. López-Urías, J.C. Charlier, H. Terrones, M. Terrones, Identification of individual and few layers of WS<sub>2</sub> using Raman Spectroscopy, *Sci. Rep.* 3 (2013) 1, <https://doi.org/10.1038/srep01755>, 3 (2013) 1–8.
- [89] C. Lan, Z. Zhou, Z. Zhou, C. Li, L. Shu, L. Shen, D. Li, R. Dong, S.P. Yip, J.C. Ho, Wafer-scale synthesis of monolayer WS<sub>2</sub> for high-performance flexible photodetectors by enhanced chemical vapor deposition, *Nano Res.* 11 (2017) 3371–3384, <https://doi.org/10.1007/S12274-017-1941-4>, 6. 11 (2018).
- [90] W. Zhao, Z. Ghorannevis, K.K. Amara, J.R. Pang, M. Toh, X. Zhang, C. Kloc, P.H. Tan, G. Eda, Lattice dynamics in mono- and few-layer sheets of WS<sub>2</sub> and WSe<sub>2</sub>, *Nanoscale* 5 (2013) 9677–9683, <https://doi.org/10.1039/C3NR03052K>.
- [91] Y. Wang, C. Cong, W. Yang, J. Shang, N. Peimyooy, Y. Chen, J. Kang, J. Wang, W. Huang, T. Yu, Strain-induced direct–indirect bandgap transition and phonon modulation in monolayer WS<sub>2</sub>, *Nano Res.* 8 (2015) 2562–2572, <https://doi.org/10.1007/S12274-015-0762-6>, 2015 8:8.
- [92] H.M.W. Khalil, M.F. Khan, J. Eom, H. Noh, Highly stable and tunable chemical doping of multilayer WS<sub>2</sub> field effect transistor: reduction in contact resistance, *ACS Appl. Mater. Interfaces* 7 (2015) 23589–23596, <https://doi.org/10.1021/ACSAMI.5B06825>.
- [93] M.W. Iqbal, M.Z. Iqbal, M.F. Khan, M.A. Kamran, A. Majid, T. Alharbi, J. Eom, Tailoring the electrical and photo-electrical properties of a WS<sub>2</sub> field effect transistor by selective n-type chemical doping, *RSC Adv.* 6 (2016) 24675–24682, <https://doi.org/10.1039/C6RA02390H>.
- [94] N. Peimyooy, W. Yang, J. Shang, X. Shen, Y. Wang, T. Yu, Chemically driven tunable light emission of charged and neutral excitons in monolayer WS<sub>2</sub>, *ACS Nano* 8 (2014) 11320–11329, <https://doi.org/10.1021/NN504196N>.
- [95] Z. Jin, X. Li, J.T. Mullen, K.W. Kim, Intrinsic transport properties of electrons and holes in monolayer transition-metal dichalcogenides, *Phys. Rev. B Condens. Matter* 90 (2014) 045422, <https://doi.org/10.1103/PhysRevB.90.045422>.
- [96] W. Zhang, Z. Huang, W. Zhang, Y. Li, Two-dimensional semiconductors with possible high room temperature mobility, *Nano Res.* 7 (2014) 1731–1737, <https://doi.org/10.1007/S12274-014-0532-X>.
- [97] L. Britnell, R.M. Ribeiro, A. Eckmann, R. Jalil, B.D. Belle, A. Mishchenko, Y.J. Kim, R.v. Gorbachev, T. Georgiou, S.v. Morozov, A.N. Grigorenko, A.K. Geim, C. Casiraghi, A.H. Castro Neto, K.S. Novoselov, Strong light-matter interactions in heterostructures of atomically thin films, *Science* (2013) 1311–1314, <https://doi.org/10.1126/SCIENCE.1235547>, 1979). 340.
- [98] M. Bernardi, M. Palumbo, J.C. Grossman, Extraordinary sunlight absorption and one nanometer thick photovoltaics using two-dimensional monolayer materials, *Nano Lett.* 13 (2013) 3664–3670, <https://doi.org/10.1021/NL401544Y>.
- [99] S. Chen, W. Yang, Flexible low-dimensional semiconductor field emission cathodes: fabrication, properties and applications, *J Mater Chem C Mater* 5 (2017), <https://doi.org/10.1039/c7tc03081a>.
- [100] A. Patra, M.A. More, D.J. Late, C.S. Rout, Field emission applications of graphene-analogous two-dimensional materials: recent developments and future perspectives, *J Mater Chem C Mater* 9 (2021), <https://doi.org/10.1039/d1tc02054d>.
- [101] L. Chen, H. Yu, J. Zhong, J. Wu, W. Su, Graphene based hybrid/composite for electron field emission: a review, *J. Alloys Compd.* 749 (2018), <https://doi.org/10.1016/j.jallcom.2018.03.100>.
- [102] G. Viskadourous, A. Zak, M. Stylianakis, E. Kymakis, R. Tenne, E. Stratakis, Enhanced field emission of WS<sub>2</sub> nanotubes, *Small* 10 (2014) 2398–2403, <https://doi.org/10.1002/SMLL.201303340>.
- [103] S.R. Suryawanshi, P.S. Kolhe, C.S. Rout, D.J. Late, M.A. More, Spectral analysis of the emission current noise exhibited by few layer WS<sub>2</sub> nanosheets emitter, *Ultramicroscopy* 149 (2015), <https://doi.org/10.1016/j.ultramic.2014.10.004>.
- [104] A. Grillo, M. Passacantando, A. Zak, A. Pelella, A. Di Bartolomeo, W.S.2 Nanotubes, Electrical conduction and field emission under electron irradiation and mechanical stress, *Small* 16 (2020), <https://doi.org/10.1002/sml.202002880>.
- [105] E.B. Goldman, A. Zak, R. Tenne, E. Kartvelishvili, S. Levin-Zaidman, Y. Neumann, R. Stiubea-Cohen, A. Palmon, A.H. Hovav, D.J. Afraimian, Biocompatibility of tungsten disulfide inorganic nanotubes and fullerene-like nanoparticles with salivary gland cells, *Tissue Eng.* 21 (2015) 1013–1023, <https://doi.org/10.1089/TEN.TEA.2014.0163>.
- [106] J.H. Appel, D.O. Li, J.D. Podlevsky, A. Debnath, A.A. Green, Q.H. Wang, J. Chae, Low cytotoxicity and genotoxicity of two-dimensional MoS<sub>2</sub> and WS<sub>2</sub>, *ACS Biomater. Sci. Eng.* 2 (2016) 361–367, <https://doi.org/10.1021/ACSBiomaterials.5B00467>.
- [107] H. Turkez, E. Sonmez, O. Turkez, Y.I. Mokhtar, A. di Stefano, G. Turgut, The risk evaluation of tungsten oxide nanoparticles in cultured rat liver cells for its safe applications in nanotechnology, *Braz. Arch. Biol. Technol.* 57 (2014) 532–541, <https://doi.org/10.1590/S1516-89132014005000021>.
- [108] G. Hasegawa, M. Shimonaka, Y. Ishihara, Differential genotoxicity of chemical properties and particle size of rare metal and metal oxide nanoparticles, *J. Appl. Toxicol.* 32 (2012) 72–80, <https://doi.org/10.1002/JAT.1719>.
- [109] S. Chinde, N. Dumala, M.F. Rahman, S.S.K. Kamal, S.I. Kumari, M. Mahboob, P. Grover, Toxicological assessment of tungsten oxide nanoparticles in rats after acute oral exposure, *Environ. Sci. Pollut. Control Ser.* 24 (2017) 13576–13593, <https://doi.org/10.1007/S11356-017-8892-X>.
- [110] J. Hao, G. Song, T. Liu, X. Yi, K. Yang, L. Cheng, Z. Liu, *In Vivo* long-term biodistribution, excretion, and toxicology of PEGylated transition-metal dichalcogenides MS<sub>2</sub> (M = Mo, W, Ti) nanosheets, *Adv. Sci.* 4 (2017), <https://doi.org/10.1002/ADVS.201600160>.
- [111] J. Laloy, H. Haguet, L. Alpan, D. Raichman, J.M. Dogné, J.P. Lellouche, Impact of functional inorganic nanotubes f-INTs-WS<sub>2</sub> on hemolysis, platelet function and coagulation, *Nano Converg* 5 (2018) 1–10, <https://doi.org/10.1186/S40580-018-0162-1>.
- [112] M. Pardo, T. Shuster-Meisles, S. Levin-Zaidman, A. Rudich, Y. Rudich, Low cytotoxicity of inorganic nanotubes and fullerene-like nanostructures in human bronchial epithelial cells: relation to inflammatory gene induction and antioxidant response, *Environ. Sci. Technol.* 48 (2014) 3457–3466, <https://doi.org/10.1021/ES500065Z>.
- [113] Y. Qin, Y. Ma, X. Jin, L. Zhang, G. Ye, S. Zhao, A sensitive fluorescence turn-on assay of bleomycin and nuclease using WS<sub>2</sub> nanosheet as an effective sensing platform, *Anal. Chim. Acta* 866 (2015) 84–89, <https://doi.org/10.1016/J.ACA.2015.01.049>.
- [114] Y. Yuan, R. Li, Z. Liu, Establishing water-soluble layered WS<sub>2</sub> nanosheet as a platform for biosensing, *Anal. Chem.* 86 (2014) 3610–3615, <https://doi.org/10.1021/AC5002096>.
- [115] X. Zuo, H. Zhang, Q. Zhu, W. Wang, J. Feng, X. Chen, A dual-color fluorescent biosensing platform based on WS<sub>2</sub> nanosheet for detection of Hg<sup>2+</sup> and Ag<sup>+</sup>, *Biosens. Bioelectron.* 85 (2016) 464–470, <https://doi.org/10.1016/j.bios.2016.05.044>.
- [116] Q. Xi, D.M. Zhou, Y.Y. Kan, J. Ge, Z.K. Wu, R.Q. Yu, J.H. Jiang, Highly sensitive and selective strategy for microRNA detection based on WS<sub>2</sub> nanosheet mediated fluorescence quenching and duplex-specific nuclease signal amplification, *Anal. Chem.* 86 (2014) 1361–1365, <https://doi.org/10.1021/AC403944C>.
- [117] J. Zhao, X. Jin, M. Vdovenko, L. Zhang, I.Y. Sakharov, S. Zhao, A WS<sub>2</sub> nanosheet based chemiluminescence resonance energy transfer platform for sensing biomolecules, *Chem. Commun.* 51 (2015) 11092–11095, <https://doi.org/10.1039/C5CC04381F>.
- [118] J. Zhao, Y. Ma, R. Kong, L. Zhang, W. Yang, S. Zhao, Tungsten disulfide nanosheet and exonuclease III co-assisted amplification strategy for highly sensitive fluorescence polarization detection of DNA glycosylase activity, *Anal. Chim. Acta* 887 (2015) 216–223, <https://doi.org/10.1016/J.ACA.2015.07.006>.
- [119] A.H. Loo, A. Bonanni, M. Pumera, Strong dependence of fluorescence quenching on the transition metal in layered transition metal dichalcogenide nanoflakes for nucleic acid detection, *Analyst* 141 (2016) 4654–4658, <https://doi.org/10.1039/C6AN00454G>.
- [120] M. Shorie, V. Kumar, H. Kaur, K. Singh, V.K. Tomer, P. Sabherwal, Plasmonic DNA hotspots made from tungsten disulfide nanosheets and gold nanoparticles for ultrasensitive aptamer-based SERS detection of myoglobin, *Mikrochim. Acta* 185 (2018), <https://doi.org/10.1007/S00604-018-2705-X>.
- [121] P. Wang, A. Wang, M.M. Hassan, Q. Ouyang, H. Li, Q. Chen, A highly sensitive upconversion nanoparticles-WS<sub>2</sub> nanosheet sensing platform for Escherichia coli detection, *Sensor. Actuator. B Chem.* 320 (2020) 128434, <https://doi.org/10.1016/J.SNB.2020.128434>.
- [122] X. Zuo, H. Dai, H. Zhang, J. Liu, S. Ma, X. Chen, A peptide-WS<sub>2</sub> nanosheet based biosensing platform for determination of  $\beta$ -secretase and screening of its inhibitors, *Analyst* 143 (2018) 4585–4591, <https://doi.org/10.1039/C8AN00132D>.

- [123] T.W. Kang, J. Han, S. Lee, L.J. Hwang, S.J. Jeon, J.M. Ju, M.J. Kim, J.K. Yang, B. Jun, C.H. Lee, S.U. Lee, J.H. Kim, 2D transition metal dichalcogenides with glucan multivalency for antibody-free pathogen recognition, *Nat. Commun.* 9 (2018) 1–10, <https://doi.org/10.1038/s41467-018-04997-w>, 2018 9:1.
- [124] J.K. Yang, H.R. Lee, L.J. Hwang, H.I. Kim, D. bin Yim, J.H. Kim, Fluorescent 2D WS<sub>2</sub> nanosheets bearing chemical affinity elements for the recognition of glycosylated hemoglobin, *Adv. Healthcare Mater.* 7 (2018) 1701496, <https://doi.org/10.1002/ADHM.201701496>.
- [125] M. Haddad Irani-nezhad, R. Jalili, E. Kohan, A. Khataee, Y. Yoon, Tungsten disulfide (WS<sub>2</sub>)/fluorescein ratiometric fluorescent probe for detection of cefixime residues in milk, *Environ. Res.* 205 (2022), <https://doi.org/10.1016/J.ENVSRES.2021.112512>.
- [126] X. Zhao, D. He, Y. Wang, C. Fu, Facile fabrication of tungsten disulfide quantum dots (WS<sub>2</sub> QDs) as effective probes for fluorescence detection of dopamine (DA), *Mater. Chem. Phys.* 207 (2018) 130–134, <https://doi.org/10.1016/J.MATCHEMPHYS.2017.12.045>.
- [127] X. Guo, Y. Wang, F. Wu, Y. Ni, S. Kokot, The use of tungsten disulfide dots as highly selective, fluorescent probes for analysis of nitrofurazone, *Talanta* 144 (2015) 1036–1043, <https://doi.org/10.1016/J.TALANTA.2015.07.055>.
- [128] Q. Ouyang, S. Zeng, L. Jiang, L. Hong, G. Xu, X.Q. Dinh, J. Qian, S. He, J. Qu, P. Coquet, K.T. Yong, Sensitivity enhancement of transition metal dichalcogenides/silicon nanostructure-based surface plasmon resonance biosensor, *Sci. Rep.* 6 (2016) 1, <https://doi.org/10.1038/srep28190>, 6 (2016) 1–13.
- [129] J.N. Nur, M.H.H. Hasib, F. Asrafy, K.N. Shushama, R. Inum, M.M. Rana, Improvement of the performance parameters of the surface plasmon resonance biosensor using Al<sub>2</sub>O<sub>3</sub> and WS<sub>2</sub>, *Opt. Quant. Electron.* 51 (2019) 1–11, <https://doi.org/10.1007/S11082-019-1886-9>.
- [130] M.S. Rahman, M.R. Hasan, K.A. Rikta, M.S. Anower, A novel graphene coated surface plasmon resonance biosensor with tungsten disulfide (WS<sub>2</sub>) for sensing DNA hybridization, *Opt. Mater.* 75 (2018) 567–573, <https://doi.org/10.1016/J.OPTMAT.2017.11.013>.
- [131] Z. Fredj, B. Singh, M. Bahri, M. Sawan, P. Montréal, P. Qin, Enzymatic electrochemical biosensors for neurotransmitters detection: recent achievements and trends, <https://doi.org/10.3390/chemosensors11070388>, 2023.
- [132] Z. Fredj, P. Wang, F. Ullah, M. Sawan, A nanoplatform-based aptasensor to electrochemically detect epinephrine produced by living cells, *Microchim. Acta* 190 (2023) 343, <https://doi.org/10.1007/s00604-023-05902-z>.
- [133] M. Bahri, I. Dermoul, M. Getaye, M. Ben Ali, E. Abdelhamid, 2D simulation of a microfluidic biosensor for CRP detection into a rotating micro-channel, *SN Appl. Sci.* 1 (2019), <https://doi.org/10.1007/s42452-019-1231-8>.
- [134] M. Bahri, P. Qin, Environment applications of non-layered 2D materials, *Semiconduct. Semimet.* 113 (2023) 277–295, <https://doi.org/10.1016/BS.SEMSEM.2023.09.008>.
- [135] Z. Fredj, M. Sawan, 2D-non-layered materials: advancement and application in biosensors, memristors, and energy storage, *Semiconduct. Semimet.* 113 (2023) 253–276, <https://doi.org/10.1016/BS.SEMSEM.2023.09.007>.
- [136] M. Bahri, I. Dermoul, M. Getaye, M.A. Elaguech, K. Djebbi, M. Ben Ali, C. Tlili, D. Wang, CRP binding kinetics enhancement using local narrowing into a bent channel: finite element analysis, *Engineering* 14 (2022) 62–75, <https://doi.org/10.4236/ENG.2022.141006>.
- [137] A. Li, J. Zhang, J. Qiu, Z. Zhao, C. Wang, C. Zhao, H. Liu, A novel aptameric biosensor based on the self-assembled DNA–WS<sub>2</sub> nanosheet architecture, *Talanta* 163 (2017) 78–84, <https://doi.org/10.1016/j.talanta.2016.10.088>.
- [138] J. Yang, L. Gao, C. Peng, W. Zhang, Construction of self-signal DNA electrochemical biosensor employing WS<sub>2</sub> nanosheets combined with Pln6COOH, *RSC Adv.* 9 (2019) 9613–9619, <https://doi.org/10.1039/C8RA10266J>.
- [139] R. Pourakbari, M. Yousefi, B. Khalilzadeh, M.H. Irani-nezhad, A. Khataee, L. Aghebati-Maleki, A. Soleimani, A. Kamrani, F. Chakari-Khiavi, R. Abolhasan, M. Motallebnezhad, F. Jadidi-Niaragh, B. Yousefi, H.S. Kafil, M. Hojjat-Farsangi, M.R. Rashidi, Early stage evaluation of colon cancer using tungsten disulfide quantum dots and bacteriophage nano-biocomposite as an efficient electrochemical platform, *Cancer Nanotechnol* 13 (2022) 1–17, <https://doi.org/10.1186/S12645-022-00113-2>.
- [140] H.-L. Shuai, K.-J. Huang, Y.-X. Chen, A layered tungsten disulfide/acetylene black composite based DNA biosensing platform coupled with hybridization chain reaction for signal amplification, *J. Mater. Chem. B* 4 (2016) 1186–1196, <https://doi.org/10.1039/C5TB02214B>.
- [141] K.J. Huang, Y.J. Liu, H.B. Wang, T. Gan, Y.M. Liu, L.L. Wang, Signal amplification for electrochemical DNA biosensor based on two-dimensional graphene analogue tungsten sulfide–graphene composites and gold nanoparticles, *Sensor. Actuator. B Chem.* 191 (2014) 828–836, <https://doi.org/10.1016/J.SNB.2013.10.072>.
- [142] Y. Wang, C. Gong, Y. Zhu, Q. Wang, L. Geng, Signal-on electrochemical aptasensor for sensitive detection of sulfamethazine based on carbon quantum dots/tungsten disulfide nanocomposites, *Electrochim. Acta* 393 (2021) 139054, <https://doi.org/10.1016/J.ELECTACTA.2021.139054>.
- [143] G. Wu, H. Zheng, Y. Xing, C. Wang, X. Yuan, X. Zhu, A sensitive electrochemical sensor for environmental toxicity monitoring based on tungsten disulfide nanosheets/hydroxylated carbon nanotubes nanocomposite, *Chemosphere* 286 (2022) 131602, <https://doi.org/10.1016/J.CHEMOSPHERE.2021.131602>.
- [144] B.G. Santos, J.M. Gonçalves, D.P. Rocha, G.S. Hígino, T.P. Yadav, J.J. Pedrotti, P.M. Ajayan, L. Angnes, Electrochemical sensor for isoniazid detection by using a WS<sub>2</sub>/CNTs nanocomposite, *Sensors and Actuators Reports* 4 (2022) 100073, <https://doi.org/10.1016/J.SNR.2021.100073>.
- [145] M. Garg, M. Chatterjee, A.L. Sharma, S. Singh, Label-free approach for electrochemical ferritin sensing using biosurfactant stabilized tungsten disulfide quantum dots, *Biosens. Bioelectron.* 151 (2020) 111979, <https://doi.org/10.1016/J.BIOS.2019.111979>.
- [146] X. Liu, H.L. Shuai, Y.J. Liu, K.J. Huang, An electrochemical biosensor for DNA detection based on tungsten disulfide/multi-walled carbon nanotube composites and hybridization chain reaction amplification, *Sensor. Actuator. B Chem.* 235 (2016) 603–613, <https://doi.org/10.1016/J.SNB.2016.05.132>.
- [147] A. Mishra, R. Pilloton, S. Jain, S. Roy, M. Khanuja, A. Mathur, J. Narang, Paper-based electrodes conjugated with tungsten disulfide nanostructure and aptamer for impedimetric detection of *Listeria monocytogenes*, *Biosensors* 12 (2022), <https://doi.org/10.3390/bios12020088>.
- [148] S.K. Mahobiya, B. Lalayan, N. Chauhan, M. Khanuja, N.K. Kuchhal, S.S. Islam, U. Jain, Tungsten disulfide decorated screen-printed electrodes for sensing of glycosylated hemoglobin, *ACS Omega* 7 (2022) 34676–34684, <https://doi.org/10.1021/acsomega.2c04926>.
- [149] W.W. Li, T.D.W. Claridge, Q. Li, M.R. Wormald, B.G. Davis, H. Bayley, Tuning the cavity of cyclodextrins: altered sugar adaptors in protein pores, *J. Am. Chem. Soc.* 133 (2011) 1987–2001, <https://doi.org/10.1021/JA1100867>.
- [150] B.I. Karawdeniya, Y.M.N.D.Y. Bandara, J.W. Nichols, R.B. Chevalier, J.R. Dwyer, Surveying silicon nitride nanopores for glycomics and heparin quality assurance, *Nat. Commun.* 9 (2018) 1, <https://doi.org/10.1038/s41467-018-05751-y>, 9 (2018) 1–8.
- [151] J.O. Im, S. Lindsay, X. Wang, P. Zhang, Single molecule identification and quantification of glycosaminoglycans using solid-state nanopores, *ACS Nano* 13 (2019) 6308–6318, <https://doi.org/10.1021/ACS.NANO.9B00618>.
- [152] A. Fennouri, J. List, J. Ducey, J. Dupasquier, V. Sukyte, S.F. Mayer, R.D. Vargas, L. Pascual Fernandez, F. Bertani, S. Rodriguez Gonzalo, J. Yang, M. Mayer, Tuning the diameter, stability, and membrane affinity of peptide pores by DNA-programmed self-assembly, *ACS Nano* 15 (2021) 11263–11275, <https://doi.org/10.1021/ACS.NANO.0C10311>.
- [153] D. Vikraman, R. Sathesnan, K.S. Kumar, K.R. Mahendran, Nanopore passport control for substrate-specific translocation, *ACS Nano* 14 (2020) 2285–2295, <https://doi.org/10.1021/ACS.NANO.9B09408>.
- [154] Y. Cai, B. Zhang, L. Liang, S. Wang, L. Zhang, L. Wang, H.L. Cui, Y. Zhou, D. Wang, A solid-state nanopore-based single-molecule approach for label-free characterization of plant polysaccharides, *Plant Commun* 2 (2021), <https://doi.org/10.1016/J.XPLC.2020.100106>.
- [155] K. Kim, C.H. Lee, C.B. Park, Chemical sensing platforms for detecting trace-level Alzheimer’s core biomarkers, *Chem. Soc. Rev.* 49 (2020) 5446–5472, <https://doi.org/10.1039/D0CS00107D>.
- [156] R. Kawano, T. Osaki, H. Sasaki, M. Takinoue, S. Yoshizawa, S. Takeuchi, Rapid detection of a cocaine-binding aptamer using biological nanopores on a chip, *J. Am. Chem. Soc.* 133 (2011) 8474–8477, <https://doi.org/10.1021/JA2026085>.
- [157] J. Wang, J.D. Prajapati, F. Gao, Y.L. Ying, U. Kleinekathöfer, M. Winterhalter, Y.T. Long, Identification of single amino acid chiral and positional isomers using an electrostatically asymmetric nanopore, *J. Am. Chem. Soc.* 144 (2022) 15072–15078, <https://doi.org/10.1021/JACS.2C03923>.
- [158] H. Shan, X. Li, L. Liu, D. Song, Z. Wang, Recent advances in nanocomposite-based electrochemical aptasensors for the detection of toxins, *J. Mater. Chem. B* 8 (2020) 5808–5825, <https://doi.org/10.1039/D0TB00705F>.
- [159] K. Chen, J. Kong, J. Zhu, N. Ermann, P. Predki, U.F. Keyser, Digital data storage using DNA nanostructures and solid-state nanopores, *Nano Lett.* 19 (2019) 1210–1215, <https://doi.org/10.1021/ACS.NANO.8B04715>.

- [160] M. Akeson, D. Branton, J.J. Kasianowicz, E. Brandin, D.W. Deamer, Microsecond time-scale discrimination among polycytidylic acid, polyadenylic acid, and polyuridylic acid as homopolymers or as segments within single RNA molecules, *Biophys. J.* 77 (1999) 3227–3233, [https://doi.org/10.1016/S0006-3495\(99\)77153-5](https://doi.org/10.1016/S0006-3495(99)77153-5).
- [161] M. Zhang, C. Chen, Y. Zhang, J. Geng, Biological nanopores for sensing applications, *Proteins: Struct., Funct., Bioinf.* 90 (2022) 1786–1799, <https://doi.org/10.1002/PROT.26308>.
- [162] L. Liang, F. Qin, S. Wang, J. Wu, R. Li, Z. Wang, M. Ren, D. Liu, D. Wang, D. Astruc, Overview of the materials design and sensing strategies of nanopore devices, *Coord. Chem. Rev.* 478 (2023) 214998, <https://doi.org/10.1016/j.CCR.2022.214998>.
- [163] J. Wang, Y. Zhou, L. Jiang, Bio-inspired track-etched polymeric nanochannels: steady-state biosensors for detection of analytes, *ACS Nano* (2021), <https://doi.org/10.1021/ACS.NANO.1C08582>.
- [164] N. Sakai, S. Matile, Synthetic ion channels, *Langmuir* 29 (2013) 9031–9040, <https://doi.org/10.1021/LA400716C>.
- [165] Y.C. Chou, P. Masih Das, D.S. Monos, D.S. Monos, M. Drndić, Lifetime and stability of silicon nitride nanopores and nanopore arrays for ionic measurements, *ACS Nano* 14 (2020) 6715–6728, <https://doi.org/10.1021/ACS.NANO.9B09964>.
- [166] N. Yang, X. Jiang, Nanocarbons for DNA sequencing: a review, *Carbon N Y* 115 (2017) 293–311, <https://doi.org/10.1016/J.CARBON.2017.01.012>.
- [167] H. Qiu, W. Zhou, W. Guo, Nanopores in graphene and other 2D materials: a decade's journey toward sequencing, *ACS Nano* 15 (2021) 18848–18864, <https://doi.org/10.1021/ACS.NANO.1C07960>.
- [168] J.D. Spitzberg, A. Zrehen, X.F. van Kooten, A. Meller, Plasmonic-nanopore biosensors for superior single-molecule detection, *Adv. Mater.* 31 (2019) 1900422, <https://doi.org/10.1002/ADMA.201900422>.
- [169] L. Wang, M.S.H. Boutilier, P.R. Kidambi, D. Jang, N.G. Hadjicostantinou, R. Karnik, Fundamental transport mechanisms, fabrication and potential applications of nanoporous atomically thin membranes, *Nat. Nanotechnol.* 12 (2017) 509–522, <https://doi.org/10.1038/nnano.2017.72>, 2017 12:6.
- [170] Z. Wang, T.Y. Lv, Z.B. Shi, S.S. Yang, Z.Y. Gu, Two-dimensional materials as solid-state nanopores for chemical sensing, *Dalton Trans.* 50 (2021) 13608–13619, <https://doi.org/10.1039/D1DT02206G>.
- [171] G. Danda, M. Drndić, Two-dimensional nanopores and nanoporous membranes for ion and molecule transport, *Curr. Opin. Biotechnol.* 55 (2019) 124–133, <https://doi.org/10.1016/J.COPBIO.2018.09.002>.
- [172] G.H. Ryu, A. France-Lanord, Y. Wen, S. Zhou, J.C. Grossman, J.H. Warner, Atomic structure and dynamics of self-limiting sub-nanometer pores in monolayer WS<sub>2</sub>, *ACS Nano* 12 (2018) 11638–11647, <https://doi.org/10.1021/ACS.NANO.8B07051>.
- [173] G. Danda, P. Masih Das, Y.C. Chou, J.T. Mlack, W.M. Parkin, C.H. Naylor, K. Fujisawa, T. Zhang, L.B. Fulton, M. Terrones, A.T.C. Johnson, M. Drndić, Monolayer WS<sub>2</sub> nanopores for DNA translocation with light-adjustable sizes, *ACS Nano* 11 (2017) 1937, <https://doi.org/10.1021/ACS.NANO.6B08028>. –1945.
- [174] W. Si, Y. Zhang, G. Wu, J. Sha, L. Liu, Y. Chen, DNA sequencing technology based on nanopore sensors by theoretical calculations and simulations, *Chin. Sci. Bull.* 59 (2014) 4929–4941, <https://doi.org/10.1007/S11434-014-0622-X>.
- [175] M. Kokkonen, M. Jestoi, A. Rizzo, Determination of selected mycotoxins in mould cheeses with liquid chromatography coupled tandem with mass spectrometry, *Food Addit. Contam.* 22 (2005) 449–456, <https://doi.org/10.1080/02652030500089861>.
- [176] F. Wu, P.A. Thomas, V.G. Kravets, H.O. Arola, M. Soikkeli, K. Iljin, G. Kim, M. Kim, H.S. Shin, D.v. Andreeva, C. Neumann, M. Küllmer, A. Turchanin, D. de Fazio, O. Balci, V. Babenko, B. Luo, I. Goykhman, S. Hofmann, A.C. Ferrari, K.S. Novoselov, A.N. Grigorenko, Layered material platform for surface plasmon resonance biosensing, *Sci. Rep.* 9 (2019) 1–9, <https://doi.org/10.1038/s41598-019-56105-7> (2019) 1–10.
- [177] F.H. Zhai, Q.Q. Zhan, K. Wang, S. Chen, R.H. He, A homogeneous DNA nanosphere for fluorescence detection of microRNAs with high-ordered aggregation enhanced emission and enzyme-free cascade amplification, *Sensor. Actuator. B Chem.* 320 (2020) 128394, <https://doi.org/10.1016/j.snb.2020.128394>.
- [178] H.J. Lim, T. Saha, B.T. Tey, W.S. Tan, C.W. Ooi, Quartz crystal microbalance-based biosensors as rapid diagnostic devices for infectious diseases, *Biosens. Bioelectron.* 168 (2020) 112513, <https://doi.org/10.1016/j.bios.2020.112513>.
- [179] Y. Huang, A. Hara, C. Terashima, A. Fujishima, M. Takai, Protein adsorption behavior on reduced graphene oxide and boron-doped diamond investigated by electrochemical impedance spectroscopy, *Carbon N Y* 152 (2019) 354–362, <https://doi.org/10.1016/j.carbon.2019.06.023>.
- [180] M. Bahri, A. Baraket, N. Zine, M. Ben Ali, J. Bausells, A. Errachid, Capacitance electrochemical biosensor based on silicon nitride transducer for TNF- $\alpha$  cytokine detection in artificial human saliva: aouit failure (HF), *Talanta* 209 (2019) 120501, <https://doi.org/10.1016/j.talanta.2019.120501>.
- [181] M. Bahri, M. Amin Elaguech, S. Nasraoui, K. Djebbi, O. Kanoun, P. Qin, C. Tlili, D. Wang, Laser-Induced graphene electrodes for highly sensitive detection of DNA hybridization via consecutive cytosines (polyC)-DNA-based electrochemical biosensors, *Microchem. J.* 185 (2023) 108208, <https://doi.org/10.1016/J.MICROC.2022.108208>.
- [182] J. Shan, J. Li, X. Chu, M. Xu, F. Jin, X. Wang, L. Ma, X. Fang, Z. Wei, X. Wang, High sensitivity glucose detection at extremely low concentrations using a MoS<sub>2</sub>-based field-effect transistor, *RSC Adv.* 8 (2018) 7942–7948, <https://doi.org/10.1039/C7RA13614E>.
- [183] X. Kong, M. Bahri, K. Djebbi, B. Shi, D. Zhou, C. Tlili, D. Wang, Graphene-based liquid gated field-effect transistor for label-free detection of DNA hybridization, in: 18th IEEE International Multi-Conference on Systems, Signals and Devices, SSD., 2021, pp. 387–391, <https://doi.org/10.1109/SSD52085.2021.9429414>.
- [184] F. Wang, Z. Wang, C. Jiang, L. Yin, R. Cheng, X. Zhan, K. Xu, F. Wang, Y. Zhang, J. He, Progress on electronic and optoelectronic devices of 2D layered semiconducting materials, *Small* 13 (2017) 1604298, <https://doi.org/10.1002/SMLL.201604298>.
- [185] M. Chhowalla, D. Jena, H. Zhang, Two-dimensional semiconductors for transistors, *Nat. Rev. Mater.* 1 (2016) 11, <https://doi.org/10.1038/natrevmats.2016.52>, 1 (2016) 1–15.
- [186] L. Liu, S.B. Kumar, Y. Ouyang, J. Guo, Performance limits of monolayer transition metal dichalcogenide transistors, *IEEE Trans. Electron. Dev.* 58 (2011) 3042–3047, <https://doi.org/10.1109/TED.2011.2159221>.
- [187] K.T. Chen, S.T. Chang, How high can the mobility of monolayer tungsten disulfide be? *Vacuum* 140 (2017) 172–175, <https://doi.org/10.1016/J.VACUUM.2016.11.006>.
- [188] X. Liu, J. Hu, C. Yue, N. della Fera, Y. Ling, Z. Mao, J. Wei, High performance field-effect transistor based on multilayer tungsten disulfide, *ACS Nano* 8 (2014) 10396–10402, <https://doi.org/10.1021/NN505253P>.
- [189] W. Sik Hwang, M. Remskar, R. Yan, V. Protasenko, K. Tahy, S. Doo Chae, P. Zhao, A. Konar, H. Xing, A. Seabaugh, D. Jena, Transistors with chemically synthesized layered semiconductor WS<sub>2</sub> exhibiting 105 room temperature modulation and ambipolar behavior, *Appl. Phys. Lett.* 101 (2012) 013107, <https://doi.org/10.1063/1.4732522>.
- [190] D. Braga, I. Gutiérrez Lezama, H. Berger, A.F. Morpurgo, Quantitative determination of the band gap of WS<sub>2</sub> with ambipolar ionic liquid-gated transistors, *Nano Lett.* 12 (2012) 5218–5223, <https://doi.org/10.1021/NL302389D>.
- [191] M. Remskar, M. Virsek, A. Jesih, WS<sub>2</sub> nanobands as a new hybrid nanomaterial, *Nano Lett.* 8 (2007) 76–80, <https://doi.org/10.1021/NL0719426>.
- [192] L. Wang, Y. Wang, J.I. Wong, T. Palacios, J. Kong, H.Y. Yang, Functionalized MoS<sub>2</sub> nanosheet-based field-effect biosensor for label-free sensitive detection of cancer marker proteins in solution, *Small* 10 (2014) 1101–1105, <https://doi.org/10.1002/SMLL.201302081>.
- [193] G. Zhou, J. Chang, H. Pu, K. Shi, S. Mao, X. Sui, R. Ren, S. Cui, J. Chen, Ultrasensitive mercury ion detection using DNA-functionalized molybdenum disulfide nanosheet/gold nanoparticle hybrid field-effect transistor device, *ACS Sens.* 1 (2016) 295–302, <https://doi.org/10.1021/ACSENSORS.5B00241>.
- [194] X. Chen, S. Hao, B. Zong, C. Liu, S. Mao, Ultrasensitive antibiotic sensing with complementary strand DNA assisted aptamer/MoS<sub>2</sub> field-effect transistors, *Biosens. Bioelectron.* 145 (2019) 111711, <https://doi.org/10.1016/j.bios.2019.111711>.
- [195] D.-W. Lee, J. Lee, I.Y. Sohn, B.-Y. Kim, Y.M. Son, H. Bark, J. Jung, M. Choi, T.H. Kim, C. Lee, N.-E. Lee, Field-effect transistor with a chemically synthesized MoS<sub>2</sub> sensing channel for label-free and highly sensitive electrical detection of DNA hybridization, *Nano Res.* 8 (2015) 2340–2350, <https://doi.org/10.1007/S12274-015-0744-8>, 2015 8:7.
- [196] S.M. Majid, A. Salimi, F. Ghasemi, An ultrasensitive detection of miRNA-155 in breast cancer via direct hybridization assay using two-dimensional molybdenum disulfide field-effect transistor biosensor, *Biosens. Bioelectron.* 105 (2018) 6–13, <https://doi.org/10.1016/J.BIOS.2018.01.009>.
- [197] T. J. rvinen, G.S. Lorite, J. Per nte, G. Toth, S. Saarakkala, V.K. Virtanen, K. Kordas, WS<sub>2</sub> and MoS<sub>2</sub> thin film gas sensors with high response to NH<sub>3</sub> in air at low temperature, *Nanotechnology* 30 (2019), <https://doi.org/10.1088/1361-6528/AB2D48>.

- [198] N. Huo, S. Yang, Z. Wei, S.S. Li, J.B. Xia, J. Li, Photoresponsive and gas sensing field-effect transistors based on multilayer WS<sub>2</sub> nanoflakes, *Sci. Rep.* 4 (2014), <https://doi.org/10.1038/SREP05209>.
- [199] X. Wei, C. Liu, H. Qin, Z. Ye, X. Liu, B. Zong, Z. Li, S. Mao, Fast, specific, and ultrasensitive antibiotic residue detection by monolayer WS<sub>2</sub>-based field-effect transistor sensor, *J. Hazard Mater.* 443 (2023) 130299, <https://doi.org/10.1016/J.JHAZMAT.2022.130299>.
- [200] Z. Huang, J. Liu, Length-dependent diblock DNA with poly-cytosine (poly-C) as high-affinity anchors on graphene oxide, *Langmuir* 34 (2017) 1171–1177, <https://doi.org/10.1021/ACS.LANGMUIR.7B02812>.
- [201] C. Lu, Z. Huang, B. Liu, Y. Liu, Y. Ying, J. Liu, Poly-cytosine DNA as a high-affinity ligand for inorganic nanomaterials, *Angew. Chem. Int. Ed.* 56 (2017) 6208–6212, <https://doi.org/10.1002/anie.201702998>.
- [202] L.A. Bawazer, A.M. Newman, Q. Gu, A. Ibish, M. Arcila, J.B. Cooper, F.C. Meldrum, D.E. Morse, Efficient selection of biomineralizing DNA aptamers using deep sequencing and population clustering, *ACS Nano* 8 (2013) 387–395, <https://doi.org/10.1021/NN4044488>.
- [203] J.M. George, A. Antony, B. Mathew, Metal oxide nanoparticles in electrochemical sensing and biosensing: a review, *Mikrochim. Acta* 185 (2018), <https://doi.org/10.1007/S00604-018-2894-3>.
- [204] J. Wang, X. Pang, X. Tan, Y. Song, L. Liu, Q. You, Q. Sun, F. Tan, N. Li, A triple-synergistic strategy for combinational photo/radiotherapy and multi-modality imaging based on hyaluronic acid-hybridized polyaniline-coated WS<sub>2</sub> nanodots, *Nanoscale* 9 (2017) 5551–5564, <https://doi.org/10.1039/C6NR09219E>.
- [205] S. Nandi, S.K. Bhunia, L. Zeiri, M. Pour, I. Nachman, D. Raichman, J.P.M. Lellouche, R. Jelinek, Bifunctional carbon-dot-WS<sub>2</sub> nanorods for photothermal therapy and cell imaging, *Chem. Eur J.* 23 (2017) 963–969, <https://doi.org/10.1002/CHEM.201604787>.
- [206] X. Song, W. Shang, L. Peng, H. Jiang, K. Wang, C. Fang, J. Tian, Novel GPC3-binding WS<sub>2</sub>-Ga<sup>3+</sup>-PEG-peptide nanosheets for in vivo bimodal imaging-guided photothermal therapy, *Nanomedicine (Lond)* 13 (2018) 1681–1693, <https://doi.org/10.2217/NNM-2017-0367>.
- [207] Y. Yong, X. Cheng, T. Bao, M. Zu, L. Yan, W. Yin, C. Ge, D. Wang, Z. Gu, Y. Zhao, Tungsten sulfide quantum dots as multifunctional nanotheranostics for in vivo dual-modal image-guided photothermal/radiotherapy synergistic therapy, *ACS Nano* 9 (2015) 12451–12463, <https://doi.org/10.1021/ACS.NANO.5B05825>.
- [208] G. Yang, R. Zhang, C. Liang, H. Zhao, X. Yi, S. Shen, K. Yang, L. Cheng, Z. Liu, Manganese dioxide coated WS<sub>2</sub>@Fe<sub>3</sub>O<sub>4</sub>/ssiO<sub>2</sub> nanocomposites for pH-responsive MR imaging and oxygen-elevated synergistic therapy, *Small* 14 (2018) 172664, <https://doi.org/10.1002/SMLL.201702664>.
- [209] Y. Wang, S. Song, T. Lu, Y. Cheng, Y. Song, S. Wang, F. Tan, J. Li, N. Li, Oxygen-supplementing mesoporous polydopamine nanospheres with WS<sub>2</sub> QDs-embedded for CT/MSOT/MR imaging and thermoradiotherapy of hypoxic cancer, *Biomaterials* 220 (2019) 119405, <https://doi.org/10.1016/J.BIOMATERIALS.2019.119405>.
- [210] Y. Chao, G. Wang, C. Liang, X. Yi, X. Zhong, J. Liu, M. Gao, K. Yang, L. Cheng, Z. Liu, Rhenium-188 labeled tungsten disulfide nanoflakes for self-sensitized, near-infrared enhanced radioisotope therapy, *Small* 12 (2016) 3967–3975, <https://doi.org/10.1002/SMLL.201601375>.
- [211] Y. Liu, X. Ji, J. Liu, W.W.L. Tong, D. Askhatova, J. Shi, Tantalum sulfide nanosheets as a theranostic nanopatform for computed tomography imaging-guided combinatorial chemo-photothermal therapy, *Adv. Funct. Mater.* 27 (2017) 1703261, <https://doi.org/10.1002/ADFM.201703261>.
- [212] N. Ma, M.K. Zhang, X.S. Wang, L. Zhang, J. Feng, X.Z. Zhang, NIR light-triggered degradable MoTe<sub>2</sub> nanosheets for combined photothermal and chemotherapy of cancer, *Adv. Funct. Mater.* 28 (2018) 1801139, <https://doi.org/10.1002/ADFM.201801139>.
- [213] X. Meng, Z. Liu, Y. Cao, W. Dai, K. Zhang, H. Dong, X. Feng, X. Zhang, Fabricating aptamer-conjugated PEGylated-MoS<sub>2</sub>/Cu<sub>1.8</sub>S theranostic nanopatform for multiplexed imaging diagnosis and chemo-photothermal therapy of cancer, *Adv. Funct. Mater.* 27 (2017) 1605592, <https://doi.org/10.1002/ADFM.201605592>.
- [214] R. Deng, H. Yi, F. Fan, L. Fu, Y. Zeng, Y. Wang, Y. Li, Y. Liu, S. Ji, Y. Su, Facile exfoliation of MoS<sub>2</sub> nanosheets by protein as a photothermal-triggered drug delivery system for synergistic tumor therapy, *RSC Adv.* 6 (2016) 77083–77092, <https://doi.org/10.1039/C6RA13993K>.
- [215] B. Geng, H. Qin, F. Zheng, W. Shen, P. Li, K. Wu, X. Wang, X. Li, D. Pan, L. Shen, Carbon dot-sensitized MoS<sub>2</sub> nanosheet heterojunctions as highly efficient NIR photothermal agents for complete tumor ablation at an ultralow laser exposure, *Nanoscale* 11 (2019) 7209–7220, <https://doi.org/10.1039/C8NR10445J>.
- [216] L. Chen, W. Feng, X. Zhou, K. Qiu, Y. Miao, Q. Zhang, M. Qin, L. Li, Y. Zhang, C. He, Facile synthesis of novel albumin-functionalized flower-like MoS<sub>2</sub> nanoparticles for in vitro chemo-photothermal synergistic therapy, *RSC Adv.* 6 (2016) 13040–13049, <https://doi.org/10.1039/C5RA27822H>.
- [217] J. Lee, H. Kim, M.J. Park, Long-life, high-rate lithium-organic batteries based on naphthoquinone derivatives, *Chem. Mater.* 28 (2016) 2408–2416, <https://doi.org/10.1021/ACS.CHEMMATER.6B00624>.
- [218] G. Yang, H. Gong, T. Liu, X. Sun, L. Cheng, Z. Liu, Two-dimensional magnetic WS<sub>2</sub>@Fe<sub>3</sub>O<sub>4</sub> nanocomposite with mesoporous silica coating for drug delivery and imaging-guided therapy of cancer, *Biomaterials* 60 (2015) 62–71, <https://doi.org/10.1016/J.BIOMATERIALS.2015.04.053>.
- [219] C. Zhang, Y. Yong, L. Song, X. Dong, X. Zhang, X. Liu, Z. Gu, Y. Zhao, Z. Hu, Photothermal therapy: multifunctional WS<sub>2</sub>@Polyetherimide nanopatforms for imaging guided gene-photothermal synergistic therapy of cancer (adv. Healthcare mater. 21/2016), *Adv. Healthcare Mater.* 5 (2016), <https://doi.org/10.1002/ADHM.201670116>, 2834–2834.
- [220] L. Cheng, C. Yuan, S. Shen, X. Yi, H. Gong, K. Yang, Z. Liu, Bottom-up synthesis of metal-ion-doped WS<sub>2</sub> nanoflakes for cancer theranostics, *ACS Nano* 9 (2015) 11090–11101, <https://doi.org/10.1021/ACS.NANO.5B04606>.
- [221] J. Li, X. Qi, P. Ye, M. Yang, M. Xie, Construction of WS<sub>2</sub>/Au-lipid drug delivery system for multiple combined therapy of tumor, *J. Drug Deliv. Sci. Technol.* 76 (2022), <https://doi.org/10.1016/j.jddst.2022.103747>.
- [222] M. Sobhani, A. Ziegler, E. Moniri, H. Ahmad Panahi, M. Daghighi Asli, Graft hyper-branched dendrimer onto WS<sub>2</sub> nanosheets modified Poly (N-Vinylcaprolactam) as a thermosensitive nanocarrier for Pioglitazone delivery using near-infrared radiation, *Int. J. Pharm.* 607 (2021) 120985, <https://doi.org/10.1016/J.IJPHARM.2021.120985>.
- [223] P.F. Hsiao, R. Anbazhagan, H.C. Tsai, Rajakumari krishnamoorthi, S.J. Lin, S.Y. Lin, K.Y. Lee, C.Y. Kao, R.S. Chen, J.Y. Lai, Fabrication of electroactive polypyrrole-tungsten disulfide nanocomposite for enhanced in vivo drug release in mice skin, *Mater. Sci. Eng. C* 107 (2020) 110330, <https://doi.org/10.1016/J.MSEC.2019.110330>.
- [224] C. Wu, S. Wang, J. Zhao, Y. Liu, Y. Zheng, Y. Luo, C. Ye, M. Huang, H. Chen, Biodegradable Fe(III)@WS<sub>2</sub>-PVP nanocapsules for redox reaction and TME-enhanced nanocatalytic, photothermal, and chemotherapy, *Adv. Funct. Mater.* 29 (2019) 1901722, <https://doi.org/10.1002/ADFM.201901722>.
- [225] G.R. Navale, C.S. Rout, K.N. Gohil, M.S. Dharne, D.J. Late, S.S. Shinde, Oxidative and membrane stress-mediated antibacterial activity of WS<sub>2</sub> and rGO-WS<sub>2</sub> nanosheets, *RSC Adv.* 5 (2015) 74726–74733, <https://doi.org/10.1039/C5RA15652A>.
- [226] R. Venkatasubramanian, R.S. Srivastava, R.D.K. Misra, Comparative study of antimicrobial and photocatalytic activity in titania encapsulated composite nanoparticles with different dopants, *Mater. Sci. Technol.* 24 (2013) 589–595, <https://doi.org/10.1179/174328408X282065>.
- [227] C. Bankier, R.K. Matharu, Y.K. Cheong, G.G. Ren, E. Cloutman-Green, L. Ciric, Synergistic antibacterial effects of metallic nanoparticle combinations, *Sci. Rep.* 9 (2019) 1–9, <https://doi.org/10.1038/s41598-019-52473-2>, 2019) 1–8.
- [228] H. Han, J. Yang, X. Li, Y. Qi, Z. Yang, Z. Han, Y. Jiang, M. Stenzel, H. Li, Y. Yin, Y. Du, J. Liu, F. Wang, Shining light on transition metal sulfides: new choices as highly efficient antibacterial agents, *Nano Res.* (2021) 2512–2534, <https://doi.org/10.1007/S12274-021-3293-3>, 2021) 14:8. 14.
- [229] Y. Deng, Z. Li, R. Tang, K. Ouyang, C. Liao, Y. Fang, C. Ding, L. Yang, L. Su, D. Gong, What will happen when microorganisms “meet” photocatalysts and photocatalysis? *Environ. Sci.: Nano* 7 (2020) <https://doi.org/10.1039/c9en01318k>.
- [230] X. Liu, G. Duan, W. Li, Z. Zhou, R. Zhou, Membrane destruction-mediated antibacterial activity of tungsten disulfide (WS<sub>2</sub>), *RSC Adv.* 7 (2017) 37873–37880, <https://doi.org/10.1039/C7RA06442J>.
- [231] T. Wang, X. Zhang, L. Mei, D. Ma, Y. Liao, Y. Zu, P. Xu, W. Yin, Z. Gu, A two-step gas/liquid strategy for the production of N-doped defect-rich transition metal dichalcogenide nanosheets and their antibacterial applications, *Nanoscale* 12 (2020) 8415–8424, <https://doi.org/10.1039/D0NR00192A>.
- [232] G. Gao, L. Wang, P. Yang, L. Huang, X. Xie, J. Wu, C. Qiu, L. Cai, Bio-Inspired growth of silver nanoparticles on 2D material’s scaffolds as heterostructures with their enhanced antibacterial property, *J. Nanosci. Nanotechnol.* 18 (2018) 3893–3900, <https://doi.org/10.1166/JNN.2018.15027>.
- [233] T.I. Kim, J. Kim, I.J. Park, K.O. Cho, S.Y. Choi, Chemically exfoliated 1T-phase transition metal dichalcogenide nanosheets for transparent antibacterial applications, *2d Mater.* 2019 025025, <https://doi.org/10.1088/2053-1583/AB070E>, 6.
- [234] I. Kaplan-Ashiri, S.R. Cohen, K. Gartsman, V. Ivanovskaya, T. Heine, G. Seifert, I. Wiesel, H.D. Wagner, R. Tenne, On the mechanical behavior of WS<sub>2</sub> nanotubes under axial tension and compression, *Proc. Natl. Acad. Sci. U.S.A.* 103 (2006) 523–528, <https://doi.org/10.1073/PNAS.0505640103>.

- [235] M.S. Wang, I. Kaplan-Ashiri, X.L. Wei, R. Rosentsveig, H.D. Wagner, R. Tenne, L.M. Peng, In situ TEM measurements of the mechanical properties and behavior of WS<sub>2</sub> nanotubes, *Nano Res.* 1 (2008) 22–31, <https://doi.org/10.1007/S12274-008-8008-5>, 2008 1:1.
- [236] E. Zohar, S. Baruch, M. Shneider, H. Dodiuk, S. Kenig, R. Tenne, H.D. Wagner, The effect of WS<sub>2</sub> nanotubes on the properties of epoxy-based nanocomposites, *J. Adhes. Sci. Technol.* 25 (2012) 1603–1617, <https://doi.org/10.1163/016942410X524138>.
- [237] C. Wen, J. Qian, L. Xiao, L. Luo, J. Zheng, M. Xie, J. Tao, X. Wu, B. Sa, K. Luo, Enhanced biological behavior and antibacterial property of WS<sub>2</sub> nanosheets modified mesoporous bioactive glass nanospheres for bone tissue engineering, *Ceram. Int.* 48 (2022) 33781–33793, <https://doi.org/10.1016/J.CERAMINT.2022.07.324>.
- [238] G. Lalwani, A.M. Henslee, B. Farshid, P. Parmar, L. Lin, Y.X. Qin, F.K. Kasper, A.G. Mikos, B. Sitharaman, Tungsten disulfide nanotubes reinforced biodegradable polymers for bone tissue engineering, *Acta Biomater.* 9 (2013) 8365–8373, <https://doi.org/10.1016/J.ACTBIO.2013.05.018>.
- [239] S.Y. Chen, C. Zheng, M.S. Fuhrer, J. Yan, Helicity-Resolved Raman Scattering of MoS<sub>2</sub>, MoSe<sub>2</sub>, WS<sub>2</sub>, and WSe<sub>2</sub> Atomic Layers, *Nano Lett.* 15 (2015) 2526–2532, <https://doi.org/10.1021/ACS.NANOLETT.5B00092>.
- [240] A. Gracco, M. Dandrea, F. Deflorian, C. Zanella, A. de Stefani, G. Bruno, E. Stellini, Application of a molybdenum and tungsten disulfide coating to improve tribological properties of orthodontic archwires, *Nanomaterials* 9 (2019), <https://doi.org/10.3390/NANO9050753>.
- [241] M. Redlich, A. Katz, L. Rapoport, H.D. Wagner, Y. Feldman, R. Tenne, Improved orthodontic stainless steel wires coated with inorganic fullerene-like nanoparticles of WS<sub>2</sub> impregnated in electroless nickel-phosphorous film, *Dent. Mater.* 24 (2008) 1640–1646, <https://doi.org/10.1016/J.DENTAL.2008.03.030>.
- [242] L. Tammaro, T. di Luccio, C. Borriello, F. Loffredo, K. Ramachandran, F. Villani, F. di Benedetto, T. Schiller, C. Minarini, J.A. Kornfield, Effect of tungsten disulfide (WS<sub>2</sub>) nanotubes on structural, morphological and mechanical properties of poly(L-lactide) (PLLA) films, *AIP Conf. Proc.* (2018) 020073, <https://doi.org/10.1063/1.5045935>, 1981.
- [243] Y.W. Chen, M.Y. Shie, C.H. Hsiao, Y.C. Liang, B. Wang, I.W.P. Chen, Synthesis of high-quality monolayer tungsten disulfide with chlorophylls and its application for enhancing bone regeneration, *Npj 2D Materials and Applications* 4 (2020) 1–9, <https://doi.org/10.1038/s41699-020-00168-y>, 2020 4:1.